Development of Hybrid Electrolytes for Solid-State Batteries

By

Vazrik Keshishian

A dissertation submitted in partial fulfillment
of the requirements for the degree of
Doctor of Philosophy
(Materials Science and Engineering)
in the University of Michigan
2022

Doctoral Committee:

Professor John Kieffer, Chair
Professor Richard M. Laine
Professor Pierre Ferdinand P. Poudeu
Assistant Professor Nirala Singh

Vazrik Keshishian

kvazrik@umich.edu

ORCID iD: 0000-0002-1313-4214

TABLE OF CONTENTS

LIST OF FIGURES

vi

LIST OF TABLES

ABSTRACT

Lithium-ion batteries that use solid-state electrolytes are crucial energy storage devices with widespread applications in small and large electronics, electric vehicles, electric aircrafts and grid-level energy storage. Conventional lithium-ion batteries based on liquid electrolytes lack chemical stability, have inherent safety issues, and incur a high production cost. Solid state electrolytes (SSEs) not only have the potential to correct these drawbacks but exhibit improved mechanical properties, which allows one to reduce the battery size, suppress dendrite growth, opening the possibility for metal anodes, and thus increase its energy density. However, power density requires good charge carrier mobility, which varies conversely with the factors that control mechanical properties. Thus, to simultaneously achieve high ionic conductivity and elastic moduli, we pursue a hybrid organic-inorganic composite materials design approach for creating the required SSEs.

Our hybrid electrolytes consist of a nano-porous silica backbone obtained through sol-gel synthesis that provides a three-dimensional percolating mechanically rigid scaffold. Polymer is subsequently deposited in the pores of this network via solution exchange, where it establishes the conducting phase. This unique approach allows us to decouple mechanical from cation transport properties of the material and achieve both high elastic stiffness and ionic conductivity. To increase the cation transference number, and thereby the Coulomb efficiency of the devices, we tether the cation donor to the silica scaffold. Initially, we aimed to do this with polymer chains as the intermediary. While this approach did not yield the desired outcome, we discovered that the properties of the gel-cast material are strongly influenced by unexpected structural evolution during drying, to the effect that ionic conductivities can vary by up to three orders of magnitude in these hybrids, without modifying their chemical makeup. Depending on the sample shape and aspect ratio, the drying process occurs inhomogeneously, imparting various degrees of anisotropy and spatial gradients that can be affect the development of the network topology. Cylindrical disk-shaped samples dry and rigidify

first on their periphery, causing tensile stresses to build towards the center as the drying front progresses inward. This causes reconditioning of the network structure at the core of the disk, resulting in a markedly higher conductivity with minimal reduction of mechanical stiffness.

We successfully developed an alternative approach for immobilizing cation donors and increasing the transference number of Li^+ to greater than 0.9. To this end we modified sulfonyl (trifluoromethylsulfonyl) imide (STFSI) chemistry by functionalizing the side chain of tetraethyl orthosilicate to incorporate the STFSI cation donor directly into the silica backbone. This approach significantly enhances the ionic mobility without negatively impacting the chemical or physical stability of the material. Moreover, we show that of anchoring oligo-PEO to the silica backbone, entangles with additional non-bonded short-chain PEO further enhances ionic conductivity in the solid electrolyte. To boost the ionic conductivity even more, a mixture of propylene carbonate (PC) and ethylene carbonate (EC) with various weight fractions was introduced in the silica backbone. This configuration yields the highest conductivity for the composite system, while the nano-confinement enhances the physical stability of EC and PC.

CHAPTER 1   Introduction

1–1   Background and Motivation

Overconsumption of non-renewable energy resources has causes serious environmental damage. To mitigate the negative impact of emissions from burning fossil fuels, renewable energy resources such as wind and solar power are considered as a viable alternative. However, these renewable forms of energy are available inconsistently, which requires attention to be focused on improving the technologies associated with energy storage. Improving lithium-ion battery technology is a promising approach to alleviate energy storage limitations since the use of such battery devices is ubiquitous.[1–3]

Lithium-ion batteries consist of an anode, a cathode and an electrolyte. The anode and cathode are the two terminals of the battery, which are separated by an electrolyte. Electrolytes are designed to separate the electrochemical reactions occurring in the anode and the cathode while allowing only the transport of the conducting species, lithium ions, and at the same time directing the movement of electrons only to the external circuit. Solid electrolytes are also required to have high elastic moduli to not only suppress dendrite growth but also to provide load bearing functionality. Additionally, solid electrolytes with high ionic mobility are essential in order to achieve high power density lithium-ion battery devices.[4, 5]

Conventional lithium-ion batteries use liquid electrolytes, which consist of organic solvents. Liquid electrolytes are flammable thus resulting in safety issues. This class of electrolytes cause limitations in the design of battery packs since liquids cannot withstand shear forces. Manufacturing battery packs using solid electrolytes is cost effective since the design is simple and fewer parts are involved to create proper sealing. While liquid electrolytes require a battery housing or an inert porous scaffold to impart the necessary structural support in the device, solid electrolytes inherently establish such mechanical stability, thus reducing the battery's structural complexity and size. The use of solid-state electrolytes can further increase the power

density of battery devices since lithium metal can be used as the anode. Lithium metal increases the overall cell voltage, has a very low density (0.59 g.cm^{-3}), high theoretical specific capacity (3860 mA h g^{-1}), and a low electrochemical potential (-3.040 V).[6] However, the use of a lithium metal anode is still limited due to Li filament growth and interfacial reaction/delamination during electrochemical cycling.[7] The practical use of lithium metal is only possible by developing a solid electrolyte that is chemically and physically compatible with both electrodes and possesses a high shear modulus (> 7 GPa) to suppress dendrite growth.[8, 9]

A core challenge associated with developing solid-state-electrolytes is achieving high ionic conductivity rates. Ionic conductivity values greater than 10^{-4} S.cm^{-1} are essential for solid electrolytes in order to compete with the transport properties of liquid electrolytes. Generally, the structural characteristics of solid materials are inherently unsuitable for the rapid transport of lithium ions. Therefore, various attempts have been made to increase the lithium ion transport rates. Two main groups of materials that have been thoroughly investigated for the development of highly conductive solid electrolytes are inorganic ceramic electrolytes and organic polymer electrolytes. Most inorganic electrolytes are made of either sulfides or oxides. Most of the sulfide-based electrolytes show high ionic conductivity rates and are mechanically flexible.[10–12] However, these inorganic electrolytes are not very compatible with cathode material and react with water and oxygen.[13, 14] Sodium super ionic conductor (NASICON) ($Na_{1+x}Zr_2Si_xP_{3-x}O_{12}$, 0 < x < 3), garnet $Li_7La_3Zr_2O_{12}$ (LLZO), and perovskite $Li_{3.3}La_{0.56}TiO_3$ (LLTO) are examples of oxide-based solid electrolytes.[15] Oxide-based electrolytes have conductivity values around 10^3-10^5 S·cm^1 and are chemically quite stable. However, this group of materials has high interfacial resistances (> 10^3 Ω.cm^2) with electrodes and poor mechanical properties. It is very challenging to mass produce battery devices made of oxide solid electrolytes due to the rigidity and brittleness these materials, which brings obstacles to the assembly of battery componenets.[16–19]

Another subclass of SSEs are those in which a lithium salt, such as $LiClO_4$, $LiPF_6$, or $LiAsF_6$, is incorporated into a polymer matrix. Poly(methyl methacrylate) (PMMA), polyacrylonitrile (PAN), poly(vinylidene fluoride) (PVDF), poly(ethylene oxide) (PEO), and the derivatives of these polymers are commonly used as the matrix in these SSEs.

Composite		Ionic conductivity (S.cm^{-1})	Transference number	Electrochemical stability Vs. Li$^+$/Li	References
Polymer	Filler				
PEO	Li$_{1.5}$Al$_{0.5}$Ge$_{1.5}$(PO$_4$)$_3$	1×10^{-5} (R.T.)		Up to 4.75 V	[20]
	vertically aligned Li$_{1.5}$Al$_{0.5}$Ge$_{1.5}$(PO$_4$)$_3$	1.67×10^{-4} (R.T.); 1.11×10^{-3} (60°C)	0.56	1–4.5 V	[21]
	Li$_{1.3}$Al$_{0.3}$Ti$_{1.7}$(PO$_4$)$_3$	1.9×10^{-4} (40°C)			[22]
	vertically aligned Li$_{1.3}$Al$_{0.3}$Ti$_{1.7}$(PO$_4$)$_3$	5.2×10^{-5} (R.T.)		−0.5 to 5V	[23]
	Li$_{10}$GeP$_2$S$_{12}$	2.2×10^{-4} (R.T.) (70%	0.91 (90%)		[24]
	Li$_{10}$GeP$_2$S$_{12}$	2.2×10^{-4} (R.T.) (1% Li$_{10}$GeP$_2$S$_{12}$)		0–5.7 V (1% Li$_{10}$GeP$_2$S$_{12}$)	[25]
	Li$_6$PS$_5$Cl	10^{-3} (R.T.)			[26]
	nanofiber Li$_{0.33}$La$_{0.557}$TiO$_3$	2.4×10^{-4} (R.T.)		Up to 5.0 V	[27]
	3D Li$_{0.33}$La$_{0.557}$TiO$_3$ network	1.8×10^{-4} (R.T.)	0.33	Up to 4.5 V	[28]
	Li$_7$La$_3$Zr$_2$O$_{12}$ nanowires	2.4×10^{-4} (R.T.)		Up to 5.5 V	[27]
	tetragonal Li$_7$La$_3$Zr$_2$O$_{12}$	4.45×10^{-4} (55°C)		0–5 V	[29]
	Li$_{6.4}$La$_3$Zr$_{1.4}$Ta$_{0.6}$O$_{12}$ with solid plasticizer succinonitrile	1.22×10^{-4} (30°C)	0.41	Up to 5.5 V	[29]
	3D network of Li$_{1.4}$Al$_{0.4}$Ti$_{1.6}$(PO$_4$)$_3$/PAN enhanced PEO	6.5×10^{-4} (60°C)	0.32	0.5–5 V	[30]
PAN	Li$_{0.33}$La$_{0.557}$TiO$_3$	2.4×10^{-4} (R.T.)		Up to 4.7 V	[31]
PVDF-HPF	Li$_7$La$_3$Zr$_2$O$_{12}$	7.63×10^{-4} (30°C)	0.61	Up to 5.3 V	[26]
Poly(vinyl carbonate)	Li$_{10}$SnP$_2$S$_{12}$	2.0×10^{-4} (R.T.)	0.6	Up to 4.5 V	[32]

Table 1.1   Summary of various Polymer based electrolytes with transference number and conductivity

These polymers are easily conformable, which allows for successful manufacturing in geometries not accessible with ceramic materials.[33, 34] Polymer based electrolytes are light weight, very flexible, and make good contact with electrodes.[35] The segmental motion of the chains is the main mechanism that enables lithium ion transport in polymeric electrolytes. Their major drawback is poor mechanical strength. The Young's modulus for most polymer electrolytes is in the range of tens to hundreds of MPa. This class of electrolytes are also susceptible to dendrite growth and possess ionic conductivity values less than 10^{-5} S.cm^{-1}. Various strategies have been utilized to improve the ionic conductivity by addition of plasticizers and active or passive fillers. These approaches result in higher ionic conductivity rates; however, they negatively impact the mechanical properties of the polymer SSEs.[36–39]

To improve the drawbacks associated with single-phase electrolytes, a composite materials design approach is preferred since this approach makes use of the advantages of the individual constituents of the composite.

1–2　Literature Review

1–2.1　Solid Battery Electrolytes

To better comprehend this topic, the initial research starting from early ionic conductors to present solid state electrolytes is discussed. The attempts to develop solid electrolytes dates to 19th century. In early 1830s, Faraday demonstrated the ionic properties of Ag_2S and PbF_2.[40] These solid compounds showed ionic properties at 177 ºC and 500 ºC, respectively. More solid ionic conductors were discovered after 1851 when J. Hittorf investigated Ag_2S and showed this compound is decomposable. The term solid electrolyte was used for the first time at the end of 19th century. Through a series of books called "The Science of Electricity" published by G. Wiedemann, the behavior of solid electrolytes was discussed intensively. By 1899, the efforts of W. Nernst resulted in development of an ionic conductor made of 85% ZrO_2 and 15% Y_2O, which became a famous composition and later on developed commercially. Prior to 1960, very few solid state electrolytes were developed with high ionic mobility specially at room temperature. It wasn't until 1960's that the term solid-state ionics was used. T.Takahashi and O. Yamamato developed Ag_3SI, which was highly conductive, 1×10^{-2} S.cm^{-1} at 20 ºC. Later on, J. Krummer and Y. Weber introduced β-Alumina, $Na_2O.11Al_2O_3$, which showed very high sodium ion conductivity. One other highly conductive solid electrolytes is Ag_4MI_5 (M= RB, K or NH_4), which was discovered by J. Bradley and P. Greene. [41, 42]

The introduction of organic solid electrolytes started in 1973 with the synthesis of a crystalline complex of sodium and potassium in PEO matrix. J.Coetzer et al., developed a high density battery, which consisted of liquid sodium anode, β-alumina as electrolytes and a solid-state cathode. [43] In addition to ionic solid electrolytes, which consist of ions such as Ag^{2+}, Na^+, O^{2-}, solid polymeric electrolytes that consisted of a polymer and lithium salt was developed for the first time in 1979 by Armand and co-workers. [44] After that, different polymers such as PVDF, PMMA, PAN etc. have been incorporated in lithium batteries.[45] The introduction of inorganic SSEs occurred in Oak Ridge National Laboratory in 1992. This led to development

of various inorganic lithium based conductive materials. Inorganic oxides, sulfides and halides are the

majority inorganic SSEs that have been developed and investigated thoroughly.[46]

1–2.2   Mechanism of Li ion transport in solid electrolytes

In crystalline inorganic material, the mechanism of ionic transport is based on the defects present in the

structure of these materials (see Fig. 1.1). The concentration and the distribution of these defects play an

important role in lithium ion transport. There are various types of defects such as point defects, line defect,

volume defect etc. Point defects can have simple or complicated diffusion mechanisms.
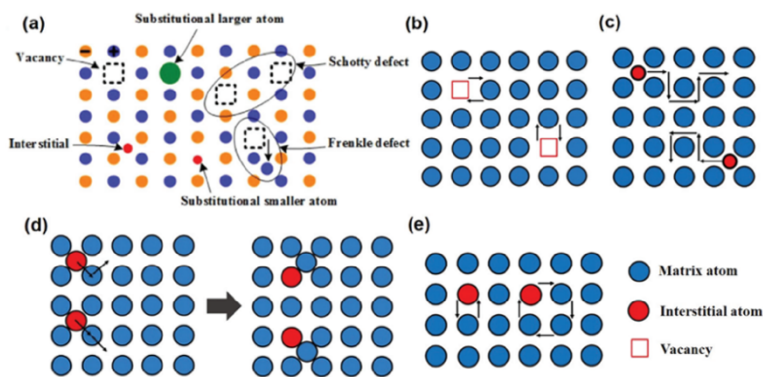
Figure 1.1   Schematic diagram for mechanisms of Li ionic transport in active inorganic region. (a) Some typical point defects in the inorganic part of CSSEs, reprinted with permission from ref.[47] Copyright 2018, Elsevier Ltd. (b) Vacancy diffusion mechanism, (c) direct interstitial mechanism, (d) interstitial knock-off mechanism, and (e) direct exchange and ring mechanism.[47] Reprinted with permission from ref. 47. Chinese Physical Society and IOP Publishing Ltd.

For Schottky and Frenkel point defects the mechanism of lithium ion transport is based on moving from the

previous equilibrium position to the adjacent vacancy. The activation energy is much lower during the ion

hoping due to much smaller lattice strain. As mentioned earlier, the vacancy concentration directly affects the

transport kinetics of lithium ions. Moreover, the category of ion adjacent to the diffusion pathway and the

configuration of the vacancy nearby can potentially influence the energy barrier for lithium ion transport.

The main representative of non-vacancy mechanism is the interstitial mechanism, which includes direct interstitial diffusion and the knock-off diffusion shown in the figure above. When the ion directly moves to the interstitial site, this type of diffusion is direct. In the indirect form, the interstitial atom first collides with the atom in the matrix resulting in the migration of matrix atom to the interstitial site. In this scenario, the size of the interstitial atom can be smaller or the size of matrix atom. We can also have the interstitial substitutional exchange mechanism, which consists of two different categories: direct exchange and ring diffusion. In direct exchange, two atoms are interacting simultaneously and exchange the lattice site with each other. In the ring diffusion process, a group of atoms are moving a distance equivalent to one atom to occupy new positions. The overall energy barrier for the non-defect diffusion processes is much higher compared to the defect based ionic transport.[48–51]

In some mixed-network former glasses such as sodium borosilicate and sodium borogermanate, the network structure changes while the network modifier mole fraction is kept constant. This allows us to understand how network structure can affect ionic conductivity and mechanical properties. These systems have two competing structural factors due to presence of a maxima in the longitudinal, shear and Young's moduli as a function of composition. For both systems, the bulk modulus shows a strong correlation with the negative logarithm of the ionic conductivity, as well as the activation energy for ionic conduction, at all compositions. An extension of the Anderson–Stuart model is used to describe the cation migration mechanisms in these structures, simultaneously accounting for the observed behaviors in ionic mobility and structural rigidity.[52]

1–2.2.1   Mechanisms of Li ion transport in polymers

Organic polymers have been mostly used as the matrix in composite electrolytes due to the flexibility and versatility polymer chains. The focus of discussion here is on the use of dry polymers. These systems are generally developed by dissolving lithium salts in solid polymers, which have polar groups present in the polymer chain. As mentioned before, lithium ion conduction mostly occurs in the amorphous region above the T_g. Based on the free-volume model, lithium ions are located at ideal coordination sites of the segmental chain of the polymer. A free volume is created around the segmental chain of the polymer as the systems

undergoes segmental motion in a seemingly liquid behavior. This allows the lithium ion to hop from one site to another as the free volume is created around one chain or between the chains.

The crystalline region of solid polymer electrolytes can also accommodate ion transport. Z. Gadjourova *et al.* showed that the ionic conductivity in the ordered crystalline phase of $PEO_6 : LiXF_6$ (X=P, As and Sb) can be higher than that of the amorphous region above T_g.
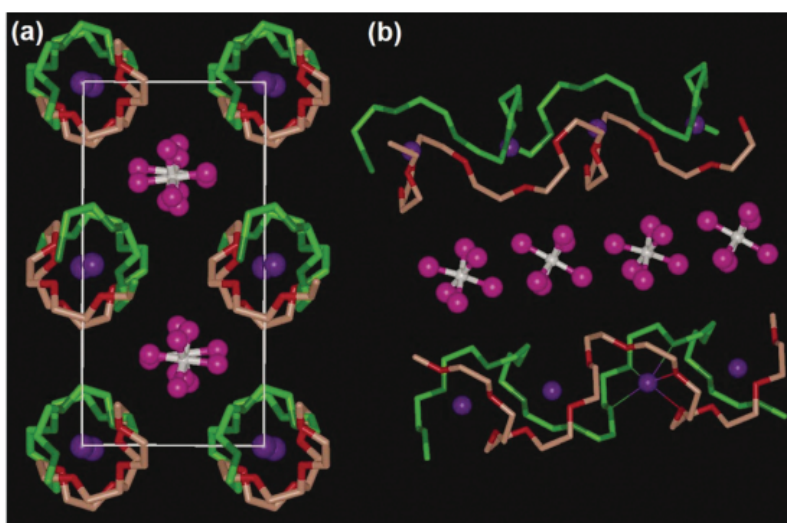
Figure 1.2   Structure of a typical solid polymer electrolyte material (poly(ethylene oxide)6:LiAsF6). (a) View along the chain axis for the Li+ transport pathway and (b) view of the relative position of the chains and their conformation. (Blue, Li; white, As; pink, F; light and dark green are for C and O in chain 1; and light and dark red are for C and O in chain 2, respectively).[100,108] Reprinted with permission from ref. [53] Copyright 2001 and 1999 Nature Publishing Group, respectively.

As it has been shown in Fig 1.2, the PEO polymer chains fold to form a cylindrical shape tunnel in which lithium ions are positioned in the coordination sites and the $(XF_6)^{-1}$ anions are uncoordinated. The lithium ions move along these tunnels without the need of segmental motion. The ion conductivity of these crystalline complexes can be further increased by the $(XF_6)^{-1}$ anions.

Various factors influence the ionic transport of polymer electrolytes. The dependence of ionic transport on temperature, polymer structure, molecular weight, dissociation of lithium salt provide complexity to these systems.

1–2.2.2   Mechanisms of Li ion transport at the interfacial region

Composite solid electrolytes (CSS) usually consist of three components that can potentially contribute to the ionic conductivity of the material. The bulk of organic or inorganic phases and the interfacial regions form these three components. The main components can be either active or passive. For instance, in an inorganic/organic composite electrolyte we can have SiO_2, Al_2O_3 and ZrO_2 as the passive fillers of the organic matrix. Active inorganic fillers such as LLZO, LATP, LLTO etc. can be used as the components to fill the organic framework. It is also possible to have composite solid electrolytes with passive and active fillers as the main components of the electrolyte.

The mechanism of ionic mobility in the interfacial region is difficult to investigate and depends largely on the constituents of the material. Generally, the addition of inorganic fillers to the polymer matrix can lower the glass transition temperature and decrease the degree of crystallinity.[54] The dispersion of particles in the matrix of the composite electrolyte is key to achieving a large interphase volume fraction and high ionic conductivity. Various factors that influence the dispersion are the surface chemistry of the particle, the interaction of the particles with the polymer matrix environment and the methods used to disperse the particles. If particle interactions are favored over the interaction of the particles with the matrix, this results in agglomeration of particles, which results in smaller interfacial area.[55–57]

1–2.3   Materials Synthesis

1–2.3.1   Sol-gel Chemical Synthesis

The solution-gelation (sol-gel) processing approach has been widely implemented in various engineering and scientific projects due to the diverse applications of the resulting products. This solution chemistry approach can offer a variety of functionalized materials such as inorganic glasses, ceramics and hybrids of organic/inorganic.

Understanding hydrolysis and condensation reactions are essential to mastering of sol-gel chemistry. The hydrolysis and condensation reactions are influenced by the presence and concentration of catalysts

(acid/base), the ratio of water to the precursor and the nature of the functionalized groups. The structure of the final gel is significantly different depending on the type of catalyst used due to the relative rates of hydrolysis and condensation reactions. The hydrolysis reaction results in replacing an alkoxy group with a hydroxy group independent of the nature of the catalyst group. Based on the ratio of silicon to water, it is possible to hydrolyze more than one alkoxy group.[58] The stability of the transition state for each hydrolysis step dictates the rate of the reaction. The successive hydrolysis reactions get progressively slower when the reaction is acid catalyzed and faster under basic conditions.[59]

$$Si(OR)_4 + nH_2O \rightarrow Si(OR)_{4-n}(OH)_n + nROH$$
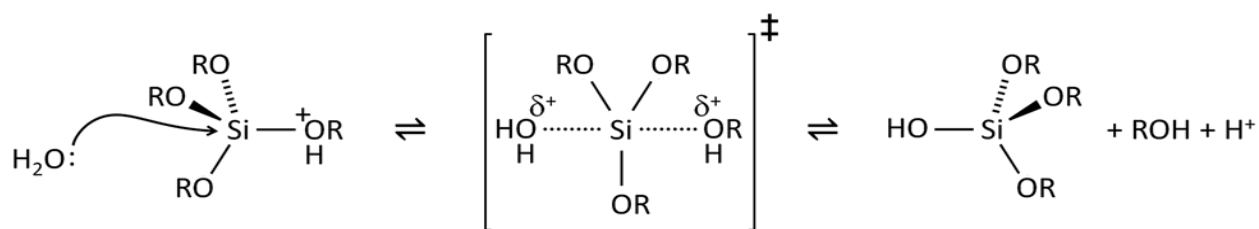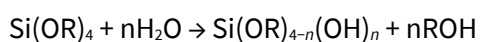
Scheme 1.1   Acid catalyzed hydrolysis of silicon alkoxides.
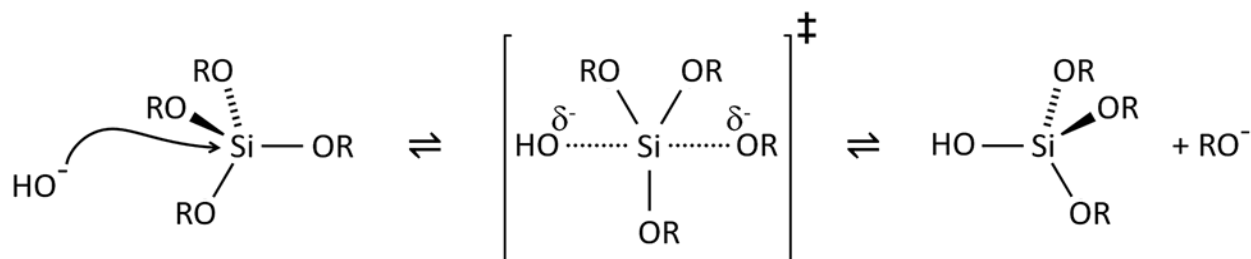
Scheme 1.2   Base catalyzed hydrolysis of silicon alkoxides

The condensation reactions are catalyzed under acidic or basic conditions similar to hydrolysis reactions. This result of the condensation reaction is the formation of siloxane bonds. The degree of hydrolysis determines the progression of the condensation reaction since one silanol group is needed on at least one silicon center. Under basic conditions, the hydrolysis step progresses faster and if the hydrolysis is completed before the

initiation of the condensation reaction, the product will look like as the following: $(OH)_3Si–O–Si(OH)_3$. This molecule has 6 available sites for further condensation.
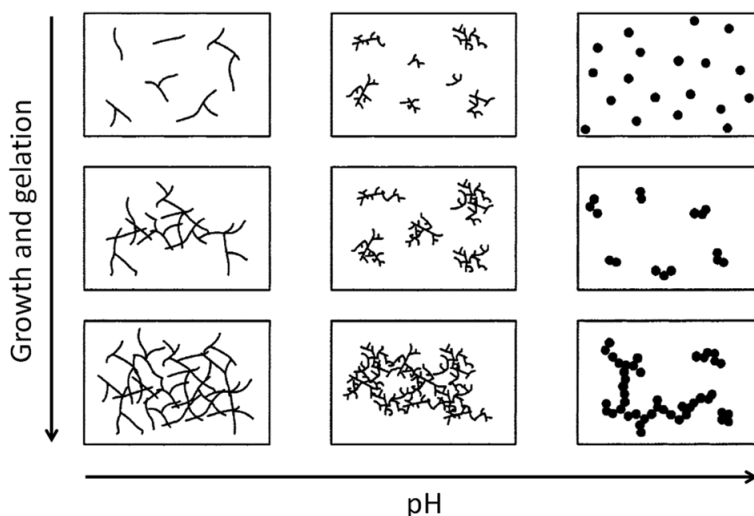
Figure 1.3   Diagram showing how pH affects the growth and structure of a gel; adapted with permission from ref. [60] Copyright (2004) American Chemical Society.

The result of multiple condensation reaction is a small and highly branched agglomerates in the solution that form a colloidal gel as the agglomerates crosslink. Under acidic conditions, since the first hydrolysis step is the fastest, condensation is initiated before the termination of the hydrolysis reaction. The condensation reaction usually happens on terminal silanols, which results in the formation of a network like structure.

There are other factors that influence the rate of hydrolysis and condensation, which are pH independent. One important factor is the presence of solvents. The solvent molecules can directly interact with the silicon atoms or enhance mixing since most silicon alkoxides are immiscible with water. The ratio of alkoxide to water is an important parameter to be used to limit hydrolysis. There are various derivatives of silicon alkoxides and the inductive and steric effects of the *R* group can influence the hydrolysis rates. Molecular silicon chemistry is very versatile and much more diverse than the simple tetra-alkoxides. Lastly, chelating agents such as acetylacetone can be incorporated to change hydrolysis and condensation rates. This approach is less common with the sol-gel chemistry of silicon derivatives.

Titanium and zirconium are other early transition metals that can be used to for sol-gel chemistry. These transition metals have lower electronegativity than silicon. The partial charge model can be applied to predict the stability and reactivity of alkoxides. The partial charges for silicon, titanium and zirconium in a four coordinate tetraethoxy complex are +0.32, +0.63 and +0.74 respectively. Hydrolysis proceeds via nucleophilic attack by water molecule to the central atom. The higher partial positive charge of titanium and zirconium explain the reason for higher hydrolysis rates of these metals. The higher rate of hydrolysis can be problematic during the synthesis of tertiary and quaternary complexes due to vigorous reaction with water. While catalysts are used to speed up the hydrolysis and condensation, additives are used for titanium alkoxides to slow down the reaction rates. To substitute the ethoxy or methoxy groups in the complexes, one uses bidentate and multidentate ligands such as acetylacetone.[61] The reactivity of titanium precursor is dependent on the alkoxide to ligand ratio and the strength of the bonds formed between the ligand and titanium. The chelating agents can have an impact on the stereochemistry of the molecule by directing sol-gel reaction to specific sites. This approach has allowed to synthesize a wide range of both crystalline and amorphous transition metal oxide structures.[62]

1–2.3.2   Materials from sol–gel chemistry: processing, post-processing and templating

There are many ways to introduce desirable features in a gel that do not involve the chemistry. The physical treatment of the prepared gel specifically the rate of evaporation can change the structure drastically. Drying the sample via heat treatment is also an important factor since it allows the removal of surface hydroxyl groups. This approach can produce a ceramic monolith or convert gel to a crystalline material.

Stober has shown previously that the processing of sols or gels can be as simple as fast stirring, which can result in the formation of small particles.[63] One more approach is to convert the solvent filled into a dry solid.

Permeability of the gel to the liquid flow in the highly porous structure is one of the factors that affects the rate of contraction or shrinkage.[64] Darcy's law can be used to describe the flux of fluid in a porous material.

$$q = \frac{K}{\mu L}\Delta p \qquad\qquad\qquad (2.1)$$

In this equation, K is the permeability, Δp is the pressure drop over a distance L and μ is the dynamic viscosity of the fluid. For the alkoxide derived gels, the permeability of very small pores is very low. During the syneresis processes, condensation reactions occur in which the solid phase forces the liquid phase out of the pores. This phenomenon happens since the liquid blocks the contraction of the porous network. Near the surface, it is much easier for the liquid phase to escape but it is much more difficult for the liquid to flow from the interior resulting in higher shrinkage rate near the surface. If the condensation reaction is accelerated by increasing the temperature, the porous network imposes a large stress on the liquid but the liquid flow rate might not increase. In this scenario, the network stiffens without much shrinkage. This also explains why the activation energy for the condensation reaction is two times higher than the activation energy for syneresis.[65–67]

To obtain pores with large volume, supercritical drying method can be carried out. The product obtained from supercritical drying is called aerogel, which is 98% air by volume. We can also create a variety of nanostructure materials by using supercritical fluids as the medium for sol-gel synthesis. Applying freeze drying results in creating cryogel, which is a highly porous material. Cryogels have porosity levels between aerogels and xerogels.[68]

Templates can also be used to engineer the structure of sol-gel chemistry to create both ordered and disordered pores. The most common additives used are the soft templates. Amphiphiles, block copolymers, ionic liquids, biopolymers and proteins are a family of soft templates. On the other hand, hard materials can also be applied to engineer the structure of the pores. Bacterial filaments, cellulose nanocrystals and colloidal particles have been used as hard material for such purposes. To create a material with multiple length scale porosity, alkoxides can be modified to improve the interaction of sol-gel precursors with both a soft template and hard template. Leaving the template in the sol-gel solution can result in the creation of an organic inorganic nanocomposite. There are also various approaches that can be taken to remove the template such as calcination or dissolution. Different chemical moieties can also be introduced during the sol-gel process to

functionalize the material while templating is incorporated. This approach is very useful in that sense that the an ordered or disordered material is created, which has molecular recognition sites.[69]

1–2.4   Experimental Techniques

1–2.4.1   Electrochemical impedance spectroscopy

Electrochemical impedance spectroscopy (EIS) is a non-destructive technique that can be used to model and understand the processes occurring in lithium-ion battery systems. Such processes usually involve the dynamics of mobile species in various regions of the system. Specifically, the dynamics of the bulk and interfacial regions play an important role in battery systems. The wide usage of EIS relies on the ability of the technique to deconvolute complex electrochemical processes into rather simple process characterized by distinct relaxation times. It is important to mention that the system must stay in a stationary state once the EIS measurement is applied. To not disturb a stationary state, a small amplitude potential or current is applied, which excites the electrochemical system at various frequency ranges. Measuring the response of the system results in obtaining a transfer function, which is the impedance.

- *Theory, Methods and Analysis*

During an EIS measurement, a small sinusoidal potential $E(t)$ is applied to a given electrochemical system. The response obtained, which is a linear current density function $j(t)$, has the same frequency as the input function but different phase and amplitude shown in the figure below. The ratio of these two different quantities is defined as the impedance $Z(t)$ [2.2], i.e.,

$$Z(t) = \frac{E(t)}{j(t)} \tag{2.2}$$
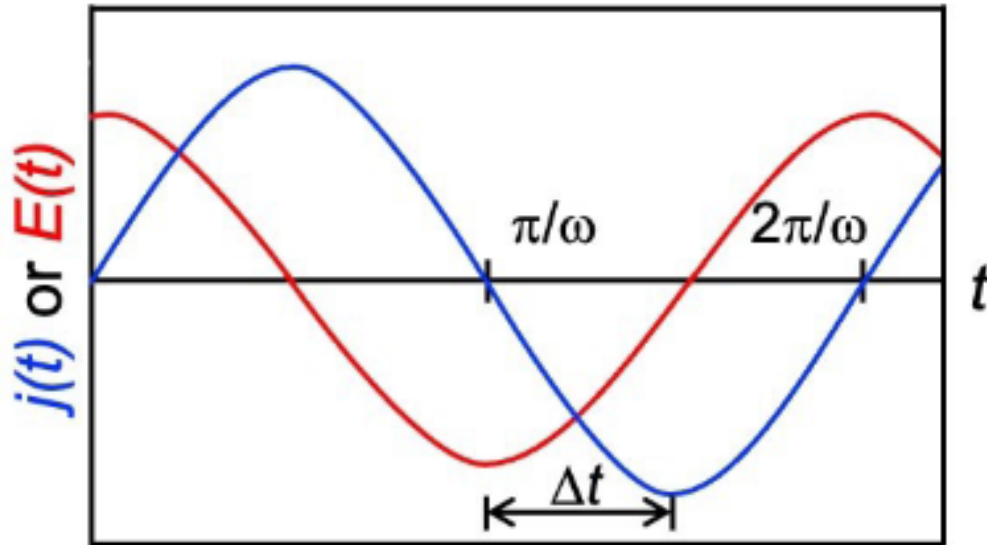
Figure 1.4 Plot describing the relationship between the input voltage, E(t) and output current, j(t) (or vice versa), the ratio of which results in impedance.

This experiment reports fast processes at high frequencies such as ion migration while slower processes are observed in the lower frequency domain.

For potentiostatic EIS, the alternating voltage can be written as the following : $E(t)=|\Delta E|\sin(\omega t)$. $|\Delta E|$ is the voltage amplitude, ω is the angular frequency and t is time. Generally, two important assumptions are made when small amplitude perturbation (< 50 mV) are applied to the system: (i) The input and the output have the same mathematical form (ii) The input and output do not have a nonlinear relationship, irreversible chemical changes are not applied to the system when investigated. If we apply the Kramers-Kronig relations, we can verify the validity of these assumptions. In this case, $j(t)=|\Delta j|\sin(\omega t+\Delta t)$ where $|\Delta j|$ is the amplitude of current density, Δt is the phase difference and $\omega t+\Delta t$ is the phase angle. The functions j(t) and E(t) contain magnitude and phase information as a result Z(t) is a complex number that can be described using real and imaginary components.

- *Impedance Plots*

Nyquist and Bode plots are used to represent the complex set of data. These plots are complimentary to each other. For instance, the Re(Z), Im(Z) and the modulus of

Z are related based on the following equation (Eq. 2.3):

$$|Z(\omega)| = \sqrt{Re(Z(\omega))^2 + Im(Z(\omega))^2} \qquad (2.3)$$

Also, ϕ as a function of ω can be expressed using the real and imaginary value of impedance (Eq. 2.4)

$$\phi(\omega) = \tan\frac{Re(Z(\omega))}{Im(Z(\omega))} \qquad (2.4)$$

We can use these derived quantities to analyze of the experimental data. Using an equivalent circuit to model the electrochemical process is a practical way to deconvolute the processes and associated characteristic time constants. A resistor and a capacitor in parallel, RC circuit, is a common element combination, which is widely used to model the electrochemical systems.
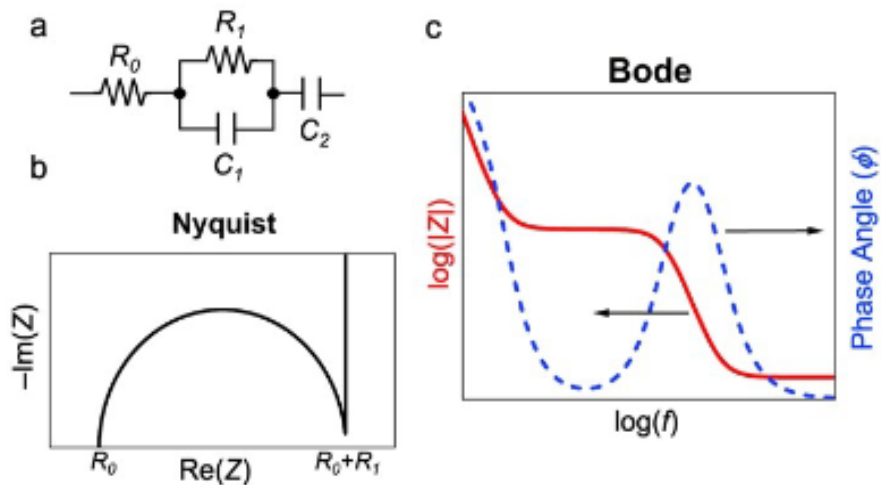
Figure 1.5 a) Equivalent circuit for single electron transfer and ion migration in the electrolyte. b) Nyquist plot of the real impedance against the imaginary impedance showing the resistance for the electrolyte. c) Bode plot of the magnitude of the impedance and phase angle against frequency.

As shown in Figure 1.7, the symmetrical arc is offset from the origin on the horizontal axis. This offset, Ro ,
is due to the resistance of the wires or the contacts. The time constant of the conduction processes can be
obtained from the frequency at the apex of the semicircle, $\tau = (RC)$, Capacitor, C_2 shows as a vertical line at
low frequency. Bode plots is advantageous since the obtained EIS data is presented in the time domain. This
allows relating some of the specific impedance events to their associated time constants.

1–2.4.2   Brillouin Light Scattering

The research by a previous group member revealed that the adiabatic elastic modulus of a solid ion
conducting material strongly correlates with the activation energy for cation hopping.[52] This led us to develop
an improved theory describing cation transport in amorphous materials, rooted in transition state theory
(TST). Measurement of the adiabatic elastic moduli of materials we develop or application as ion conductors
is therefore an important diagnostic tool for assessing performance characteristics and for understanding the
fundamental principles underlying materials design.

Brillouin light scattering (BLS) yields both the longitudinal and shear modulus in their adiabatic limit. BLS is a
non-destructive technique which relies on the interaction of incident light and acoustic phonons of the
probed material. This technique probes the propagation of plane-wave elastic deformations, or phonons, and
yields the velocity of sound. Multiplying the square of the velocity with the density of the material then gives
us the elastic modulus. Furthermore, the technique allows one to select the direction and wavelength of the
phonons that are probed, based on the scattering geometry. This is based on the fact that the total
momentum is preserved during the scattering processes. Since both sound and light can be described as wave
phenomena, the momentum balance can be simply expressed as the vector difference, $q = k_s - k_i$, where q is
the phonon wavevector, and k_s and k_i are the wavevectors of the scattered and incident light, respectively.
This construct is also known as the diffraction condition, and is illustrated in the magnification circles (Figure
1.9), which shows it for two different scattering geometries.

The measurement yields a spectrum with up to three peaks, one due to scattering by longitudinal waves and the other two by shear waves (for an elastically isotropic medium, there is only one shear peak). These peaks are shifted relative to the elastically scattered light by a frequency ω, which is proportional to the velocity of sound. Hence the elastic modulus is obtained as

$$M' = \rho_0 \omega^2 / q^2 ,$$

where ρ_0 is the equilibrium density of the scattering medium, and the wavevector is calculated as

$q = 2n/\lambda \sin\alpha$, where n is the refractive index of the material, λ is the wavelength of the probing light, and α is the scattering angle as defined in Fig. 1.6
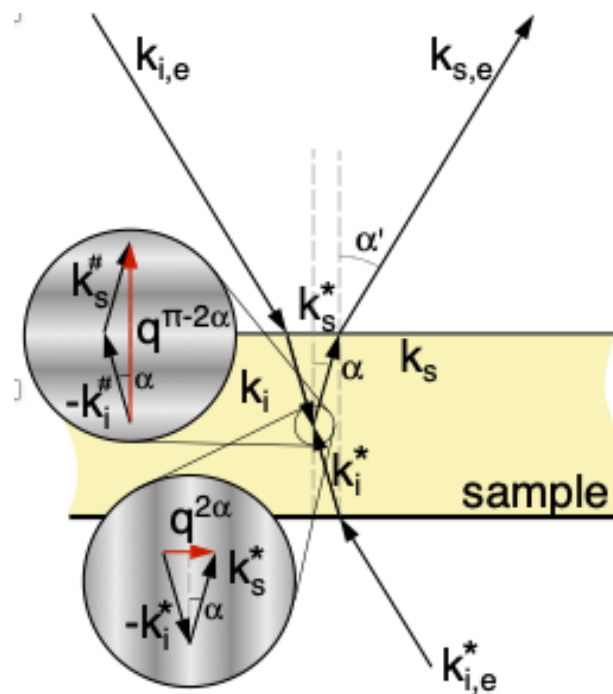
Figure 1.6   Schematic of diffraction conditions

We use two scattering geometries; one is the so-called platelet geometry, where light enters the sample on one side and exits on the opposite side, while both beams form the identical angle with respect to the plane normal. This yields the in-plane modulus, as illustrated in the lower magnification circle. The other geometry

is called platelet complement, and different only by the fact that light enters and exits the sample on the same side. This yields the out-of-plane modulus as illustrated in the upper magnification circle (Fig 1.6).

Since this technique probes the visco-elastic response of the material in GHz frequency regime, the structure of the material does not have enough time to relax. Furthermore, no heat is added or withdrawn during the scattering processes, which confirms this approach results in probing the adiabatic moduli of the given material. The wavelengths of the phonons used to vibrate the structure of the xerogels are about 200 nm. This means that during the oscillatory motion, the molecular structure of xerogels compresses and extend to approximately 100 nm. Measuring the elastic moduli of the material using BLS, it is equivalent to probing the mechanical response of many dog bone samples that are 100 nm long (Figure 1.7)
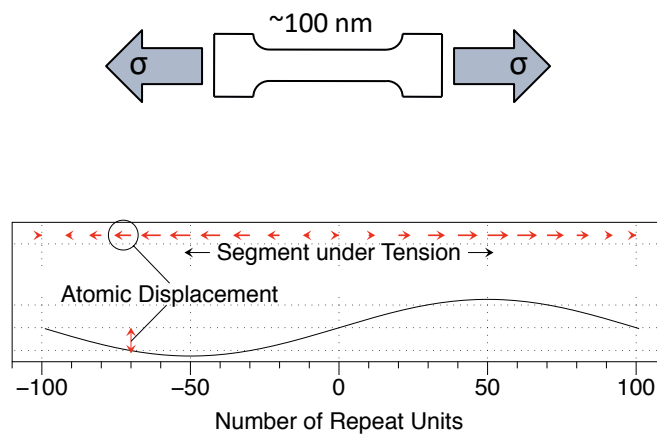
Figure 1.7   Oscillatory straining of specimen in nanoscale using Brillouin light scattering

1–2.4.3   X-ray Scattering

X-ray scattering is used to reveal important information regarding the elemental and atomic information and the structure of a material. When a powder or a monolith is illuminated by x-rays, complex patterns can be formed from the deflected or scattered x-rays. The changes in polarization, intensities, and angle of (incident vs scattered x-ray beams) are used to extract information regarding the material.

18

X-ray scattering is a non-destructive technique that can be applied on a wide range of materials starting from simple repeating inorganic crystals to complex composites made of polymers. This technique allows one to obtain information regarding the porosity, dispersity, shape, size, morphology of the investigated materials.

Once x-rays collide with the electron, the scattering events occur meaning the more electrons available within the material, the highly the likelihood of scattering. The differences in the density of the electrons with a sample can result in contrast. If the scattered x-rays have the same characteristic such as the energy and the wavelength of the incident x-rays, the event is elastic scattering. However, in inelastic scattering, the opposite is true.

Depending on the angle of elastic scattered x-rays, various information can be obtained regarding a material. Small angle X-ray scattering (SAXS) uses very small angles 0.1-10**°**. Wide angle X-ray scattering relies on larger angels that are usually > 10**°**.
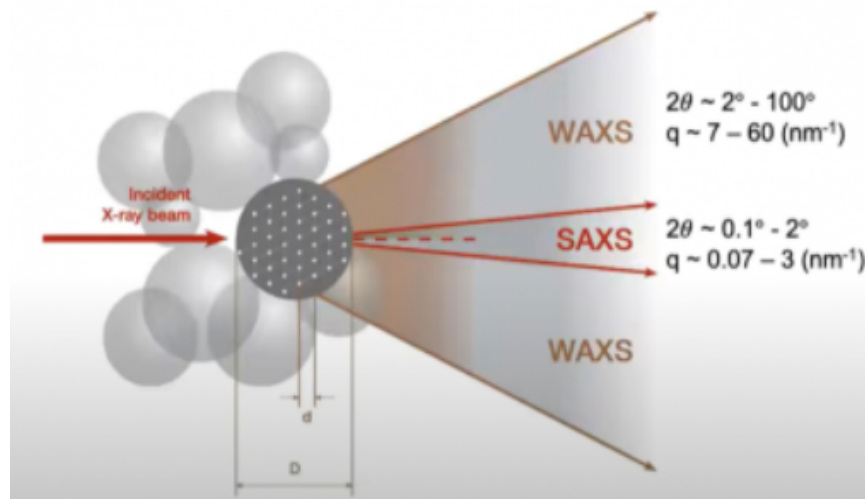
Figure 1.8   SAXS and WAXS achieve different resolutions, with WAXS measuring wider angles, and achieving atomic resolution, and SAXS measuring very small angles and achieving nanoscale resolution [70]

The information regarding the lattice spacing of the crystals is obtained using Bragg's equation:

$n\lambda = 2dsin(\theta)$

in which θ is scattering angle, λ is the X-ray wavelength, d is the spacing distance between structures.

1–2.4.4   Thermogravimetric Analysis

Thermogravimetric analysis (TGA) is an analytical technique widely used to determine a material's thermal stability and its fraction of organic or inorganic volatile components by measuring the weight change that occurs as the material is heated at a constant rate. The thermal decomposition of the material can be tracked as temperature changes. Furthermore, TGA can be used to track the presence of volatile solvents and water. The apparatus consists of a very sensitive scale to measure weight changes and a furnace that can be programmed for a desired heat flow rate. The balance needs to be thermally isolated and is usually located above the heating system. A pan is positioned at the end of a hang-down wire with a required reproducible position. We can couple an infrared spectrometer to the TGA instrument to identify the volatile species.

1–2.4.5   Differential Scanning Calorimetry

Differential Scanning Calorimetry (DSC) is a thermal analysis technique that probes the changes in the heat capacity of a material as temperature changes. A sample of known mass is heated or cooled and the changes in its heat capacity are tracked as changes in the heat flow. This technique detects the transitions that are occurring in material such as glass transition, various phase changes and curing. Amorphous materials such as glass have no organization in the solid state – it is random. This gives it the transparency that glass has, among other properties. As you warm it up, its heat capacity increases. At some point you have enough energy in the material that it can be mobile. This requires a fair amount of energy compared to the baseline increase, although much less energy than the melting point does. This energy normally appears as a step change in the instrument baseline – pointing up in heat flow instruments and down in heat flux.

The biggest advantage of DSC is the ease and speed with which it can be used to see transitions in materials. If you work with polymeric materials of any type, the glass transition is important to understanding your material.

CHAPTER 2   Bonded *vs.* Non-Bonded Hybrid Organic-Inorganic Solid Electrolytes

2–1   Introduction

Composite solid electrolytes are viable candidates to replace liquid electrolytes, which are flammable and provide low mechanical strength. Crystalline ceramic electrolytes show high ionic conductivities (> 10^{-4} $S.cm^{-1}$), wide electrochemical stability (>5.0 V vs. Li/Li$^+$) and good chemical stability. However, their poor mechanical properties, such as brittleness, make it costly to mass produce ceramic electrolytes.[71] Conversely, polymer electrolytes consist of amorphous and crystalline regions. The presence of the crystalline domains at room temperature lowers the ionic conductivity of solid polymer electrolytes, ultimately requiring the dispersion of mechanically stiff nanoparticles to prevent the formation of such domains. Hence, taking advantage of the desired properties of organic and inorganic materials in a combined fashion, we focus on developing a composite materials design approach, aiming to address the individual issues inherent to SSEs. In this chapter we introduce the methodology for preparing composite electrolytes that have high mechanical strength and a wide electrochemical window.

Rather than dispersing ceramic nanoparticles into a polymer matrix, we infiltrate the organic phase into the pores of the inorganic backbone, where its ability to organize into crystalline domains is equally inhibited. Finally, the nano porous inorganic backbone offers the required mechanical rigidity, which has an adiabatic elastic modulus in GPa ranges, characteristics to suppress dendrite growth.

2–2   Objectives

In preceding research within our group, hybrid organic-inorganic solid electrolytes were successfully synthesized using a one-pot method. The basic constituents were sol-gel derived silica (based on tetraethoxysilane, TEOS) and polyethylene glycol. The ionic transport properties of systems where no

covalent bonds formed between the organic and inorganic phases formed were compared with those of systems where such bonds developed. Such bonding was achieved using methoxy polyethylene glycol amine (MPEG-NH$_2$) and 3-Isocyanatopropyl)triethoxysilane (IPTS, Aldrich), 3-Glycidyloxypropyl) trimethoxysilane (GLYMO) reagents, where the latter incorporates into the silica structure during polycondensation and MPEG-NH$_2$ anchors to these groups. The comparison revealed that the system with anchored PEG chains exhibits more than an order of magnitude higher ionic conductivity, and this difference was attributed to the fact that when charge carrier phase is not chemically bonded to the backbone, the salt anion is subject to electroosmotic drag, which slows the Li$^+$ migration and reduces its transference number.

However, small-angle x-ray scattering showed that the silica phase that formed during the one-pot synthesis consists for the most part of isolated clusters rather than a percolating three-dimensional network. Such a material may not provide the desired elastic stiffness. Hence, in the present investigation we devised a two-step synthesis route, in which a nano-porous continuous backbone is first formed via sol-gel synthesis providing the loadbearing capability. This backbone is subsequently infiltrated with polyethylene glycol to establish the conducting phase. Here, we also compare the properties of materials with and without covalent bonding between organic and inorganic constituents. Hence our research objectives are:

(i) to confirm feasibility of this two-step synthesis route,

(ii) identify the optimal polymer chain length for maximizing the polymer content of the electrolyte, and

(iii) to establish the effect of these bonds on materials performance

2–3 Synthesis

2–3.1 Reagents

The materials used for this study are all reagent grade and can be purchased commercially. Tetraethylorthosilicate (TEOS, > 98%), Poly-(ethylene glycol) [PEG 400, 600, 1000, 2000, 6000 and 10000 g mol^{-1}] , hydrochloric acid (HCl) were purchased from Sigma-Aldrich. Lithium Perchlorate (battery grade, dry,

99.99% trace metals basis) was kept under vacuum at 50 °C and purchased from Sigma-Aldrich. Ethanol

(200% proof) was purchased from Fischer Scientific.

2–3.2   Two-Step Synthesis of Hybrid Electrolytes

- *Step-1*

The synthesis of the inorganic backbone is performed by modifying the method found in the literature.[72]

This consists of mixing TEOS (13.8 g, 0.0663 mol), ethanol (12.9 g, 0.28 mol), water (2.19 g, 0.28 mol) for 30

minutes. Then, HCl (1M, 0.0007 mol, 0.71 g) is added dropwise and the solution is stirred for 48 hours at 60

°C. After the gelation process is initiated, the solution is cast into molds consisting of Teflon o-rings with

inner diameters of 18 or 36 mm. The gelation is completed, the samples are aged for three days and washed

with ethanol to remove unreacted TEOS.

- *Step-2*

To infiltrate the pores of the obtained sol-gel samples from step 1, solutions of poly (ethylene oxide) with

different molecular weights are prepared using ethanol as solvent. The polymer phase is introduced into the

porous inorganic backbone obtained from step-1 via solution exchange. The polymer solution is renewed

every few hours for about two days. As the polymer penetrates the silica network, the amine groups of the

mPEG-NH$_2$ encounter GLYMO moieties that dangle from vertices of the network. The epoxy ring in

GLYMO is then expected to react with the amine according to scheme 2.1, which was verified by FTIR.
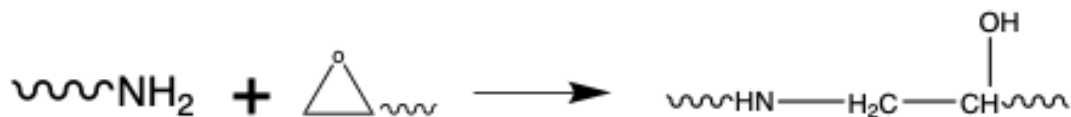
Schematic 2.1 Schematic of the reaction of epoxy ring (available in GLYMO) with the amine group in mPEG-NH$_2$

- *Post-synthesis Drying Processes*

The cylindrical shaped gels obtained after the step-1 and step-2 are placed in a petri dish and kept at room temperature for approximately 24 hours. After 24 hours, the samples are moved to a vacuum oven and the temperature is increased gradually to 75 °C, while the pressure is decreased to a low vacuum of at most –65 kPa.

2–4   Materials Characterization

A Jasco Fourier Transformed infrared (FT-IR) 4100 was used to obtain the spectra of xerogels over the range of 400-4000 cm^{-1}.

Differential Scanning Calorimetry (DSC) and thermogravimetric analysis were performed using TA instruments. Tescan Rise scanning electron microscope (SEM) was used to obtain the micro-images of the pores of hybrid electrolytes.

XRD scans were made using the Cu Kα radiation (1.541 Å) operating at 40 kV and 100 mA in the range of 10°- 40° 2θ, and using a step width of 0.01°. Impedance spectroscopy performed to determine the ionic conductivity. To this end, samples are placed in between two polished stainless steel blocking electrodes and are measured using a Novocontrol broadband dielectric impedance spectrometer at temperatures from 0°C to 80°C, in the frequency range from 0.1 Hz to 10 MHz.

2–5   Results and Discussion

In this work, hybrid composite electrolytes with various compositions were developed and characterized. TGA reveals both the mass fraction and the volume fraction of organic phase in the composite structure. A control group of polymerized TEOS (100 .wt%) was used to estimate the amount of water loss due to residual OH groups, which was subtracted from the weight loss in the hybrid composite. FTIR is used to gain insight with respect to molecular structures of the hybrid nanocomposite electrolytes, in particular as to the extent to which covalent bonds form between the organic and inorganic components. The degree of

crystallinity of the polymers in the composite electrolytes is assessed using XRD. SEM imaging serves to visualize the morphology of the pores of the xerogels.

2–5.1 Ionic Conductivity
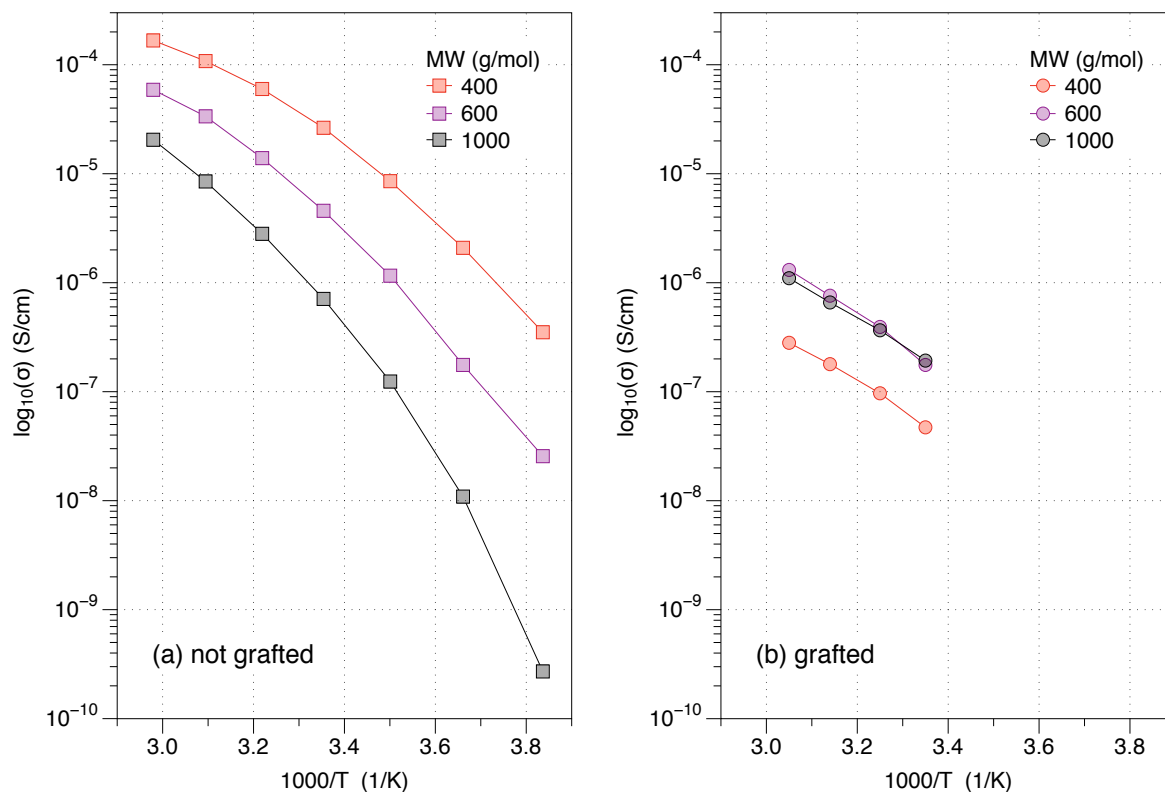
Figure 2.1 Ionic conductivity of hybrid silica-PEG nano-composite as a function of the reciprocal temperature and for different chain lengths, with (a) PEG not grafted to the backbone, and (b) with mPEGNH$_2$ grafted through the epoxy-amine reaction.

Ionic conductivity represent the key property scrutinized during this investigation. We first address the question as to whether anchoring the polymer to the backbone via GLYMO–mPEG-NH$_2$ mechanism does indeed improve the ionic conductivity of the hybrid electrolyte, as suggested by the behavior of the one-pot synthesized material in preceding work. Despite numerous efforts and variations of synthesis and processing parameters, this could not be ascertained in a satisfactory manner. We illustrate why by using two sets of representative data shown in Fig. 2.1(a) and (b), which show the ionic conductivities of hybrid silica-mPEG-

NH$_2$ nano-composite as a function of temperature, with (a) PEG not grafted, and (b) with it grafted to the backbone. The figures have the same size and scale to show the difference between the data sets.

Note that the synthesis and measurement of grafted system took place first, at a time when the significance of this information was not yet clear, and the chosen temperature range was limited. However, the important differences are still evident. Evidently, the data for samples with grafted and not grafted polymer exhibit markedly different conductivity magnitudes, the latter being at least an order of magnitude higher in the measured temperature range. At first glance, therefore, it would seem that anchoring the conducting phase to the backbone does not result in improvement of ionic conductivity. However, the temperature dependences of these two data sets also differ significantly. First, all data deviates from Arrhenius behavior, showing distinct curvature. For the materials without grafting, data for the three molecular weights vary between three and five orders of magnitude between the freezing point and 70ºC. Conductivities increase monotonically with decreasing molecular weight. Since the glass transition temperature decreases with molecular weight, one would expect the cation mobility to vary in this order. Furthermore, the curves bundle at high temperature and fan out at low temperature, which reflects consistency in the transport mechanism. (This latter point will be expanded upon in the next sub-section.) Conversely, the slopes in the data for grafted polymer are smaller, and the order in terms of molecular weight and T_g is not preserved. In combination, this is indicative that the material's development has somehow been constrained by factors unrelated to its molecular makeup. In the following we provide further information in support of this assertion.

2–5.2   Visual inspection
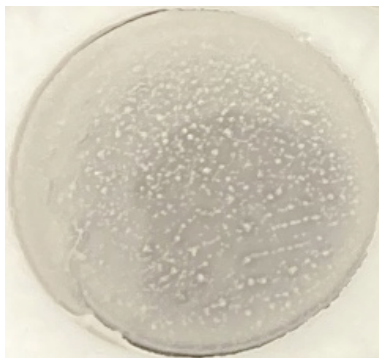
Figure 2.2   Image of a hybrid electrolyte sample based on the GLYMO-mPEG-NH2 grafting chemistry

Figure 2.2 shows a photograph of a sample obtained when pursuing grafting via the GLYMO-mPEG-NH$_2$

chemistry. Note how the upper edge and small patches across the entire surface appear white and opaque.

This is the result of micro-pore formation with sizes exceeding the diffraction limit. In other, words the

material has a significant amount of voids that represent obstacles to cation transport. Along the same lines,

the radial contraction of this material is about 50%, respectively, a 75% volume contraction. By comparison,

we find that for materials filled with PEO that is not grafted to the backbone, the radial shrinkage is only

38%, corresponding to a 61% volume shrinkage. Hence, when grafting polymer to the backbone, pores seem

to be filling to a significantly lesser degree, which is consistent with the observed lower ionic conductivity.

2–5.3   IR Spectroscopy

Indeed, the question arises whether during the solvent exchange, the mPEG-NH$_2$ actually reacts with the

GLYMO groups that have been incorporated into the silica backbone. Such a reaction would consume the

epoxy oxirane rings and the amine groups. We attempt to answer this question in a semi-quantitative way

using results from IR spectroscopy. The top part of Fig. 2.3 shows the IR spectra of a TEOS-PEG mixture

and of GLYMO as a black and a green line, respectively. The red trace in the bottom part is the spectrum for

the hybrid material obtained using GLYMO-functionalized silica and mPEG-NH$_2$ as the reagents. The

intensity increase of peaks associated with alcohol groups notwithstanding, a linear combination of the two

spectra from the top of the figure should approximately yield the red spectrum on the bottom, assuming that no epoxy-amine reaction did occur. The factors for the linear combination are chosen such that magnitudes of peaks associated with molecular groups that remain unaltered during the process match. Accordingly, we scale the spectra using the sum of the Si-O-Si stretching mode intensities and the CH_2 stretching mode intensities as our reference.

Comparing the resulting linear combination, represented by the blue trace, with the spectrum for the synthesized hybrid material, we see that the mode associated with the oxirane ring, around 790 cm^{-1}, decreases in intensity for the hybrid (marked by green rectangle). This suggests that some anchoring of mPEG-NH$_2$ does take place during this two-step synthesis. But, since the intensity of the 790 cm^{-1} band does not completely vanish, we conclude that some fraction of GLYMO groups remain unreacted.
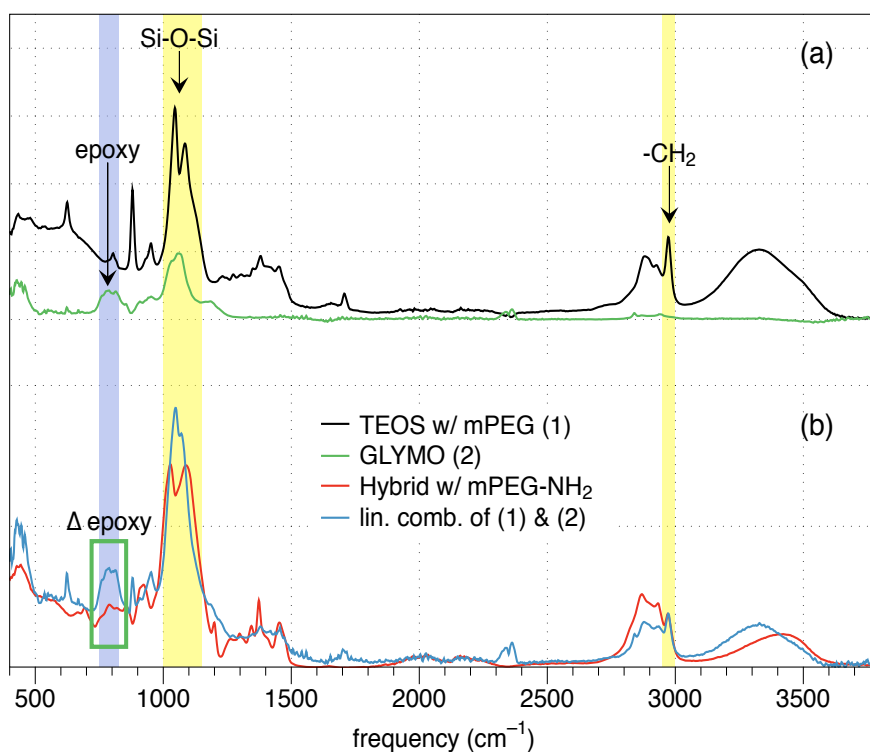
Figure 2.3 IR spectra of (a) a TEOS-mPEG mixture and GLYMO, and of (b) the hybrid that results from reacting GLYMO-functionalized silica with mPEG-NH$_2$, overlayed with a linear combination of the two spectra shown in (a).

2–5.4 Analysis of the temperature dependence of ionic conductivity

To further elucidate the differences between samples that have polymer grafted to the backbone and those that have not, we examine the information that can be gained from the temperature dependence of the ionic conductivity. First, we provide an introduction to a new approach we developed to carry out this analysis.

2–5.4.1 Variable activation Gibbs free energy

In crystalline materials the temperature dependance of ionic transport is well described using the Arrhenius relationship,

$$\sigma T = \gamma / k_B \, \rho \left(z q_e d_0 \right)^2 v_D e^{S_a/k_B} e^{-E_a/k_B T} = \sigma_0 e^{-E_a/k_B T} \Leftrightarrow \ln\left(\sigma T\right) = \ln \sigma_0 - E_a / k_B T = \ln \sigma_0 - \beta E_a, \qquad (2.1)$$

where γ is a geometry coefficient that is equal to $1/2$ for diffusion in one dimension, and equal to $1/6$ for diffusion in three dimensions, d_0 is the average jump distance, which has a negligible temperature dependence within the range that we consider, and v_D is the attempt frequency, for which that of a fundamental mode of motion of the element in question within this structure, e.g., the Debye frequency, is often used. Furthermore, E_a and S_a are the activation enthalpy and entropy, respectively, and k_B is the Boltzmann factor. Seen in the context of transition state theory (TST), Eq. (2.1) is evidence for the fact that ionic transport occurs via a hopping mechanism and can be used to extract the associated activation enthalpy, E_a, from the slope of $\ln(\sigma T)$ *vs.* the reciprocal temperature. However, in amorphous materials, especially in the supercooled liquid regime where the materials are transitioning from liquid to glass, the temperature dependence of the ionic conductivity tends to deviate from Arrhenius behavior, exhibiting marked curvature and thus precluding the identification of a unique characteristic slope.

To still achieve good fits of their data, researchers modified the Arrhenius equation. One of the best-known forms is the equation proposed by Vogel, Tammann, and Fulcher (VTF),[73–75]

$$\sigma T = A e^{-B/(T-T_0)} \Rightarrow \ln\left(\sigma T\right) = \ln A - k_B B / k_B T \left(1 - T_0 / T\right),$$

or

$$\ln(\sigma T) = \ln A - \beta k_B B / (1 - \beta k_B T_0),$$ (2.2)

which adds a shift in the temperature scale to T_0 as the origin. The resulting expression successfully

reproduces the non-linearity in the $\ln(\sigma T)$ *vs.* $1/T$ plot on account of the fact that it introduces a singularity at

T_0. The data fit yields the parameters A, B, and T_0, which can be used to interpolate between data points.

However, the physical meaning of these parameters remains elusive. The temperature T_0 does not reliably

correlate with the glass transition or the Kautzmann temperatures.[76, 77] Most importantly, the parameter B in

eq. (2.2) does not yield the activation energy in the statistical mechanical sense of representing the energy

barrier the system must overcome to allow for the cation to hop from one site to the next.[78] Indeed, the fits

of various expressions discussed here reveal that the best fit of an Arrhenius-type expression and the VTF

equation show that $B \cdot k_B$ and E_a differ by about an order of magnitude. Even the factor $\ln A$, which

corresponds to $\ln(\sigma T)$ when $T \rightarrow \infty$, is strongly influenced by T_0. Most importantly, the VTF equation is

inconsistent with TST, in that it removes part of the available thermal energy from the comparison with the

activation energy when evaluating the probability for a cation jump to be successful.

Being mindful of the structural changes that occur in the glass transition regime, we have therefore adopted a

different approach for analyzing the temperature dependence of ionic conductivities. A brief derivation of this

approach is given here. Firstly, as soon as the $\ln(\sigma T)$ *vs.* β data exhibits finite curvature, data fits using an

arbitrary function, say the VTF equation, will extrapolate to different intercepts with the ordinate at $\beta = 0$

depending on the high-temperature cut-off in data collection. Hence, it is necessary to account for a possible

temperature dependence of σ_0, and according to Eq. (2.1), the only quantity in σ_0 that can exhibit a significant

temperature dependence is the activation entropy. We therefore must consider the Gibbs free energy of

activation. In differential form, the modified Eq. (2.1) is $d\ln(\sigma T)/d\beta = -G_a - \beta dG_a/d\beta$, i.e., the leading

term corresponds to the activation free energy. For systems exhibiting Arrhenius behavior only the leading

term on right hand side prevails; $dG_a/d\beta = 0$ and G_a is a constant independent of temperature. Conversely, a non-zero derivative $dG_a/d\beta$ causes curvature in $\ln(\sigma T)$ vs. β, and evidently, reflects a change in G_a with β. In other words, first and possibly higher order derivatives of G_a with respect to β must be non-zero.

To accommodate this conclusion, we developed a model in which the activation enthalpy and entropy are both temperature dependent. For practical reasons, it is preferrable to use a closed form functional dependence of the activation energy on temperature. To this end we pursue an approach based on a simple thermodynamic construct, in which we consider the transition from a liquid to a glass (or *vice versa*) as a rate phenomenon that possess both forward and reverse pathways. We therefore use Richard's generalized differential equation,[79] which was originally developed to describe growth phenomena, and is given by

$$\frac{d\psi(\beta)}{d\beta} = H\psi(\beta)\left(1 - \left(\psi(\beta)/A\right)^{\nu}\right). \tag{2.3}$$

This differential equation has the structure of a generic rate equation to describe the transformation from an unstable to a stable state. It has the solution

$$\psi(\beta) = A\left(1 + C_0 e^{-\nu H(\beta - \beta_C)}\right)^{-1/\nu}, \tag{2.4}$$

known as the generalized logistic function, where A, H, C_0, ν, and β_C are parameters. This construct has been employed in fields including epidemiology,[80, 81] behavioral sciences,[82] ecology,[83] economics,[84] and chemistry.[85] It can be shown that for $A = C_0 = \nu = 1$, we recuperate the expression for the relative proportions of a two-level system, which is a well known construct in statistical thermodynamics that is often used to illutrate general concepts in a simplified manner. Thus, we describe the variable activation Gibbs free energy (VAG) using $E_a(\beta) = \psi(\beta)\left(E_{a,R} - E_{a,V}\right) + E_{a,V} = \psi(\beta)\Delta E_a + E_0$, and similarly $\tag{2.5}$

$$S_a(\beta) = \psi(\beta)\Delta S_a + S_0. \tag{2.6}$$

Here we keep $A = 1$ for simplicity, while we adopt the values for $v = 12$ and $C_0 = 2.54$ based on experience. Similarly, $\beta_C = 1/(k_B T_C)$ is chosen to be slightly above the measured glass transition temperature, i.e. $T_C = T_g + 20$ K for consistency. Accordingly, we fit the measured data using

$$\ln(\sigma T) = P + S_0/k_B + \psi(\beta)(\Delta S_a/k_B - \beta \Delta E_a) - \beta E_0 , \qquad (2.7)$$

where H, ΔE_a, E_0, ΔS_a, S_0 are the five parameters to be optimized using a non-linear least square fitting

method, such as the Marquart-Levenberg algorithm. $P = \ln\left(\dfrac{\gamma p (z q_e d_0)^2 v_D}{k_B}\right)$ can be calculated with sufficient

accuracy from the basic structural and thermomechanical information of the materials. Given the nature of the fitting function, multiple sets of parameters yield resonable fits. We therefore typically conduct an exhaustive search for the lowest error fit, choosing several hundred combinations of intial values for the parameters, randomly chosen within realistic bounds.

Furthermore, the bounds are established using the approach illustrated in Fig. 2.4. The measured data is shown as blue circles on the right in Fig. 2.4(a). We begin by verifying the deviation from Arrhenius behavior (dashed black line) and also perform a fit using the VTF model (dashed orange line). Next we compute the derivative of the VTF function with respect to β to create a set of interpolated slope data (square symbols in Fig. 2.4(b)), and fit this data with the derivative of Eq. (2.7). The purpose of this is (i) to smooth the experimental data, (ii) to eliminate one of the unknown parameters S_0/k_B for this initial fit, and (iii) to establish an initial set of bounds for the activation enthalpy based on the extremes in the slopes. Finally, using the parameters so obtained, we perform the full optimization of all variable coefficients, by randomly varying initial guesses within the established bounds. If the search consistently returns a value at the edge of the bound interval,

The resulting VAG model function is shown as solid green line in Fig. 2.4(a). In our experience thus far, for most cases, the fit yields a slightly smaller error than the VTF model. However, more importantly, the VAG

model provides more realistic activation enthalpies and is able to resolve the activation enetropies. These quantities are shown for the illustration data set in the inset of Fig. 2.4(a).
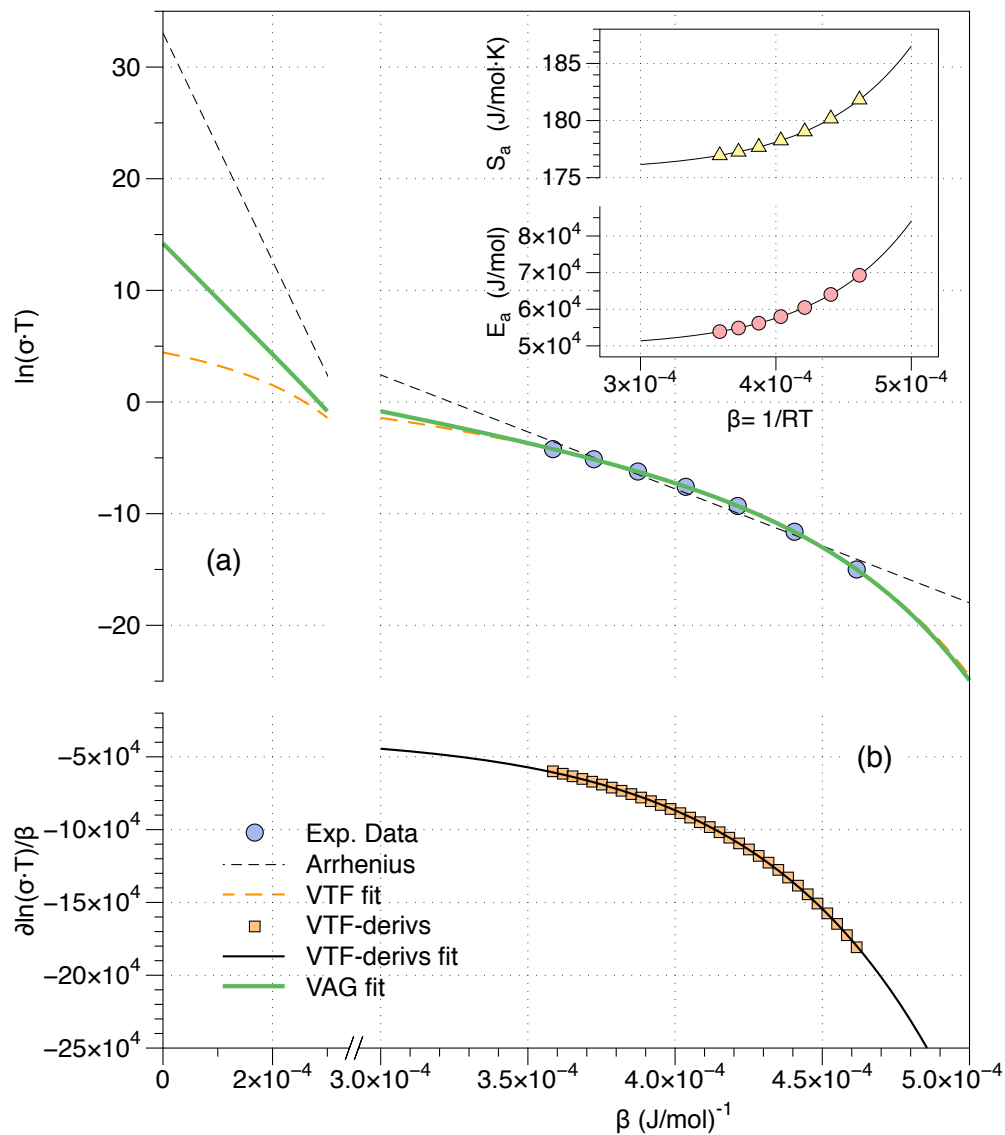
Figure 2.4   Illustration of the VAG model fitting procedure. (a) Measured data with Arrhenius, VTF, and VAG model fits. (b) Interpolated derivatives with respoect to β of the VTF model (square symbols) and fit of these derivatives using the derivative of the the VAG model

2–5.4.2   Activation Energy of Cation Transport in Grafted vs. Non-grafted Hybrid Electrolytes

We applied this analysis to the data shown in Fig. 2.1. The best fits and resulting activation enthalpies and entropies for cation hopping are plotted in Fig. 2.5 as a function of β. Again, all figure sizes and scales are maintained the same for comparison. As the plots reveal, for the systems in which polymer is not grafted to the backbone, activation enthalpies and entropies change significantly both as a function of temperature and the chain length of the polymer. The lowest values are associated with the smallest molecular weight, which is consistent with expectations that are based on thermophysical property trends, such as glass transition and melting temperatures. We also expect that in a homogenous phase, the conductivities converge at high temperatures onto a value that is dominated by the average jump distance, attempt frequency, and density, i.e., if quantities that depend on the structure and bonding characteristics of the material's molecular building block. We therefore conclude that this data is representative processes that occur in a well-formed polymer phase, close to its equilibrium density when contained in the pores of the silica backbone. Under these conditions, the dynamics of the structure is predominantly controlled by factors such entanglement, radius of gyration, and segmental mobility.

Conversely, the systems with polymer grafted to the backbone, variation in the activation free energy is small and exhibits no significant trend that would be reflective of the polymer chain length. In this case, the cation conduction process seems to be determined by factors other than the thermophysical characteristics of the polymer. Note that the activation energies are small, indicating that it is very feasible for cations to jump the activation barriers. Yet the conductivities are low, which suggests that few cations actually undertake a relatively easy task. This observation led us to conclude that significantly fewer transport pathways exist in the grafted materials. Hence, the way we can explain the observed behavior is that mPEG-NH$_2$ does not fill the pores in an efficient way. When the polymer is infused into hydrogel during the fluid exchange period in step 2, a large portion may react with GLYMO groups at the pore mouths, thus blocking other polymer from penetrating. As a result, the polymer volume fraction in these covalently bonded hybrid materials is lower

than in those where the polymer does not react with the backbone, i.e., where the polymer solution is less obstructed from entering the pores.
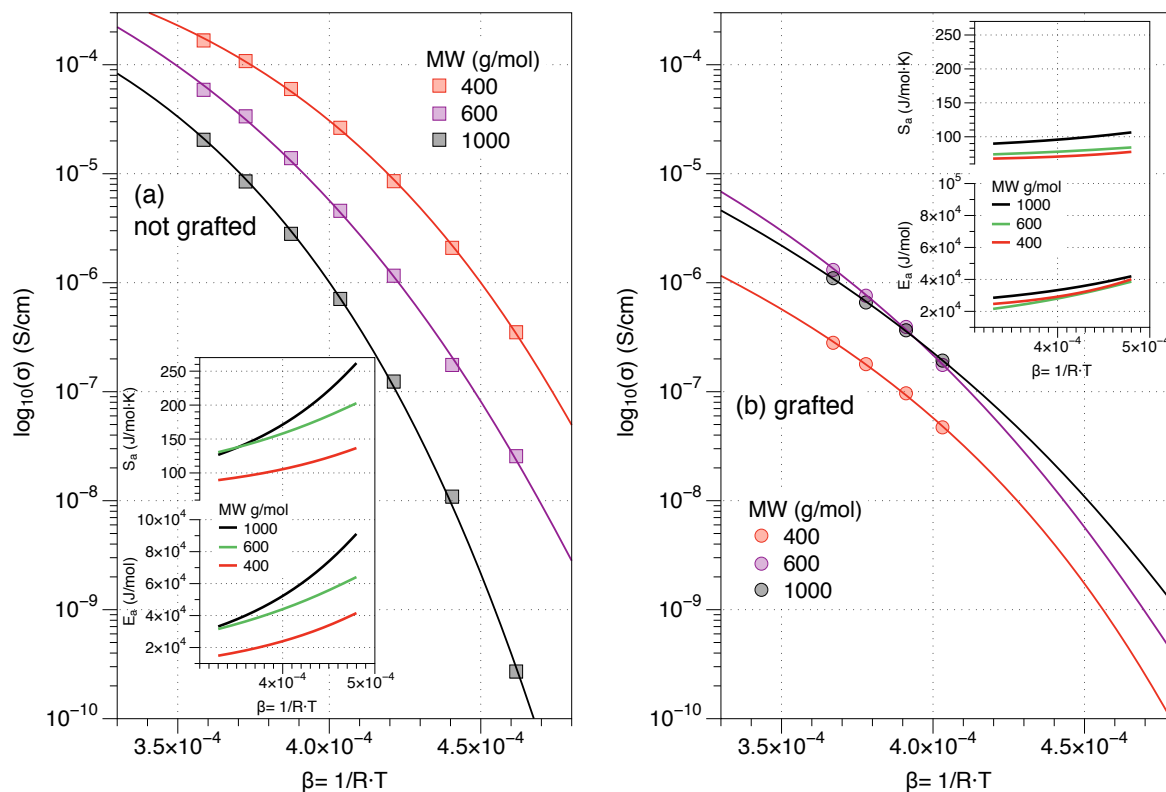
Figure 2.5　　　Fitting of the conductivity data for hybrid silica-PEG nano-composite as a function of the reciprocal temperature and for different chain lengths, with (a) PEG not grafted to the backbone, and (b) with mPEG-NH₂ grafted through the epoxy-amine reaction, using the VAG model. Inset: resulting activation enthalpies and entropies for cation hopping.

We found that all hybrid materials retain a small fraction of void space. In the case of hybrids loaded with mPEG-NH₂, this void space is not dramatically larger, but sufficiently large to obstruct cation conduction pathways. Hence, the behavior exhibited by this material is that of an electrolyte in which the cation hopping process is characterized by low-activation barrier, perhaps along the surfaces of pores, but where the effective conduction cross section severely limited.

2–5.4.3 Fill Factor for Hybrid Electrolytes Without Grafting Polymer to the Backbone

Focusing on improving ionic conductivity, one strategy is to maximize the conductive polymer content of the composite material. Since the inorganic scaffold of the material is characterized by a distribution of pore sizes, combining two or more different chain lengths of PEG may increase the volume fraction of organic phase in the composite and increase the ionic conductivity values. We therefore prepared solutions containing polymer with different chain lengths and chain lengths combinations to be used during the solvent exchange in step 2 of our process. The conductivity data for samples so obtained are shown in Fig. 2.6. This figure contains data for a representative selection of specimens, including the top performing compositions.
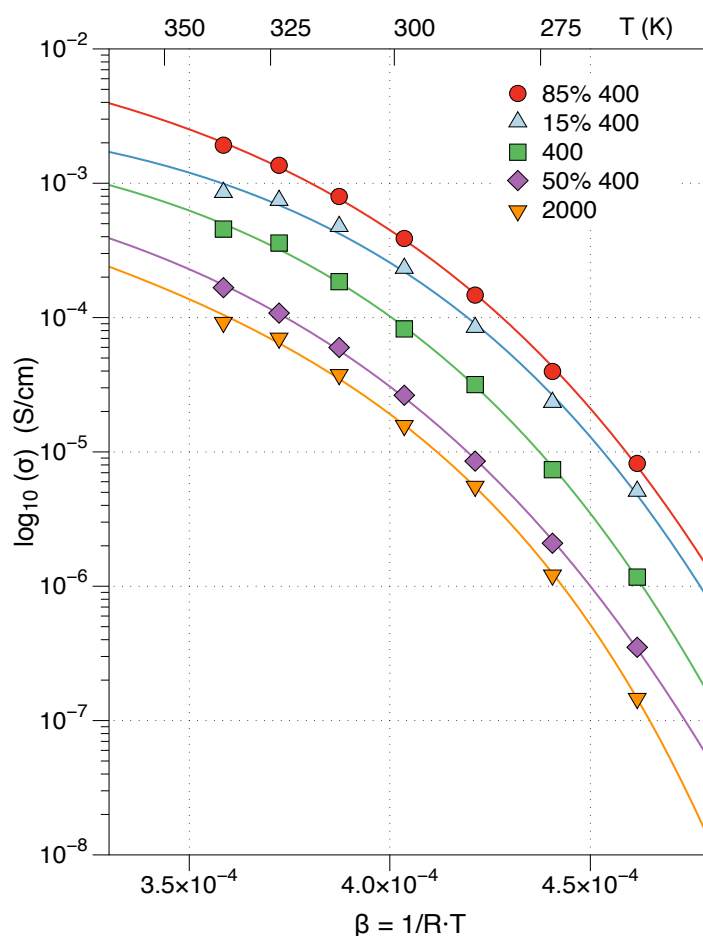
Figure 2.6 Ionic conductivity of hybrid silica containing PEG with molecular weights of 400 and 2000 g/mol, as well as different mixtures thereof. The solid lines are best fits using the VAG model.

Accordingly, the materials with disparate fractions of polymer type, i.e., with 85 wt% PEG400 and 15 wt.% PEG2000 and *vice versa* exhibit the highest conductivities. Interestingly, the 50/50 mixture has a lower conductivity than the hybrid uniformly filled with the shorter chain length. The hybrid containing the longest chain-length polymer shows the lowest conductivity.

Several factors can contribute to the observed behavior, including the degree to which pores are filled with polymer, as well as structural organization withing the polymer phase. Generally, as the organic content of the electrolytes is increased, it is expected the ionic transport efficiency to increase simply due to the density of conduction pathways. To verify whether combining two different chain lengths of PEG increases the volume fraction of the polymer in the composite, we determine the volume fraction of the organic and inorganic components of the material using a combination of thermogravimetric analysis (TGA) and tracking of reagent masses when preparing reaction precursors. We obtain the volume fraction of from the weight loss m_P during TGA, while the mass of the silica backbone, m_S, is determined upon drying (sacrificial) specimen after the first step of synthesis. Using the known densities of each phase, ρ_S and ρ_P, respectively, we calculate their partial volumes according to $V_P = m_P / \rho_P$, and $V_S = m_S / \rho_S$, and with that the volume fraction is

$$\Psi = \frac{V_P}{V_P + V_S}$$

The thermogravimetric traces used to determine the polymer volume fraction are shown in Fig 2.7. Accordingly, the hybrid electrolyte composed of 85 wt% PEG400 and 15 wt.% PEG2000 has the highest mass loss, and thus the largest volume fraction of polymer. The volume fractions of all specimens so determined are summarized in Table 2.1.
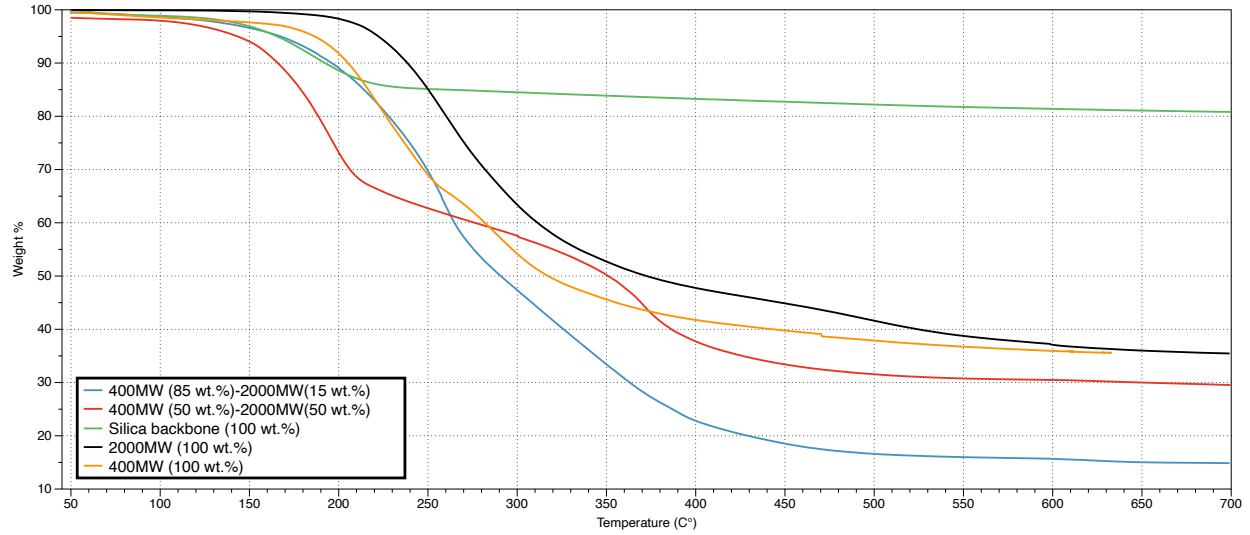
Figure 2.7　　TGA of hybrid electrolytes with 400MW PEG, 2000MW PEG and combination of 400MW PEG with 2000MW at two different relative weight fractions

1) Polymer molecular weight (g/mol)	2) $\Psi_{polymer}$
3) **2000MW**	4) 49.4%
5) **400MW**	6) 50.7%
7) **400MW (85 wt.%)-2000MW(15 wt.%)**	8) 60.7%
9) **400MW (50 wt.%)-2000MW(50 wt.%)**	10) 57.3%
11) **10000MW**	12) 38.8%

Table 2-1　　Summary of polymer volume fraction for hybrid electrolytes containing PEG

2–5.4.4　Morphology

Scanning electron microscopy was used to characterize the structure of hybrid electrolytes to understand the changes in the post structure due to post synthesis process. The drying processes affect the pore structure of the material differently on the surface versus the interior of structure. The pores on the surface of the material are completely collapsed (Fig 2-8 (a)). However, as it is shown in the image below (Fig. 2.8 (b)), the nano pores in the interior of the sample are available and provide the pathways for lithium ion hopping.
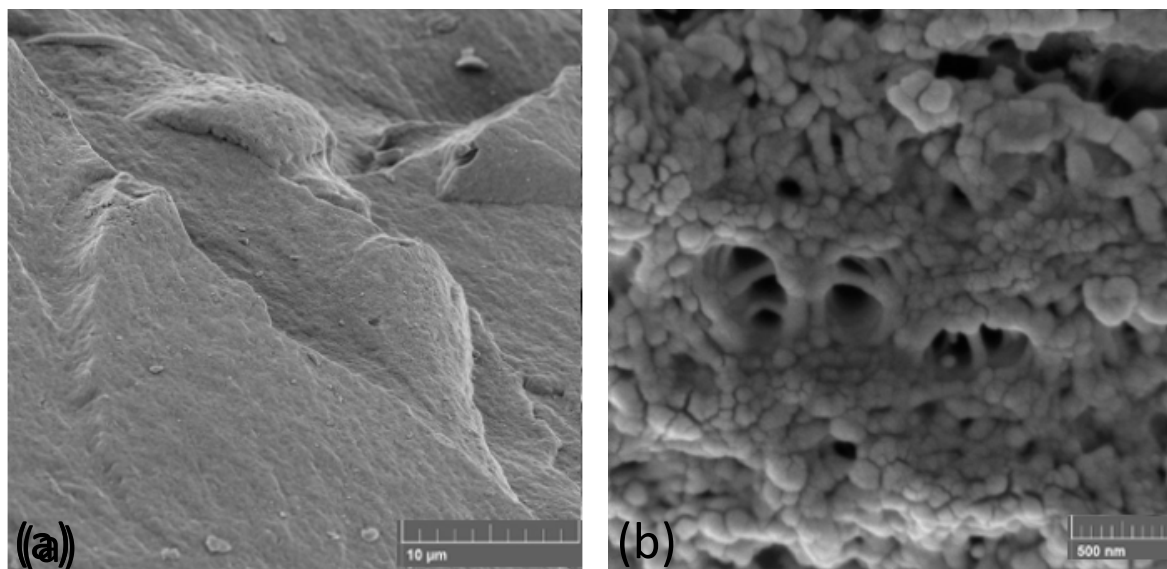
Figure 2.8 SEM images of hybrid TEOSPEG 400MW composites (a) surface of the sample (b) cross section of nanocomposite

2–5.5 Activation Energy of Cation Transport in Materials with Different Polymer MWs Mixtures

We analyzed the data shown in Fig. 2.6 using the VAG model to assess how changes in molecular configuration due to different polymer chain length and mixtures thereof affect thermally activated processes. The intent is to probe the structural origin of the observed behavior, as opposed to the morphological one. The components of the activation free energy are plotted vs. *b* in Fig. 2.9. Accordingly, the activation energy of a given sample roughly doubles upon decreasing the temperature within the measurement range. At a given temperature, the activation energy between the least and most conductive sample changes by approximately 10 kJ/mol. The interesting observation here is that the materials with the highest conductivities also exhibit the highest activation energies, which at first is counter-intuitive, but not unprecedented when the molecular constitution of the material changes significantly between sample types. This reflects marked differences in the energy landscape between materials. The reason why conductivity and activation energy can both be high is that the increased height of the activation barrier is compensated by a simultaneous increase in activation entropy. Accordingly, the material with the deeper potential wells affords

more choices of cation passageways in the vicinity of the saddle points, as is realized by a flattening of the

energy landscape at higher energies.
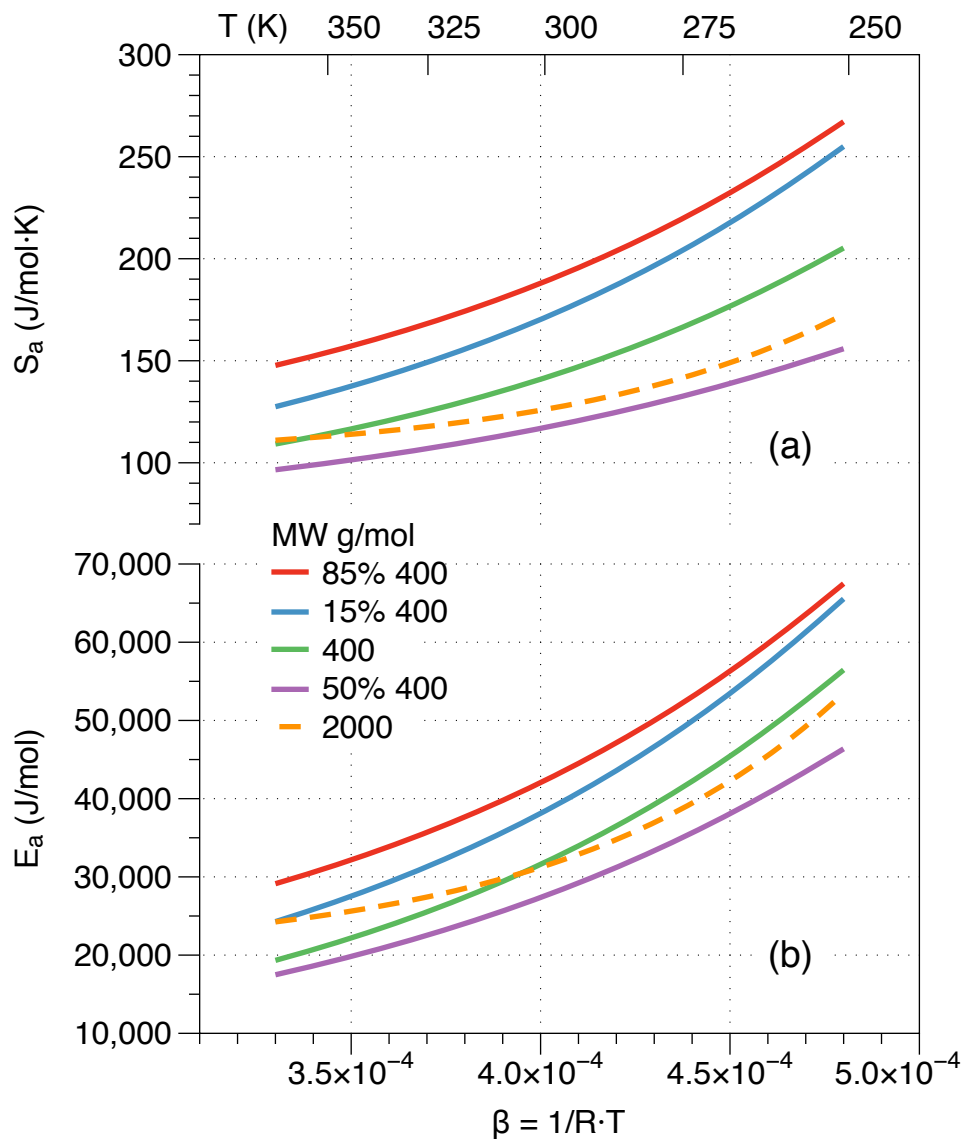
Figure 2.9   Activation entropies (a) and enthalpies (b) as a function of the scaled reciprocal temperature for hybrid silica-PEO materials with various mixtures of two different chain lengths

The sequence of activation enthalpies and entropies is remains in step with the conductivity magnitudes for as

long as the material contains the low-molecular weight polymer. The outlier in this sequence is the material

that contains only large molecular weight polymer. Given the length of this polymer in comparison with

silica backbone pores sizes, it is possible that this polymer alone can achieve the same fill factor as those

containing any amount of short-chain polymer. Voids that the latter could reach remain unfilled when only

longer-chain polymer is used. Thus, we believe that we again witness residual nano-porosity, the reduction of

conduction cross-section, and the formation of low-activation energy surface migration pathways.

2–5.6   X-ray Diffraction

The degree of crystallinity of the hybrid electrolytes is an important parameter that affects the ionic

conductivity of the material. X-ray diffraction measurements of hybrid electrolytes with various polymer

molecular weight and 100 wt.% silica was measured to verify the degree of crystallinity.
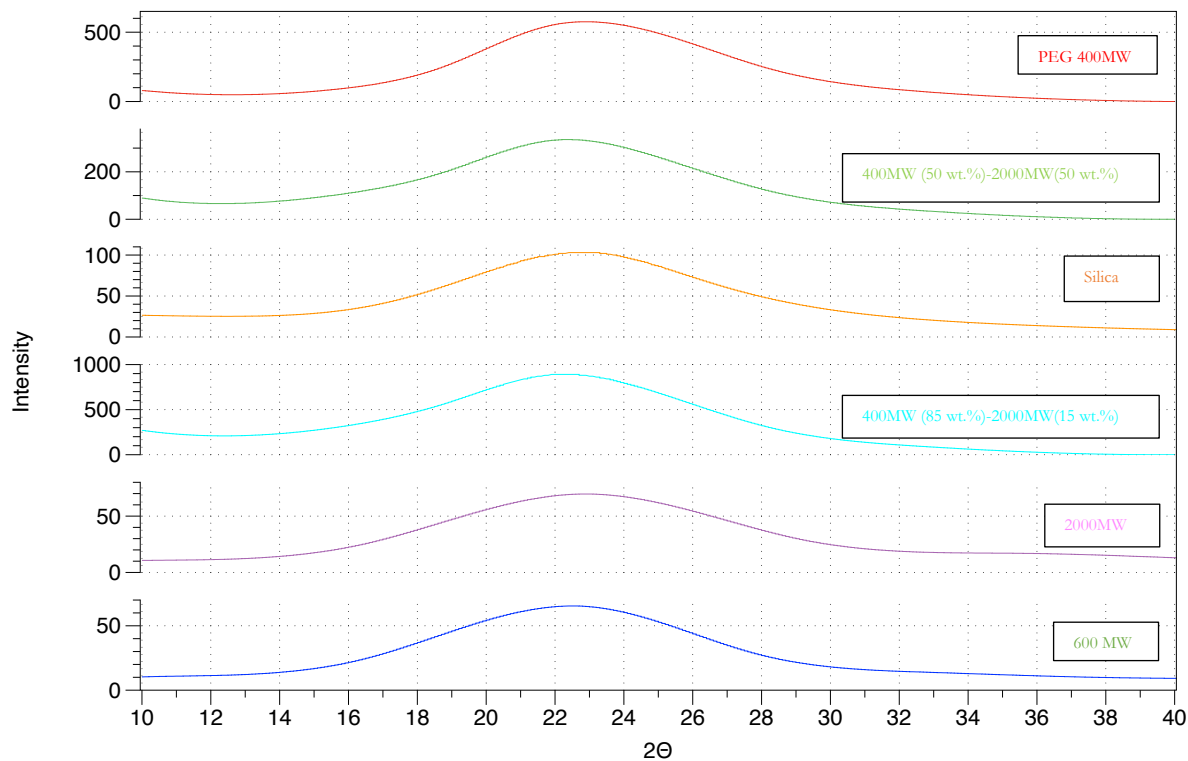
Figure 2.10   XRD patterns of Silica, hybrid PEG-silica samples with Mw 400,6000 and 2000 and mixture of two
different chain lengths. The various samples were scanned at 5° 2θ min^{-1}.

As shown in Fig 2.10, all samples had a broad peak around 22°-24° which is characteristic of an amorphous

material. The XRD patterns also confirm that the lithium source is fully dissociated in system. The sharp

peaks of LiClO$_4$ at 13 °, 21° 23°, 24.5° and 32°are not present in the XRD patterns of the hybrid electrolytes.

CHAPTER 3   Drying Induced Structural Inhomogeneities

3–1   Introduction

In this study, we develop a hybrid solid electrolyte via a two-step process. In the first step, the inorganic backbone is synthesized using acid catalyzed sol-gel polymerization of TEOS. In the second step, we introduce the organic phase in the second step via solution exchange. As shown in the previous chapter, efforts to graft the polymer to the backbone in order to immobilize the conducting phase and reduce osmotic drag were met with challenges. Even without including reactive groups in the silica backbone and polymer, in many cases measured materials properties were afflicted with significant variability, despite great precautions with regard to compositional consistency. We therefore shifted our focus on investigating the influence of post synthesis processes on the structural evolution. The post synthesis materials development involves casting the obtained gel in Teflon rings and controlled drying. We changed the casting mold diameter from 36 to 18 mm, but maintained the same thickness. Since the aspect ratios of the cast geometries are different, we expect to gain some insight into the constitution of the material solely conditioned by geometry. The comparison of the ionic conductivities of samples that are chemically identical but cast differently confirm that post synthesis processes have resulted in inhomogeneity of ionic conductivity.

3–2   Sample Preparation

- *Materials*

The materials used for this study are all reagent grade and can be purchased commercially. These include tetraethylorthosilicate (TEOS, > 98%), Poly-(ethylene glycol) [PEG 400, 600, 1000, 2000, 6000 and 10000 g·mol^{-1}], hydrochloric acid (HCl) were purchased from Sigma-Aldrich. Lithium Perchlorate (battery grade, dry, 99.99% trace metals basis) was kept under vacuum at 50 °C and purchased from Sigma-Aldrich. Ethanol (200% proof) was purchased from Fischer Scientific.

- *Synthesis of TEOS*

Step-1: Backbone Formation

The synthesis of the inorganic backbone is carried out using a modified version of the method described in the literature.[72] We mix TEOS (13.8 g, 0.0663 mol), ethanol (12.9 g, 0.28 mol), water (2.19 g, 0.28 mol) by rapidly stirring for 30 minutes. Then, HCl (1M, 0.0007 mol, 0.71 g) is added dropwise and the solution is stirred for 48 hours at 60 °C. As soon as the gelation process initiates, as judged by the observed changes in flow behavior upon lightly jiggling the beaker, the solution is cast in 18 or 36 mm O-rings. The hydrogels so obtained are immersed in ethanol and aged for three days in a sealed container then washed with ethanol to remove unreacted TEOS. A monolithic hydrogel with a silica backbone that it connected and percolates in three dimension ensues.

Step-2: **Infuse Network with Conducting Polymer phase**

To infiltrate the pores of the hydrogel samples obtained in the previous step with polymer, different solutions of poly (ethylene oxide) (400 MW, 600 MW and 1000 MW) are prepared using ethanol as solvent. The polymer phase is incorporated into the porous inorganic backbone obtained from the step-1 via solution exchange. The gels synthesized from step-1 are submerged in polymer solutions for 6 hrs at room temperature then 12 hrs at 55 °C.

- *Sample Drying*

The obtained gels are sealed in a petri dish and dried for 72 hours in ambient conditions. Then, the samples are moved to heated oven and kept for 24 hours at 40 °C. The drying step has been repeated for two more rounds with the same number of hours while changing the temperature to 50 and 60 °C consecutively.

To determine the drying rates for samples, the synthesized xerogels with and without polymer were imaged using a Nikon DSLR camera. ImageJ software is used to convert the obtained pixels to area. As we can see in

Figure 3.1, xerogels without polymer shrink faster and the ratio of final diameter to initial diameter of xerogels without polymer is smaller compared to the xerogels with polymer.
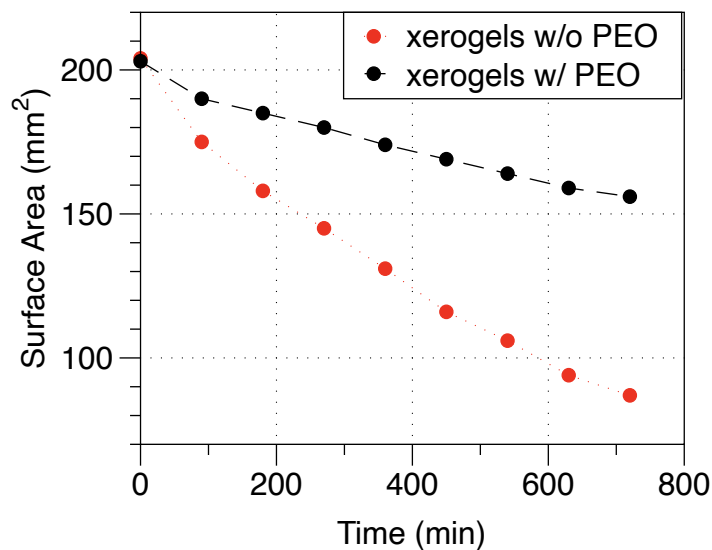
Figure 3.1   Graph of the surface area (mm^2) of xerogels w/ and w/o polymer versus time (min)

- *Materials Characterization.*

Thermogravimetric analysis (TGA) of the final dry electrolyte samples is done using a TA instruments Q500 TGA analyzer under nitrogen atmosphere to prevent the oxidation of the samples. The prepared samples are dried under vacuum at 55 °C. To measure temperature dependent ionic conductivity of the prepared xerogels, electrochemical impedance (EIS) was used using a Novocontrol broadband dielectric impedance spectrometer. The EIS measurements were conducted from -12.5 °C to 62.5 °C and 0.1 Hz to 10 MHz.

3–3   Results and Discussion

In this part of the work, we study the effects of processing conditions, specifically the radial shrinkage of the prepared materials, on chemical composition and elastic modulus of hybrid organic-inorganic electrolytes. As detailed earlier, the rate limiting step in sample preparation is the drying period. The drying rate must be kept low in order to prevent sample cracking. Mainly for this reason, we explored reducing the sample size, expecting that this would also reduce the time necessary to evacuate the solvents from the pores. Indeed, we

found that by simply cutting the sample diameter in half, the drying period was significantly shortened, despite keeping the same sample thickness.

3–3.1   Ionic Conductivity as a Function of Sample Size

Recall, that during drying the samples shrink only in radial direction and not in thickness. Furthermore, the ratio of sample diameter before (d_i) and after drying (d_f) is independent of the casting diameter, i.e.,

$$\frac{d_f}{d_i} = 0.62 \,.$$
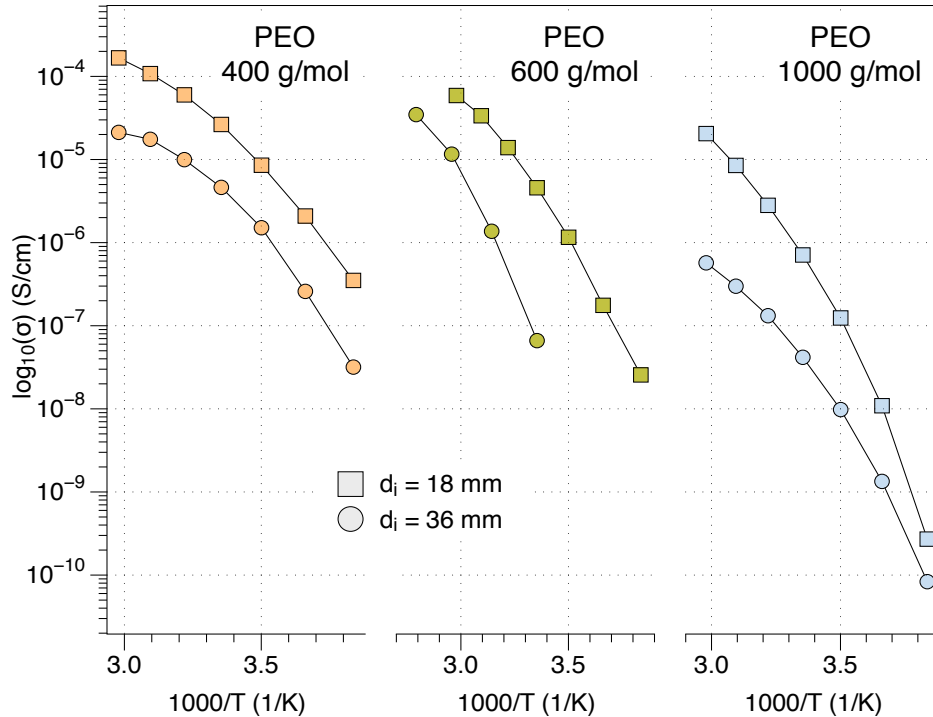
Figure 3.2   Ionic conductivity as a function of the reciprocal temperature for samples with three different polymer lengths, comparing two different casting diameters for each set.

This confirms that the total shrinkage is the same for large and small sample, i.e., the same amount of solvent is evacuated per unit volume of material, regardless of its size. It has therefore been surprising to find that the measured conductivities has been significantly and consistently higher for the smaller samples than for the

larger ones. This is reflected by the data shown in Fig. 3.2, where we plot the ionic conductivity vs. reciprocal temperature for samples with three different polymer chain lengths and two casting radii for each chemical composition.

Surprisingly, the conductivities and their temperature dependence vary strongly solely based on casting diameter. It is intriguing that this property can vary by an order of magnitude or more, without changing the nominal chemical constitution of the material. Currently, in this field of research, the principal variable that is being explored for improving conductivity is the material's chemistry. It is therefore important to determine to what extent materials conditioning can achieve the same.

3–3.2   Ionic Conductivity as a Function of the Location in the Sample

During drying of the samples, the material undergoes local structural changes that include the mere removal of solvent, leaving behind salt-doped polymer and the silica backbone. It is likely that the resulting structure contains nano-scale porosity in places where the silica backbone cannot sufficiently contract to close all voids between backbone and polymer. Furthermore, the contraction of the network can lead to further polycondensation of residual OH groups, and thus increased rigidity of the backbone. Considering the large aspect ratio of diameter to thickness, and the fact that shrinking only occurs in radial direction, it is safe to assume that the vast majority of fluid evaporates through the top face of the disk, except for the outside perimeter. Hence, the compaction and rigidification of the material may indeed start on the edge of disk and progress inward with time, leading to spatially inhomogeneous mechanical and transport properties. Depending on the radial distribution describing these properties, it may explain why smaller samples conduct better than larger ones.

To test this hypothesis, we measured the ionic conductivity of samples while progressively removing material at the circumference. That is, we first measured the conductivity of the as-cast sample, then cleaved away four segments from the periphery to yield a square, and if possible cleaved away the corners of the square to yield an even smaller square. After each cleaving, the measured conductivity is dominated more and more by

the mobility at the center of the sample. Measurements were carried out as a function of temperature, so that we can also analyze the nature of the thermal activation of the transport process.
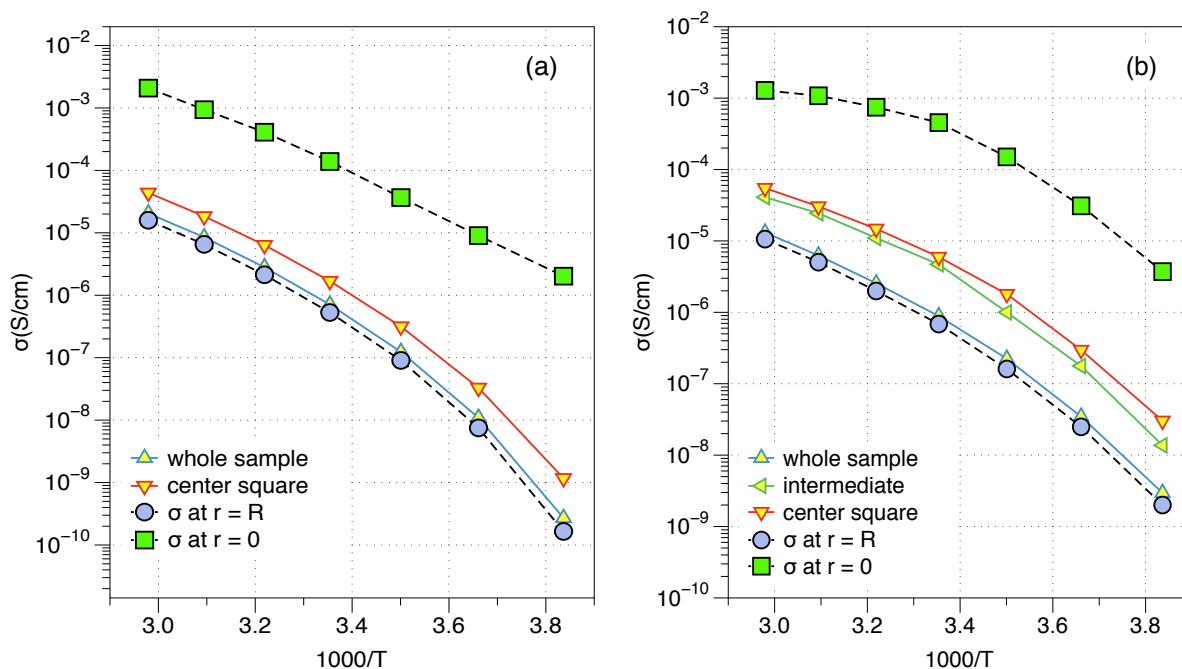
Figure 3.3   Ionic conductivities of silica-PEO hybrid electrolytes as a function of the reciprocal temperature: (a) for a system containing 1000MW PEO (EO/Li=10) (b) for a system containing 400MW PEO (EO/Li=10)

Indeed, using this approach, we consistently found that the center portions of our samples exhibit clearly higher ionic conductivities than the as cast samples. Two representative sets results of our analysis are shown in Fig. 3.3 (a) and (b). The measured data are shown as open triangular symbols. In Fig. 3.3 (a), for a system containing PEO with an average molecular weight of 1000 g/mol and a salt loading of EO/Li = 10, two sets of measured data can be seen, corresponding to the whole sample (lower values) and to a center square segment obtained after a first cleaving (higher values). Similarly, In Fig. 3.3 (b), for a system containing PEO with an average molecular weight of 400 g/mol and a salt loading of EO/Li = 30, three sets of measured data can be seen, corresponding to the whole sample (lowest values) and two center squares obtained after cleaving twice consecutively (higher values). Accordingly, it is clear that the material in the core of the samples exhibit significantly higher ionic conductivity, increasing progressively the closer one gets to the center. In the case of the lower-molecular weight system, based on the measurements alone, we observe an

order of magnitude increase at room temperature. Each of the plots contains two additional sets of data, to a description of which we will return below.

To further pursue our hypothesis that inhomogeneities develop in the samples during drying, we probe for manifestations of such nonuniformities at various levels. First, we verify whether the chemical composition of the material is affected by the processing conditions, i.e., whether the proportions of silica backbone and polymer filler might be different in the center vs. the perimeter of the samples. To this end, we performed TGA by separately collecting material from the center and the periphery of the dried electrolytes. The TGA data so obtained, shown in Fig. 2-3, overlap within experimental error, confirming that the content of organic constituents in material is invariant as a function of the radius of the samples.
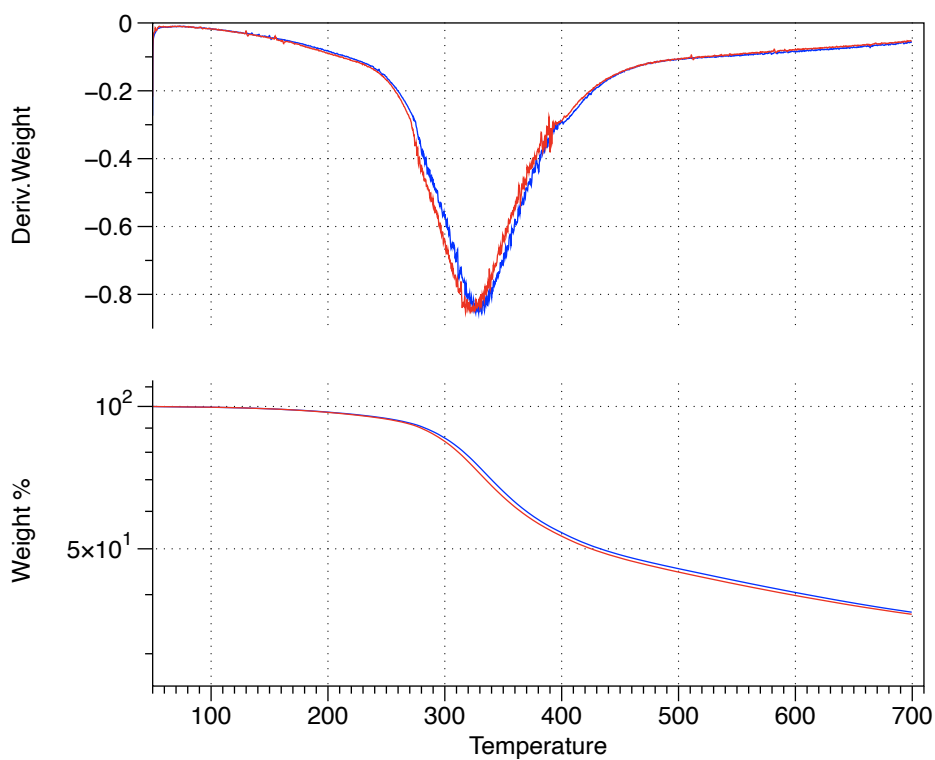
Figure 3.4 TGA of the center and periphery of hybrid electrolyte for verification of chemical homogeneity of the sample

Next, we examine the chemical constitution of each of the composite material's components using FTIR spectroscopy. Again, material collected from the center and the periphery of the sample are measured

separately and spectra are compared in Figure 3.4. While some differences between the spectra of neat PEO and PEO embedded in silica pore structures are apparent, revealing the effects of the nano-confinement, the important finding is that the transmittance peaks for the composite in the center and at the periphery completely overlap, proving that the center and the periphery of the material are chemically identical, and thus, the specimens are chemically homogenous as a function of their radii.
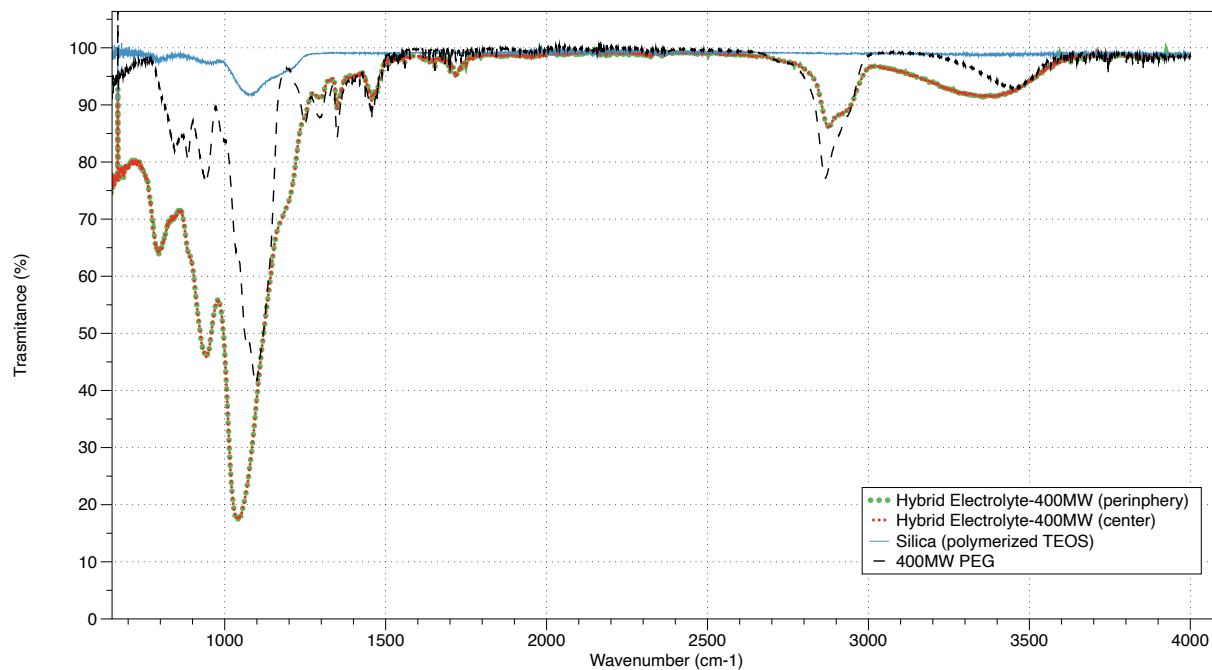
Figure 3.5   FTIR of the center and periphery of hybrid electrolyte shown in green and red, silica backbone shown in blue and 400MW PEG shown in black.

3–3.3   Ionic Conductivity and Elastic Properties

Finally, using BLS to probe the adiabatic elastic modulus of the material as a function of the position along the diameter of the sample, inhomogeneities become apparent. Measurements were taken in platelet and platelet-complement scattering geometries, as outlined in Chapter 1, which allows one to determine the elastic response to in-plane (radial) and out-of-plane (axial) deformations, respectively. Fig. 3-6 shows the in-plane and out-of-plane longitudinal adiabatic moduli for hybrid electrolytes containing PEO with different chain lengths. Accordingly, the in-plane modulus increases with chain length, whereas the out-of-plane modulus

decreases. Generally, the smaller-chain length polymer is able to penetrate pores more uniformly than the larger-chain length ones. This appears to work in favor of the axial modulus, but not so for the radial modulus. Also, the out-of-plane modulus is significantly higher than the in-plane modulus, especially at the lower molecular weight of the polymer, where the two quantities differ by essentially a factor of two. This divergence can be understood as indicative of a texture that develops in the silica backbone upon drying, i.e., pores collapse in the in-plane direction and, consequently become elongated in the out-of-plane direction. As a result, the backbone has a higher load bearing capability in axial direction than in the radial direction. This anisotropy is advantageous for device performance. The large axial modulus serves to enhance the structural stability of a battery, while the lower radial modulus facilitates cation migration, as detailed below.
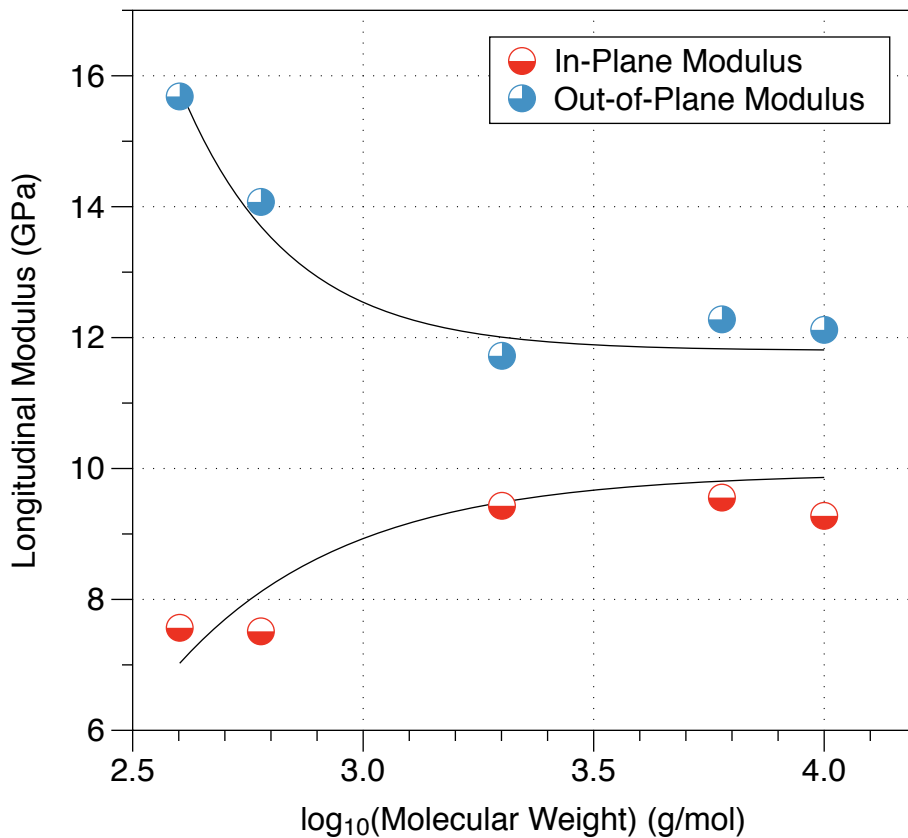
Figure 3.6 In-plane and out-of-plane longitudinal adiabatic moduli for hybrid electrolytes containing PEO with different chain lengths. Lines are provided to guide the eye.
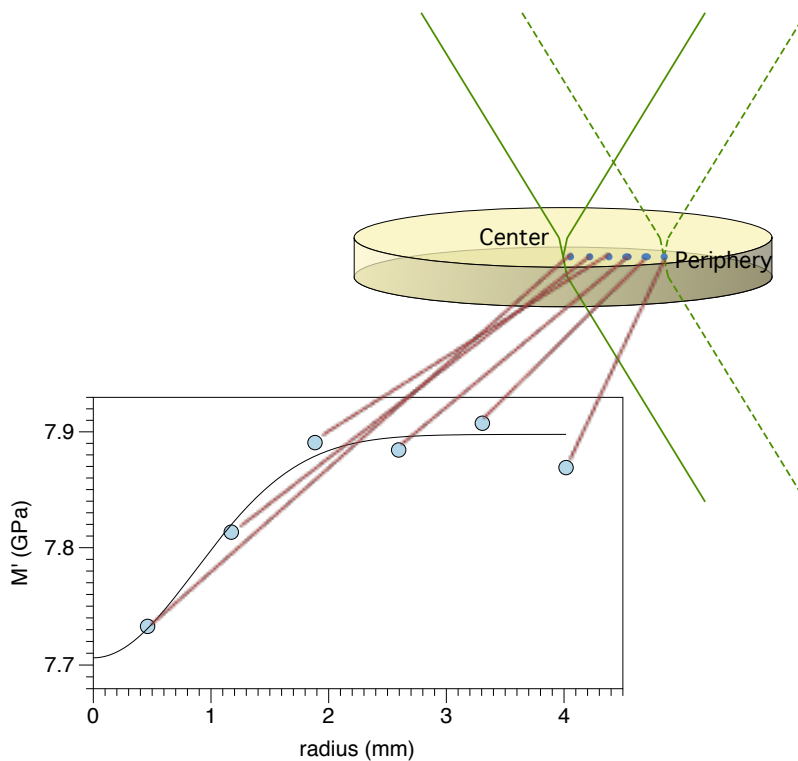
Figure 3.7   Radial dependence of the in-plane longitudinal adiabatic elastic modulus

The structural evolution that results from the radial shrinkage of xerogels during the drying processes could explain the inhomogeneity of the elastic modulus of the material, specifically more pronounced difference in the center of material compared to the periphery.

From the obtained data shown in Fig. 3.7, we can conclude that the adiabatic modulus decreases as the position is moved from the periphery to center. In Fig. 3.7 we show the in-plane longitudinal adiabatic elastic modulus as a function of the radius of the sample. The magnitude dips by about 3% near the center. By comparison, the out-of-plane modulus remains constant with experimental scatter similar to that of the in-plane modulus at larger radii. This finding is significant in two respects. First, it evidences inhomogeneity in the mechanical properties, and second, the decrease of the adiabatic modulus towards the center is consistent with observing higher cation mobility. This latter conclusion is based on a discovery we made recently, which is that for a monolithic amorphous material, the adiabatic modulus is strongly correlated with the negative

logarithm of the ionic conductivity multiplied with temperature.[52] To illustrate this connection, consider that in a first approximation we can describe the ionic conductivity using the Arrhenius relationship,

$$-\ln\left(\sigma\cdot T\right) = -\ln\sigma_0 + E_a\big/k_B T \tag{3.1}$$

where dependence temperature is entirely attributed to the activation energy for cation hopping, E_a. Correlating the left hand side of this equation with the adiabatic modulus M, involves a scaling (factor p) and a shift (factor q), i.e.,

$$-\ln\left(\sigma\cdot T\right) = q + pM \tag{3.2}$$

Comparing Eq. (3.1) and (3.2) yields $pM = E_a\big/k_B T \quad q = -\ln\sigma_0$. Accordingly, at any given temperature, the activation energy for cation hopping, which is an energy per atom is directly proportional to the adiabatic elastic modulus, which is an energy per volume. In other words, a lower elastic modulus provides for higher atomic mobility, and *vice versa*.

3–3.4   Calculated Extremes in Ionic Conductivity

In our hybrid materials, for which we attribute the cation conduction process predomintly to the polymer phase, the above relationship contains an additional unknown scaling parameter, depending on what rule of mixture applies. That is, the measured modulus reflects a composite quantity and not directly the magnitude of the modulus of the polymer phase. However, since we have shown that the chemical composition of our material is independent of the position along the radius of the sample, we can use the functional form that describes the radial dependence of the overall modulus as reflective of the radial dependence of the polymer contribution to stiffness. As shown in Fig. 3.7, the radial dependence elastic modulus, and thus, of the negative logarithm of the ionic conductivity is well described by a Gaussian function. Hence, defining $\kappa\left(r\right) = -\ln\left(\sigma\left(r\right)\cdot T\right)$, we can write

$$\kappa(r) = (\kappa_0 - \kappa_R) e^{-ar^2} + \kappa_R, \tag{3.3}$$

where the quantities $\kappa_0 = \kappa(r = 0)$ and $\kappa_R = \kappa(r = R)$ are unknown. The parameter a, resulting from fitting the modulus data using the Gaussian function, is the only fixed parameter for the analysis that follows. Typically, when we measure conductiviy, we implicitely assume a constant value anywhere in the sample, and the evaluation of the desired quantity is straightforward. However, in case the conductivity has a radial dependence, we effectively measure an average conductivity across the surface in contact with the electrodes. Formally it requires multiplication of the local quantity $\kappa(r)$ with the differential contact surface area $rd\phi dr$, integration over the entire contact area, and normalization with respec to that area. For the conductivity of the as-cast intact sample, this amounts to

$$\begin{aligned}
\kappa_t &= \frac{1}{\pi R^2} \int_0^R \int_0^{2\pi} \kappa(r) r\, d\phi\, dr \\
&= \frac{(\kappa_0 - \kappa_R)}{\pi R^2} \int_0^R \int_0^{2\pi} r e^{-ar^2}\, d\phi\, dr + \frac{\kappa_R}{\pi R^2} \int_0^R \int_0^{2\pi} r\, d\phi\, dr \\
&= \frac{2(\kappa_0 - \kappa_R)}{R^2} \int_0^R r e^{-ar^2}\, dr + \kappa_R,
\end{aligned}$$

or

$$\kappa_t = \kappa_0 \left[\frac{2}{R^2} \int_0^R r e^{-ar^2}\, dr \right] + \kappa_R \left[1 - \frac{2}{R^2} \int_0^R r e^{-ar^2}\, dr \right]. \tag{3.4}$$

Hence, the coefficients multiplying κ_0 and κ_R in this linear equation are the integral (and its complement) in the square brackets. Since $\dfrac{de^{-ar^2}}{dr} = -2are^{-ar^2} \Rightarrow re^{-ar^2} = -\dfrac{1}{2a}\dfrac{de^{-ar^2}}{dr}$ and

$$\frac{2}{R^2} \int_0^R r e^{-ar^2}\, dr = -\frac{1}{aR^2} \int_0^R de^{-ar^2} = \frac{1}{aR^2}\left(1 - e^{-aR^2}\right). \text{ Hence, } \kappa_t = \kappa_0 \frac{\left(1 - e^{-aR^2}\right)}{aR^2} + \kappa_R \left(1 - \frac{\left(1 - e^{-aR^2}\right)}{aR^2}\right)$$

Note that aR^2 is dimensionless. Abbreviating $I_t = \left(1 - e^{-aR^2}\right)\Big/\left(aR^2\right)$, we obtain the equation

$$\kappa_t = \kappa_0 I_t + \kappa_R \left(1 - I_t\right) \qquad (3.5)$$

Conversely, when the sample after cleaving consists of a centered rectangular fragment, the integration no longer encompasses the entire surface of the circular disc, but is truncated as delineated by the edge of the rectangle. In a first approach, we use the function $\delta(r,\phi) = \begin{cases} 1 \text{ if } \left(r\cos(\phi) \leq x_m \text{ and } r\sin(\phi) \leq y_m\right) \\ 0 \text{ otherwise} \end{cases}$ to account for this truncation. The integral can then be written as

$$\begin{aligned}
\kappa_x &= \frac{1}{\left(x_m y_m\right)} \int_0^R \int_0^{\pi/2} \kappa(r)\delta(r,\phi)\, r\, d\phi\, dr \\
&= \frac{\left(\kappa_0 - \kappa_R\right)}{\left(x_m y_m\right)} \int_0^R \int_0^{\pi/2} re^{-ar^2}\delta(r,\phi)\, d\phi\, dr + \frac{\kappa_R}{\left(x_m y_m\right)} \int_0^R \int_0^{\pi/2} r\delta(r,\phi)\, d\phi\, dr \\
&= \frac{\left(\kappa_0 - \kappa_R\right)}{\left(x_m y_m\right)} \int_0^{\pi/2} \int_0^R re^{-ar^2}\delta(r,\phi)\, dr\, d\phi + \kappa_R
\end{aligned}$$

We note that, even when allowing for x_m and y_m to be different, as long as the center of the rectangle coincides with that of the circle, symmetry requires integration over only one quadrant (and multiply by four) to obtain the desired quantity. This means that the angle ϕ only varies between 0 and $\pi/2$.

Defining $I_x = \frac{1}{\left(x_m y_m\right)} \int_0^{\pi/2} \int_0^R re^{-ar^2}\delta(r,\phi)\, dr\, d\phi$, which is evaluated numerically, we get

$$\kappa_x = \kappa_0 I_x + \kappa_R \left(1 - I_x\right) \qquad (3.6)$$

Alternatively, we can express the condition for $\delta(r,\phi)$ to be finite as an upper-bound radial limit that depends on ϕ as follows. If we divide this range into two segments, 0 to ϕ_C, and ϕ_C to $\pi/2$, where ,

54

$$\phi_C = \tan^{-1}\left(y_m/x_m\right) \text{, i.e.,}$$

$$\kappa_x = \frac{\left(\kappa_0 - \kappa_R\right)}{\left(x_m y_m\right)}\left[\int_0^{\phi_C}\int_0^{r_\phi} re^{-ar^2}\,dr\,d\phi + \int_{\phi_C}^{\pi/2}\int_0^{r_C} re^{-ar^2}\,dr\,d\phi\right] + \kappa_R,$$

where for $0 \le \phi \le \phi_C, r_\phi = x_m/\cos\phi$ and $\phi_C \le \phi \le \pi/2, r_\phi = y_m/\sin\phi$. Abbreviating

$$I_b = \frac{1}{\left(x_m y_m\right)}\left[\int_0^{\phi_C}\int_0^{r_\phi} re^{-ar^2}\,dr\,d\phi + \int_{\phi_C}^{\pi/2}\int_0^{r_\phi} re^{-ar^2}\,dr\,d\phi\right].$$

Finally, substituting $\int_0^{r_\phi} re^{-ar^2}\,dr = -\frac{1}{2a}\int_0^{r_\phi} de^{-ar^2} = \frac{1}{2a}\left(1 - e^{-ar_\phi^2}\right)$ yields

$$I_b = \frac{1}{2a\left(x_m y_m\right)}\left[\int_0^{\phi_C}\left(1 - e^{-a\left(x_m/\cos\phi\right)^2}\right)d\phi + \int_{\phi_C}^{\pi/2}\left(1 - e^{-a\left(y_m/\sin\phi\right)^2}\right)d\phi\right].$$

which is again evaluated via numerical integration. Hence,

$$\kappa_x = \kappa_0 I_b + \kappa_R\left(1 - I_b\right) \qquad (3.6\text{'})$$

Provided a sufficiently small angular or linear coordinate discretization, the two numerical integrals I_x and I_b are identical. Rewriting Eq. (3.5) and (3.6) as a system of two equations in matrix form,

$$\begin{pmatrix} I_t & 1-I_t \\ I_x & 1-I_x \end{pmatrix}\begin{pmatrix} \kappa_0 \\ \kappa_R \end{pmatrix} = \begin{pmatrix} \kappa_t \\ \kappa_x \end{pmatrix}, \qquad\qquad (3.7)$$

which can be solved using methods such as Gaussian elimination. Recall that κ_0 and κ_R are the unknowns. The elements of the coefficient matrix are evaluated using the above integrals; they are only dependent on the geometry of the specimens, and κ_t and κ_x are obtained via measurement. In case we have more

measurements than unknowns (i.e., two or more cleaves instead of one), the system of equations takes the form

$$
\begin{pmatrix}
I_t & 1-I_t \\
I_1 & 1-I_1 \\
\vdots & \vdots \\
I_n & 1-I_n
\end{pmatrix}
\begin{pmatrix}
\kappa_0 \\
\kappa_R
\end{pmatrix}
=
\begin{pmatrix}
\kappa_t \\
\kappa_1 \\
\vdots \\
\kappa_n
\end{pmatrix},
\tag{3.7'}
$$

which is solved using linear regression. Either way, as the outcome we obtain the $\ln(\sigma T)$ values at the locations corresponding to the edge and the very center of the samples, for every measurement temperature. These values are converted to conductivities and plotted as filled circles and squares, respectively, along with the measured data in Fig. 3.3 (a) and (b). Based on measurement alone, we already observe an increase in conductivity by one order of magnitude between the whole sample and the center square at ambient conditions. The calculations suggest that the local conductivity in the very center of the sample can be up to three orders of magnitude higher than the measure value for the whole sample. This assessment is derived from measured quantities and only depends on the shape of the distribution function. The narrower this distribution function (i.e., the smaller its full width at half maximum), the stronger the magnification of the cation mobility in the center of the sample.

3–3.5   Drying dynamics and densification

Importantly, the enhancement of the ionic conductivity that we observe (or calculate) is purely based on structural conditioning during materials processing, without changing the chemistry of the material. Accordingly, it may not always be necessary to change the chemical composition in order to improve electrolyte performance. Evidently, to harness the characteristics of the central portion we must fully understand its structural origin and devise a method to impart the structural features more widely across the entire expanse of the material. As to the former, we have a working hypothesis. To illustrate this concept, we devised a simplified model describing the drying and shrinkage process. As mentioned earlier, except for the outer edge, the solvent emanates from the sample through the top surface. For the argument's sake we

consider that the sample consists of a liquid and a solid phase, the former being the solvent that is removed, and the latter being the mixture of silica, polymer, and salt. As the solvent evaporates, the sample shrinks, and since its center of mass remains stationary, the outer edges of the specimen approach the center at a faster rate than sections closer in. This is illustrated in the adjacent graphic (Fig. 3.8)
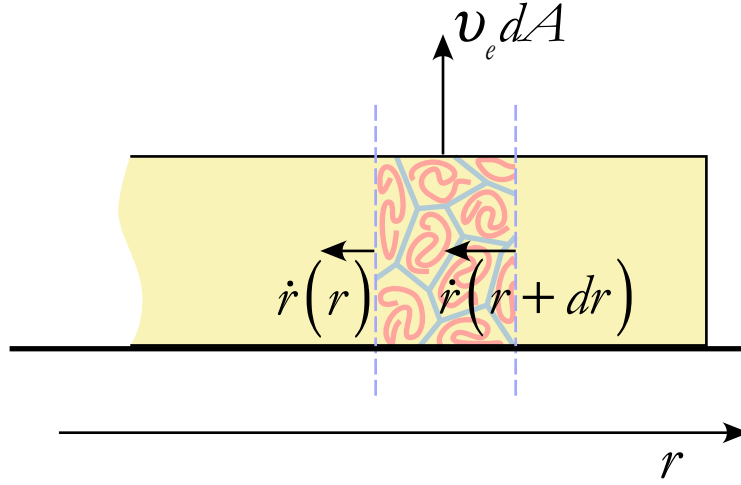
Figure 3.8   Schematic of the differential balance describing the removal of solvent from the porous hybrid network.

Since the drying takes place very slowly (over days), we ignore the acceleration of matter and even frictional forces, limiting it mostly to a mass balance. We consider the rate limiting step to be the evaporation of solvent at this surface. Hence, during the initial stages of the drying process, when pores contract freely, the differential volume of solvent evacuated per unit time from the sample at a distance r from its center is

$$d\left(\frac{dV}{dt}\right) = 2\pi r h \frac{d\dot{r}}{dr} dr = -v_e dA = -v_e 2\pi r dr \; , \tag{3.8}$$

where v_e is the effusion velocity, h is the thickness of the sample, and dA is the differential cross-sectional area. The effusion velocity describes the volume of solvent emanating per unit surface area (i.e., a linear velocity), while considering the volume of solvent in the liquid state. Simplifying,

$$\frac{d\dot{r}}{dr} = -\upsilon_e / h \Leftrightarrow d\dot{r} = -\upsilon_e / h \, dr \, ,$$

and integration yields

$$\dot{r}(r) = -(\upsilon_e / h) r \, ,\hspace{4cm}(3.9)$$

with the boundary condition being that $\dot{r}(r = 0) = 0$. This shows that the sample indeed contracts more rapidly at the periphery than in the center. However, as drying progresses, the contraction is gradually impeded by elastic forces resulting from the impingement of solid structural elements upon one another. Eventually, no further compaction can be achieved. To account for this circumstance, we included a factor $f(\Delta \dot{r})$ in Eq. (3.9) that cause the shrinkage rate to vanish when the degree of schrinkage reaches its maximum

$$\Delta r(r,t) = -(\upsilon_e f(\Delta r) / h) r \cdot t \, ,\hspace{3cm}(3.10)$$

Where $f(r) = \max(0, 1 - \Delta r_{max} / \Delta r)$. Fig. 3.9 shows the results of solving Eq. (3.10) as a function of the normalized radius, for different drying times. The times listed in the legend are based on fitting the simulated data of the sample's top surface area to the measured data shown in Fig. 3.1. This yields a value for the effusion coefficient (υ_e / h) = $1.8 \cdot 10^{-4}$ per min. The model we applied here is crude in that it does not account for the mechanical intricacies of an elastic modulus that increases with diminishing porosity, nor the structural relaxation within the not yet maximally densified region due to the building tensile stress. The important result for understanding the observed inhomogenities in ionic conductivity, is that maximum densification is first reached at the periphery of the sample. This causes a outer ring of elastically stiff material to form, while the material towards the center of the sample remains malleable due to the remaining higher solvent concentration. Once the periphery has rigidified, it prevents the center from shrinking freely as more solvent is removed from that region. As a result, a state of tensile stress develops near the center preventing the pores in the backbone from collapsing and causing the polymer to configure differently inside the network pores compared to the periphery. (A similar phenomenon is well known in the glass community as thermal

tempering, which creates glass with higher fracture toughness because the surface of the glass is subject to compressive stresses that prevent crack nucleation.)
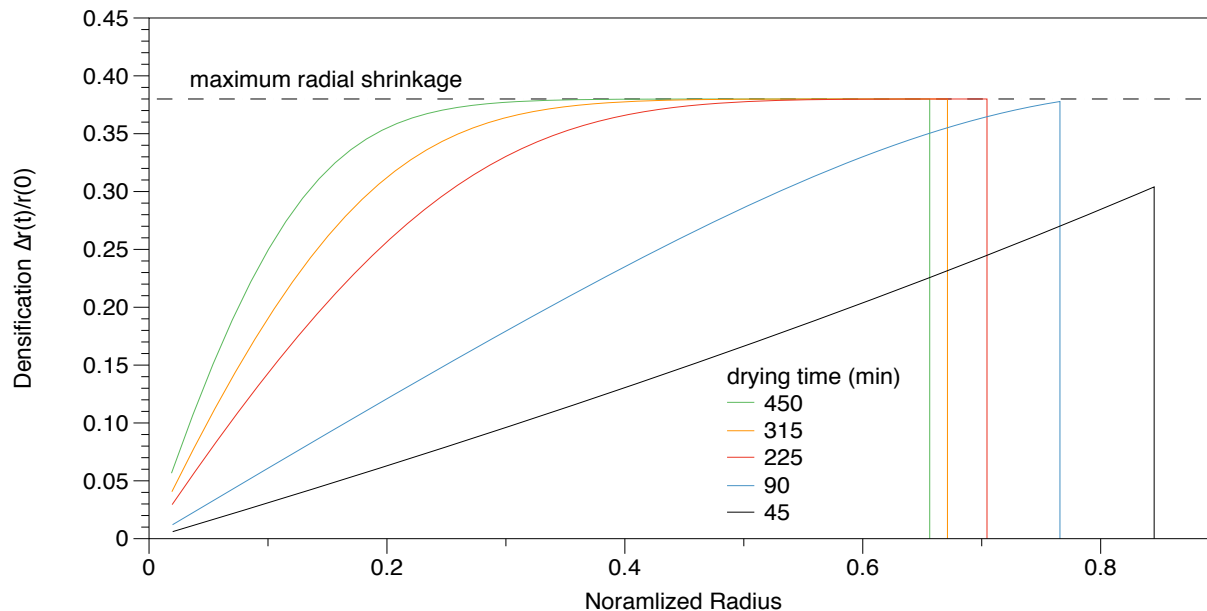
Figure 3.9   Degree of densification as a function or the sample radius calculated using a simplified model to simulate the drying process.

This above analysis suggests that tensile stresses, perhaps lower local density, and the associated structural reconfiguration in the material that is subject to these conditions, is enhances cation mobility. Keep in mind that the material in the center of the sample remains compliant for a longer period of time, allowing for the tensile stresses to relax out. Hence, the observed phenomenon is likely not the result of simply introducing residual stresses in the structure, but that of more complex structural adjustments involving the interplay between silica backbone and polymer filler.

3–3.6   Thermal activation of the cation hopping process

To further explore the nature of the inhomogeneities in the properties of our hybrid electrolytes, we investigate the extent to which these affect thermal activation character of the cation hopping process using the analysis of the temperature dependent coanductivities outlined in the previous chapter.
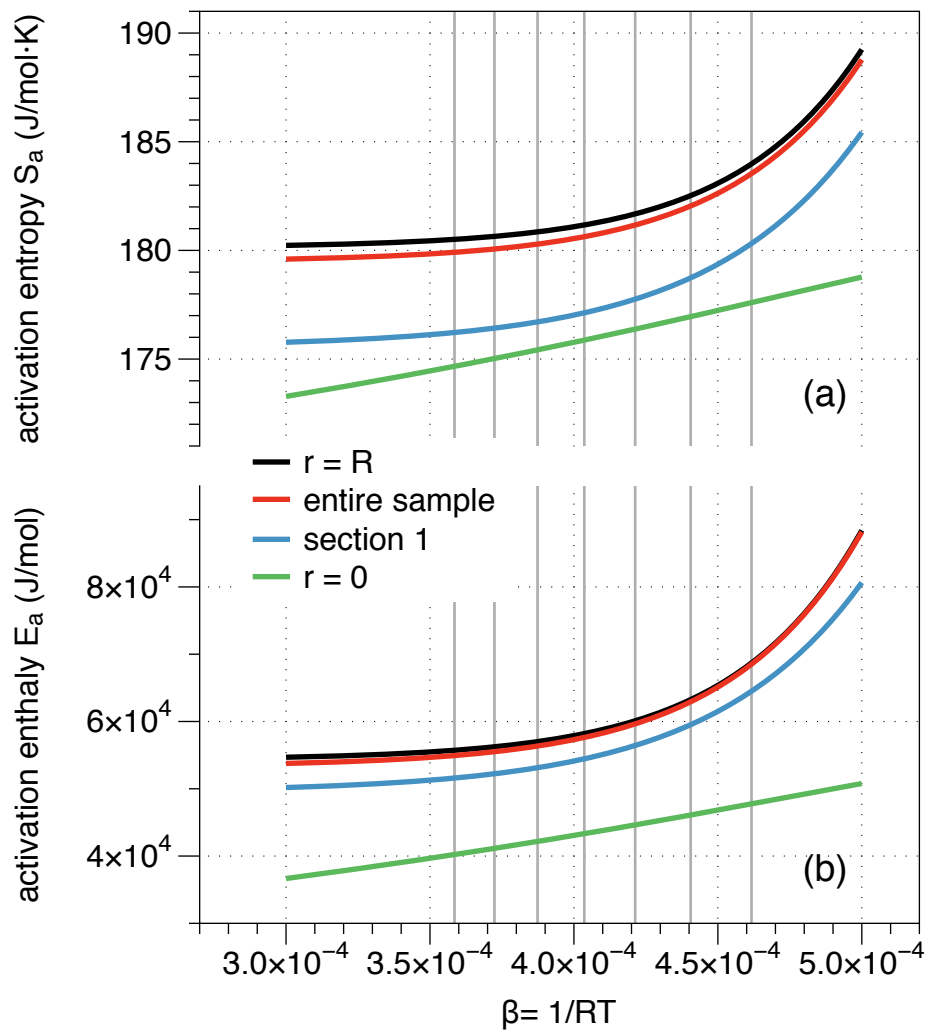
Figure 3.10   (a) Entropy and (b) enthalpy of activation as a function of b for a hybrid electrolyte containing PEO with a molecular weigh of 1000 g/mol. The analysis is carried out for measured data of the entire sample and one cleaved central square, as well as for the calculated data at the outer perimeter and the center of the sample.
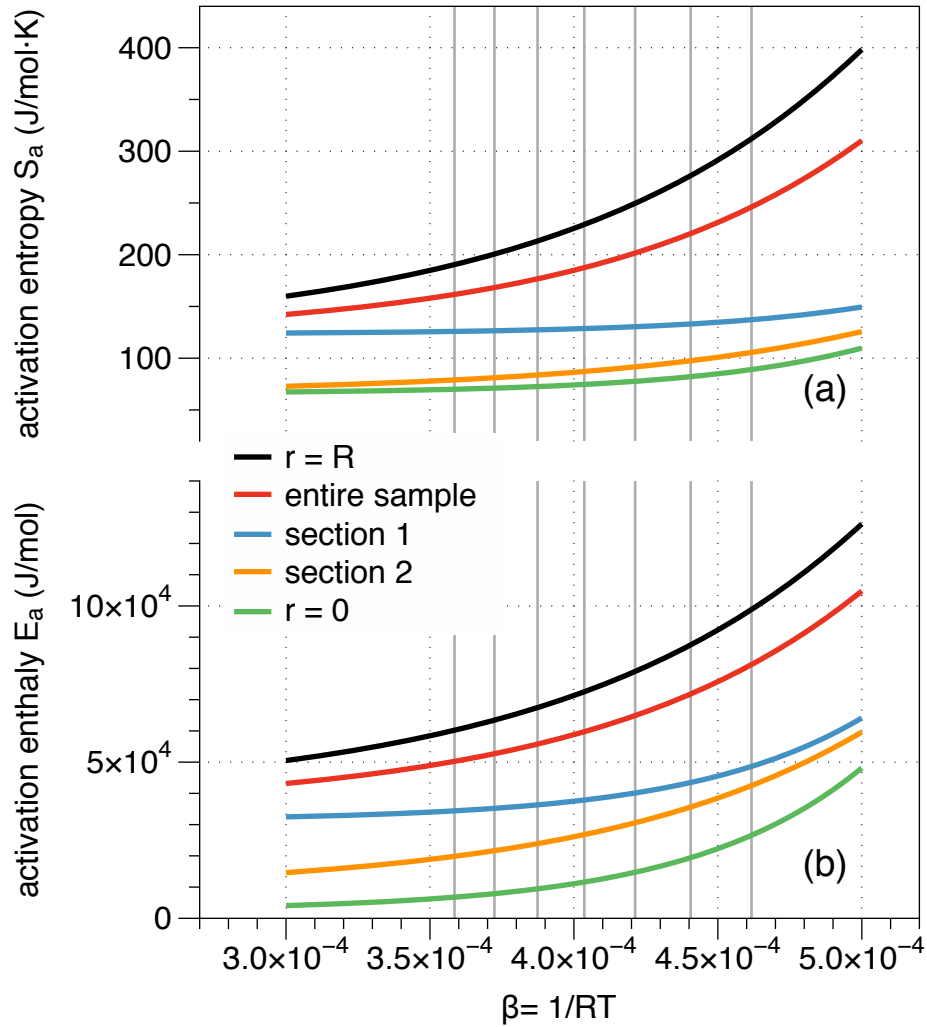
Figure 3.11 (a) Entropy and (b) enthalpy of activation as a function of b for a hybrid electrolyte containing PEO with a molecular weigh of 400 g/mol. The analysis is carried out for measured data of the entire sample and two cleaved central squares of decreasing size, as well as for the calculated data at the outer perimeter and the center of the sample.

A comparison is made between two samples that contain the same amount of salt and approximately the same volume fraction of PEO. The only significant difference between the two is the average molecular weight of PEO, which is 400 g/mol for one and 1000 g/mol for the other. The activation enthalpy of the intact sample is slightly lower for the lower molecular weight system. However, the variation of this quantity as a function of the sample radius is significantly stronger for this system, dropping to values ranging from 10 to 30 kJ/mol in the very center of the sample. While the material with the higher molecular weight also

shows a consistent drop in activation energy towards the center of the sample, the trend is not as pronounced. We interpret the observed behavior as the result of different drying behaviors. Longer polymer chains likely span across several neighboring pores, preventing radially inhomogenous contraction of the pore structure more manifestly compared to shorter chains that may entirely reside in a single pore. In other words, the longer polymer chains are more intertwined with the silica backbone, establishing a more uniform fabric and small radial variance. Conversely, in the material with short polymer chains, polymer and silica backbone can rearrange more independently during shrinkage, which results in more distinctive properties between center and periphery.

For both systems, the entropy of activation decreases towards the center, which means that the structure that develops under tensile mechanical constraints is characterized by an energy landscape that provides fewer choices for cation hopping pathways than structures that form under neutral or compressive conditions. It is, however, interesting to note that the activation entropy increases while the enthalpy decreases, which quantitatively would represent the ideal scenario for enhancing cation mobility, is not observed.

CHAPTER 4   Single Ion Conducting Hybrid Electrolytes

4–1   Introduction

The development of hybrid composite solid electrolytes with desirable mechanical properties, high energy density, and high power density is crucial to develop next generation battery devices. However, the main shortcomings of these electrolytes currently are low ionic conductivity values, low transport numbers for the cation, and lack of mechanical stability limit the utilization of such electrolytes in battery devices. Even though there exist single-ion conducting solid electrolytes with transference numbers close to unity, the conductivity of such electrolytes is below the competitive threshold of 10^{-4} S.cm^{-1} at room temperature. With these challenges, the research described in this chapter focuses on (i) synthesizing a single-ion composite electrolyte with load bearing properties; increasing the volume fraction of the organic phase in the composite electrolyte by introducing oligo PEO; and (iii) characterizing the effect various system parameters have on the transference number of the charge carrying species.

Single-ion solid electrolytes are a class of solid electrolyte that are being studied extensively due to their unique chemical and physical properties.[86, 87] Single-ion polymer electrolytes have the potential to overcome the mass transport limitation associated with dual-ion solid electrolytes. This limitation with dual ions is due to concentration polarization, which creates a concentration gradient resulting in lithium-ion depletion toward the anode when the system is being charged. Even though solid electrolytes containing immobilized anions are very promising in overcoming the limitations of dual-ion systems, there are limitations associated with single-ion conductors as well, specifically single-ion polymer electrolytes. Generally, single-ion conductors that are made of smaller chain length organic polymers lack desired mechanical properties such as high elastic modulus. To improve the mechanical properties of such electrolytes, a composite materials design approach is necessary. This approach can decouple ionic mobility from the mechanical properties of the system, allowing the mechanical properties to be tuned largely independently from the transport properties. With that

in mind, our composite material is based on an inorganic backbone, synthesized using functionalized

tetraethoxysilane (TEOS). The synthesis involves replacing one of the ethoxy groups in TEOS with sulfonyl

(trifluoromethane-sulfonyl)imide (STFSI), which serves as the cation donor. STFSI not only creates a highly

delocalized negative charge but also weakly coordinates the anion and consequently improves the ionic

mobility of the system.[88–90]

Another major drawback of single-ion conducting polymers is the low ionic conductivity of such systems. To

increase the ionic mobility, certain segments of the electrolyte can be modified to lower the overall degree of

crystallinity. Using functionalized TEOS that incorporates a short chain polymer as one of the components of

the backbone, one can decrease the glass transition temperature and improve segmental dynamics.[91, 92]

Increasing segmental dynamics is a promising approach to improve the ionic conductivity of sulfonyl

(trifluoromethane-sulfonyl)imide-based electrolytes. Segmental dynamics have been improved by anchoring

oligo PEO to the inorganic backbone using functionalized TEOS which includes a less rigid polymer such as

PEO in the continuous network. Filling up the pores of the backbone with PEO also changes the segmental

dynamics. This approach relies on the van der Waals interactions of the polymer chains with the pore walls

made of the inorganic backbone.

4–2   Review of the structure and conductivity for single-ion conducting polymer electrolytes

4–2.1   Anionic carboxylate and sulfonate groups

One of the key factors that influences the properties of polymeric single-ion conductors is the nature of

negatively charged organic moieties such as carboxylate or sulfonate groups, which are typically larger in size

compared to lithium, less mobile, and can therefore be viewed as cation donors. Initial efforts to tune the

properties of the cation donor were based on using carboxylate groups to act as Lewis acids, shown in

Schematic 4.1. The initial materials design conducted by Kubo *et al.* revolved around using polyether (PEO or

P(EO/PO)) and a polyanionic lithium salt (Poly(Li-Sorb) or Poly(Li-Muco)) with or without $BF_3 \cdot OEt_2$. The

presence of BF_3 plays a key role in the dissociation of lithium ions when carboxylate anions complex with

BF$_3$. This complex formation promotes the delocalization of the negative charge. In addition, this system has

relatively high transference numbers, 0.45-0.88, mainly due to the fact that the counter anion is immobilized.[93]
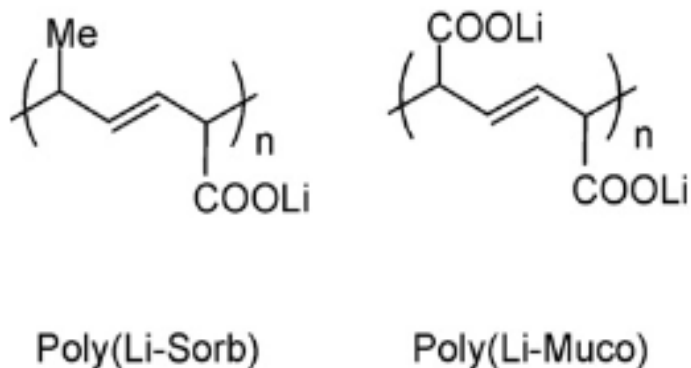
Scheme 4.1   The structure of polyionic salts used in single ion conductors

Addition of oligo PEO (400-900 MW) through an esterification reaction is another approach that has been

shown to improve the overall conductivity of single-ion conductors. This approach was first reported with

the work of Gohy *et al.* Schematic 4.2 shows the final product, which includes a polystyrene moiety in

addition to the esterified oligo PEO. The conductivity of this system was further improved through the

addition of BF3 reaching 10^{-5} S·cm^{-1} at room temperature.
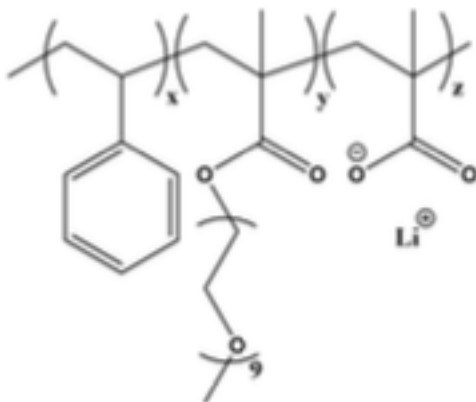
Scheme 4.2   Structure of single ion conductor with esterified oligo PEO

Sulfonate groups are another weakly coordinated complex that has been extensively used in single-ion conducting electrolytes. As shown below, various chain lengths of PEO can be incorporated into the backbone of the polymer to facilitate lithium ion transport. Colby and coworkers have shown that increasing the chain length of the oligo PEO can increase the overall crystallinity of the system.[94]
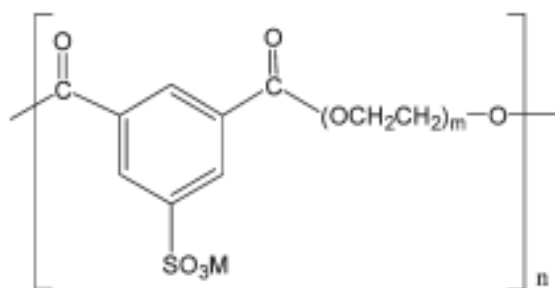
Scheme 4.3   Structure of sulfonate based single-electrolyte with esterified PEO chain

As mentioned previously, the higher the degree of crystallinity of the polymer in an electrolyte, the lower the ionic conductivity of a given system. To suppress crystallization of polymer in an electrolyte, various strategies have been developed. One approach relies on creating a copolymer of poly(p-phenylene oxide) (PPO) and PEO to design a triblock single-ion conductor. It is very also practical to use short chain PEO in a comb fashion. This approach was first developed by Sun et al and ionic conductivities of 2.0×10^{-7} S.cm^{-1} were obtained at 25ºC with a EO/Li=40.[95–97]

Composite	Ionic conductivity (S/cm)	Transference number	References
Polyether,polyethylene oxide blended with SICPE	10^{-4} - 10^{-5} at 80 ℃ (dry)	0.45~0.88	98
Block copolymer of poly(ethylene glycol methacrylate), polystyrene and poly (lithium methacrylate)	10^{-8} - 10^{-11} at 25 ℃ (dry)	0.84	99
PEG ionomers with sulfonate anion	6.27×10^{-7} at 25 oC	N/A	94
Triblock SICPE with PEO,PPO and poly(lithium 2,3,5,6-tetrafluorostyrene-4-sulfonate)	10^{-6} (R.T.)	N/A	100
Comb-shaped copolymer of PEO and sulfonate monomer	2.0×10^{-7} (R.T.)	N/A	101

Block copolymer of LiMTFSI and PEO	2.3×10^{-6} (R.T.)	0.83	[102]
Random copolymer of LiSTFSI and PEGMEA	2.4×10^{-4} (R.T.)	> 0.9	[103]
PDMS backbone grafted with LiSPSI	7.2×10^{-4} (R.T.)	0.89	[104]
PEO blended with LiSsTFSI	1.35×10^{-4} 90 ℃	> 0.9	[27]
Copolymer of polyethylene and LiAFSI	5.84×10^{-4} (R.T.)	0.91	[105]
Block copolymer of PEO and LiSTFSI	10^{-4} - 10^{-7} at 60 ℃	0.87-0.99	[106]
Homopolymer poly(PEOMA-TFSI–Li$^+$)	10^{-4} - 10^{-5} at 90 ℃	0.97-0.99	[107]

Table 4.1   Summary of various polymer based single-ion conductors

4–2.2   Sulfonyl(trifluoromethane-sulfonyl)imide (TFSI⁻) group and its derivatives

There are a few important factors that influence the dissociation of lithium ions from their counter anions. One of these factors is the ability of the anion to delocalize its negative charge. One molecular design approach that can enhance the delocalization of negative charge is the use of bulky conjugating units. The addition of electron withdrawing groups such as haloalkyl, carbonyl, cyano, ammonium, and nitro groups can have a similar effect. The following structures have been studied and incorporated extensively in single-ion conducting polymer electrolytes: sulfonyl(trifluoromethane-sulfonyl)imide (SO_2-N(-)-SO_2-CF_3) and trifluoromethane-sulfonyl imide (N(-)-SO_2-F_3).[108]
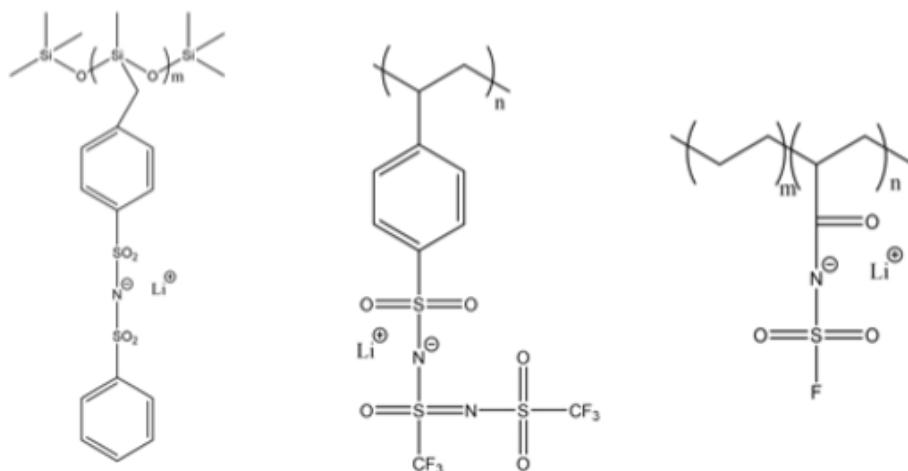
Scheme 4.4   The structure of various polymer based single-ion conductors

Another monomer that has been widely investigated is lithium (4-styrenesulfonyl) (trifluoromethane-sulfonyl)-imide (LiSTFSI). The low ionic conductivity of this monomer at room temperature is associated with its high glass transition temperature (T_g). To lower T_g and improve the ionic conductivity, physical blending of PEO with LiSTFSI synthesized via free radical polymerization can be employed. This approach, as mentioned earlier, enhances the segmental dynamics of the LiSTFSI.

4–2.3   Use of PEO in single-ion conductors

Various polymer fillers can be used to optimize not only the mobility of cations but also improve the mechanical properties and the thermal stability of single-ion conducting polymer electrolytes. The use of PEO as a spacer has been investigated extensively in single ion composite polymer electrolytes due to cost effectiveness and compatibility with the various components of the composite. There are two ways in which PEO can be introduced in the silica matrix. PEO can be either percolated into the pores of the silica matrix where it interacts with the inorganic phase via dispersive interatomic forces, or it can be chemically grafted to the silica matrix by various available synthesis methods. Poly(ethylene oxide)-b-poly[(styrene-4-sulfonyltrifluoromethylsulfonyl)imide lithium] (PEO−P[(STFSI)Li]) has been investigated by Balsara et al.[109] It has been shown that the molecular weight of the block-copolymer can impact the degree of the crystallinity

of the system. At low temperatures, clusters of the PSLiTFSI were formed since the crystalline phase is thermodynamically more favorable. As the temperature is increased above the melting point, the ionic conductivity of the system improves drastically.[109] Utilizing shorter chain length PEO can block the formation of crystalline regions. Incorporating shorter chain length polymer might not improve the mechanical properties of the system significantly but the ionic conductivity values can reach 10^{-5} S.cm^1.

We can also use PEO as a spacer in different parts of a SICPE to tune the structure of the material. Maranas *et al.* have shown that the compatibility of various structures of SICPEs can be improved by using fixed chain length PEO covalently bonded to the backbone.[110] Matyjaszewsk *et al.* have used click chemistry to synthesize a PEO-based macromonomer PEOMA-TFSI$^-$Li$^+$. The presence of the PEO in the system improved the segmental dynamics significantly resulting in the formation of an amorphous lithium conducting phase.[111]

4–3   Transport number *vs.* transference number

The transport number is defined as the ratio of electric current derived from positively charged ions to the total electric current of the system.[112] Accordingly, for a system containing only one positively and one negatively charged species, the transport number for a cation is

$$t_+ = \frac{\mu_+}{\mu_+ + \mu_-}$$
(4.1)

where μ_+ and μ_- are the are the mobilities of the cation and anion, respectively.[113]On the other hand, for systems that contain multiple positively and negatively charged species, the transference number of a specific cation species is defined as the number of moles of that element transferred by migration per one mole of electrons. For instance, a general LiY salt can dissociate into Li$^+$, Y$^-$, [Li$_2$Y]$^+$ and [LiY$_2$]$^-$. The transference number for lithium is defined as the sum of the transport number of positively charged species containing lithium which is show below:

$$T^+ = t[Li]^+ + t[Li2Y]^+ - t[LiY2]^-$$
(4.2)

If there is in no ion dissociation, transference number and transport number are the same ($T^+ = t^+$, $T^- = t^-$).

Transport numbers can have values between 0 and 1. However, there is no limit for the values of transference numbers. It is even possible to have negative values for the transference numbers. If the mobility values for $[LiY_2]^-$ were higher than the combined mobility values for Li^+ and $[Li_2Y]^+$, the transference number for lithium ion can be less than zero.

4–4   Effects of high lithium ion transport numbers

Dendrite growth in lithium-ion batteries can result in low Coulombic efficiency and increased safety concerns. Conventional electrolytes use dual ions, and exhibit low lithium ion transport numbers. A low Li^+ transport number essentially means that most of the ionic conductivity is not attributed to the cation conductivity, which results in dendrite growth. The processes associated with the electrodeposition of lithium onto the electrodes are the fundamental cause of dendrite growth. More specifically these processes are associated with the flux and transport of lithium ion near the surface of anode and cathode.[107, 114]

When lithium ion is electrodeposited onto the anode at a constant current density, there is a moment in which the concentration of salt near the electrode is close to zero. In other words, the surface of the anode is depleted of lithium ions. This occurs when lithium ions are being consumed by the anode faster than the diffusion flux can replenish lithium ions near the anode. This creates and instability within which lateral fluctuations provoke creation of preferred transport channels carrying lithium towards the anode and initiation of lithium dendrite growth. This sequence of events yields Sand's time, the time when lithium dendrite starts growing, which is shown below:

$$\tau = \pi D \left(\frac{eC_0}{2Jt_a}\right)^2 \tag{4.3}$$

where τ is Sand's time (s), D is the diffusion coefficient of the metal ions (cm² s⁻¹), e is the electronic charge (C), C_0 is the ion concentration in the bulk electrolyte (mol cm⁻³), J is the current density (A cm⁻²),and t_a is

the transport number of anions which is equal to $(1-t_{Li})$.[115] The factors that describe the diffusion coefficient were introduced in Chapter 2

$$D = \gamma d_0^2 \nu_D e^{-\Delta G_a/k_B T} = \gamma d_0^2 \nu_D e^{S_a/k_B} e^{-E_a/k_B T},$$

where the definitions for all terms in this expression are provided in the corresponding section. As shown in the equation above, Sand's time is inversely proportional to the square of the anion transport number. As a result, the main emphasis here is to develop a solid-state electrolyte with high lithium ion transport numbers, thus reducing that of the anions and raises Sand's time beyond the duration of the charging cycle, which in turn suppresses dendrite growth.

4–5   Materials fabrication

4–5.1   Materials

Tetraethyl orthosilicate (reagent grade, 98%), Trifluoromethanesulfonamide (95%), Triethylamine (99.5%), and dichloromethane (anhydrous, 99.8%) were purchased from Sigma Aldrich.

4–5.2   Synthesis of silica backbone

To obtain a porous silica backbone, 14.8 ml of TEOS is mixed with 4 ml of water in a plastic beaker. Then, 0.8 ml of HCl (1M) is added to initiate the acid catalyzed reaction. The solution is stirred at room temperature for approximately two hours until it is fully homogenous. The temperature is raised to 65 °C to initiate the polycondensation process.

4–5.3   Synthesis of triethylammonium trimethoxysilane

Trifluoromethanesulfonamide (1 g, 0.006 mol) along with triethylamine (0.6 g, 0.006 mol) are added to 28 ml of dichloromethane. The solution is stirred until fully dissolved. Then 4-[2-(trimethoxysilyl)-ethyl]benzene-1-sulfonyl chloride (4.28 g , 0.0131 mol) was added to the mixture and stirred for 24 hours at 40°C. A waxy

dark orange product is obtained after distillation of the solution. The next step involves the hydrolysis by addition of water (0.4 g , 0.023 mol) and ethanol (3.94 g , 0.085 mol) and homogenizing the product at 45 °C for 2.5h.

4–5.4 Grafting cation donor to oligo PEO

The pre-hydrolyzed anion is mixed with a specific amount of lightly gelled backbone precursor at 65°C, the solution is stirred for 30 min, then the viscous solution is cast into a plastic container and left to gel. The gel is then moved into the oven and aged at 50°C for 24h. A transparent yellow colored silica backbone is obtained. The backbone is then washed with deionized water first followed by ethanol.

4–5.5 Ion exchange and polymer percolation

To replace triethylammonium ions with lithium ions, the gel was submerged in a solution of lithium hydroxide (0.2 g, 0.008 mol) dissolved in 200 ml of deionized water. The ideal processing time for the ion exchange is two hours. To remove the excessive lithium hydroxide, the gel is washed with water and ethanol consecutively. To fill the pores of the inorganic backbone with polymer, the ion exchanged product is submerged in 50 ml of polyethylene glycol (600 MW) at 45°C for 12 hours. The final product is dried in a heated vacuum oven at 50 °C for 24 hours.

4–5.6 Percolation of propylene carbonate (PC) and ethylene carbonate (EC)

80 wt.% EC and 20 wt%. PC solutions with or without added lithium perchlorate (1M or 0.5M) were prepared. The gelled backbones with or without grafted oligo-PEO were submerged in the solution for five to six hours. The samples were transferred to petri dishes and kept at room temperature for future experiments.

4–6   Results and Discussion

4–6.1   Ionic Conductivity

The ionic conductivity of the hybrid composite materials prepared as described above are measured as a function of temperature using EIS. We first focus on ascertaining that replacing a larger cation, in this case triethylammonium, with smaller molar mass cation (lithium ion) indeed results in higher ionic conductivity of our material. As described in section 5.5, triethylammonium is replaced with lithium ions. Fig. 4.1 contains two groups of data, color coded according to EO to cation ratios of 13, 15 and 25. The circular symbols indicate that the material contains triethylammonium cations, corresponding to the materials before the cation exchange, and the square symbols indicate that the positive charge carriers are lithium, i.e., after the cation exchange. Comparing the ionic conductivities between both groups of samples shows that for those containing lithium ions (at the same cation concentrations) conductivities are systematically higher (Fig 4.1). These results are in general agreement with the behavior we would expect for an amorphous solid electrolyte; that replacing a larger molar mass cation with a smaller molar mass cation would result in increase of ionic conductivity for a given material.

We also change the molar ratio of ethylene oxide to lithium ion to determine what effect the relative ratio of lithium ion has on the overall conductivity of the system. Increasing the concentration of lithium ions relative to ethylene oxide results in an increase in ionic conductivity. However, a very high concentration of lithium ion $\frac{EO}{Li} < 10$, causes the material to plasticize exceedingly and makes it unstable.
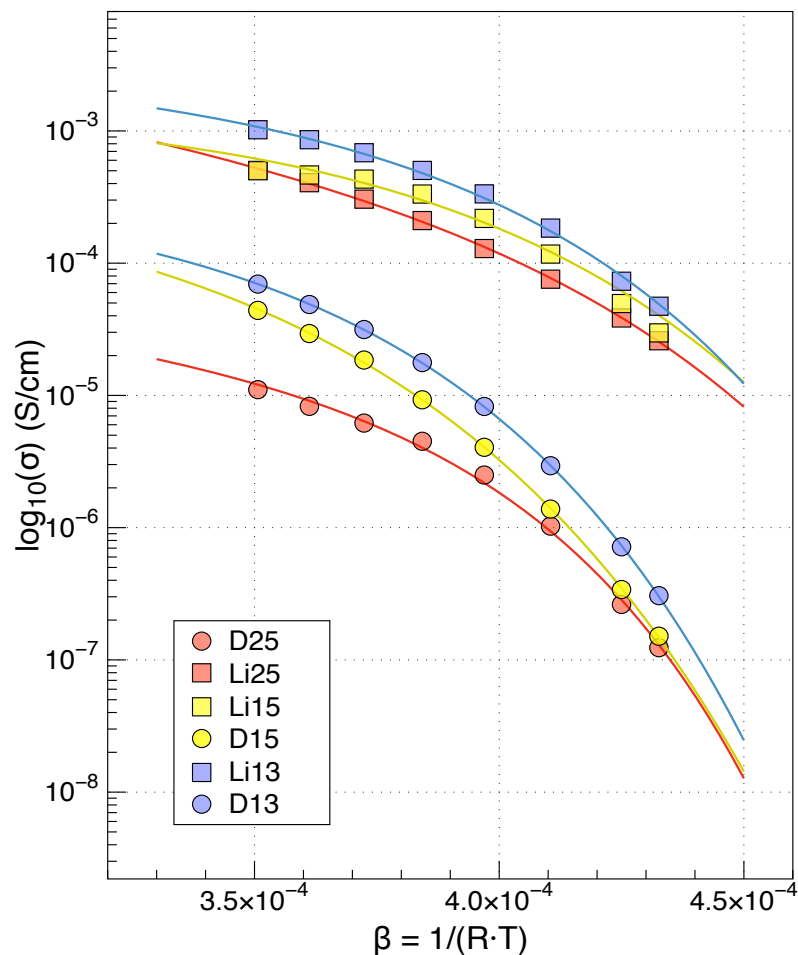
Figure 4.1   The temperature dependent ionic conductivity of hybrid electrolytes with lithium and triethylammonium ions as the conducting species. The ethylene oxide to triethylammonium molar ratio is labeled as D and ethylene oxide to lithium ion molar ratio as Li.

Next we focus on understanding how additionally anchoring oligo-PEO to the silica scaffold affects the ionic conductivity of hybrid electrolytes in comparison to those having only short-chain PEO interacting via weaker dispersive forces with the backbone. Comparing temperature depended ionic conductivity results for grafted oligo-PEO) *vs.* non-grafted PEO provides information about the effectiveness of immobilizing the polymer filler. Indeed, the hybrid electrolytes with grafted oligo-PEO have higher conductivity values at all temperatures compared to non-grafted polymer. (Keep in mind, though, that samples with grafted oligo-PEO also contain short-chain PEO.)

The material with $\frac{EO}{Li}$=15 shows higher conductivity values at temperatures below 30 °C compared to the electrolytes with $\frac{EO}{Li}$=30. Moreover, samples with $\frac{EO}{Li}$=15 show less of a change with temperature in their ionic conductivity data, suggesting that for this material cation transport in this system has an overall lower activation energy. This is somewhat surprising, given that the chemical makeup of the conducting phase is the same for both materials. On the other hand, since more cation donors are incorporated into the silica backbone, the network topology of the inorganic phase is different between the two systems. More work is required to gain a better understanding of the reason for the observed behavior.
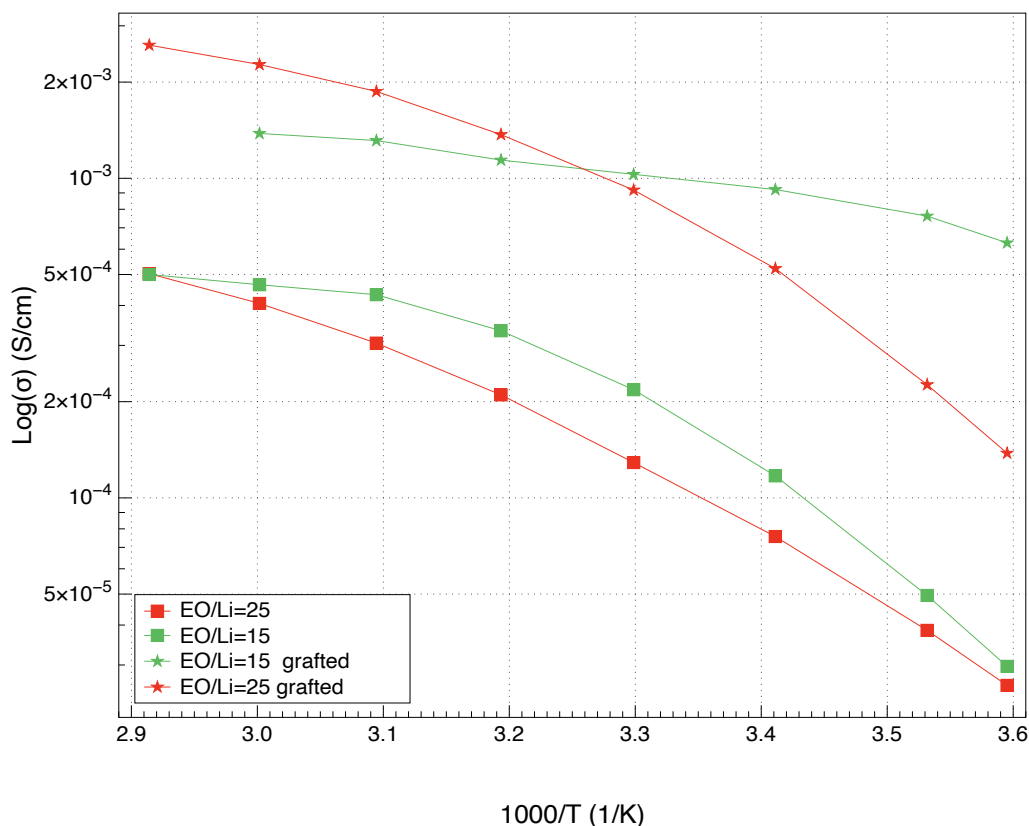
Figure 4.2   The temperature dependent conductivity of hybrid single-ion conductors with grafted PEO (oligo PEO) and non-grafted PEO.

In chapter 2 we concluded that increasing the fill factor of polymer in the pores of the silica scaffold by using a mixture of is beneficial to cation conduction. Hence, our next focus is to add organic molecular filler to the system and examine how its ionic conductivity changes. This work is still ongoing, and here we report only

initial findings. In this set of experiments, pores of the backbone are filled with propylene carbonate and ethylene carbonate, which are commonly used in liquid electrolytes. Since our silica backbone is highly porous (>90% porosity), using a viscous liquid such as EC/PC can effectively fill the pores and consequently increase the ionic conductivity. As discussed in section 5.6, different mixtures of EC/PC with lithium perchlorate concentrations of 0, 0.5, or 1 molar are used to fill the pores of the inorganic backbone. We also graft oligo-PEO to the backbone of some of the samples, but none of the samples reported here contain extra short-chain PEO. On the other hand, all samples contain the same amount of cation-exchanged TFSI donor groups embedded in the backbone, as described in section 5 above.

The ionic conductivities of these samples are plotted as a function of temperature in Figure 3. The data reveals that addition of lithium perchlorate (on top of the cations provided by TFSI groups) drastically improves the ionic conductivity of the hybrid electrolytes and the maximum ionic conductivity is achieved when a 1M solution of lithium perchlorate is used in combination with EC/PC. The results also show that anchoring oligo-PEO to the backbone in the presence of EC/PC is an effective approach to increase the ionic conductivity of the system. This finding is in accordance with our previous study that immobilizing PEO has a positive effect on improving the ionic mobility of our hybrid electrolytes. In summary, this materials system combines several factors that each by themselves enhance the cation transport rate: (i) the TFSI functional groups immobilize some the cation donor anions; (ii) the nano-porous silica backbone structure in combination with oligo-PEO molecular brushes prevent the organic phase in the pores from flowing freely; (iii) despite the increased viscosity, EC and PC molecules exhibit strong localized mobility, likely in excess of what polymer segments do. Factors (i) and (ii) improve cation transference numbers and reduce osmotic drag, while factor (iii) lowers the activation barrier for cation hopping.
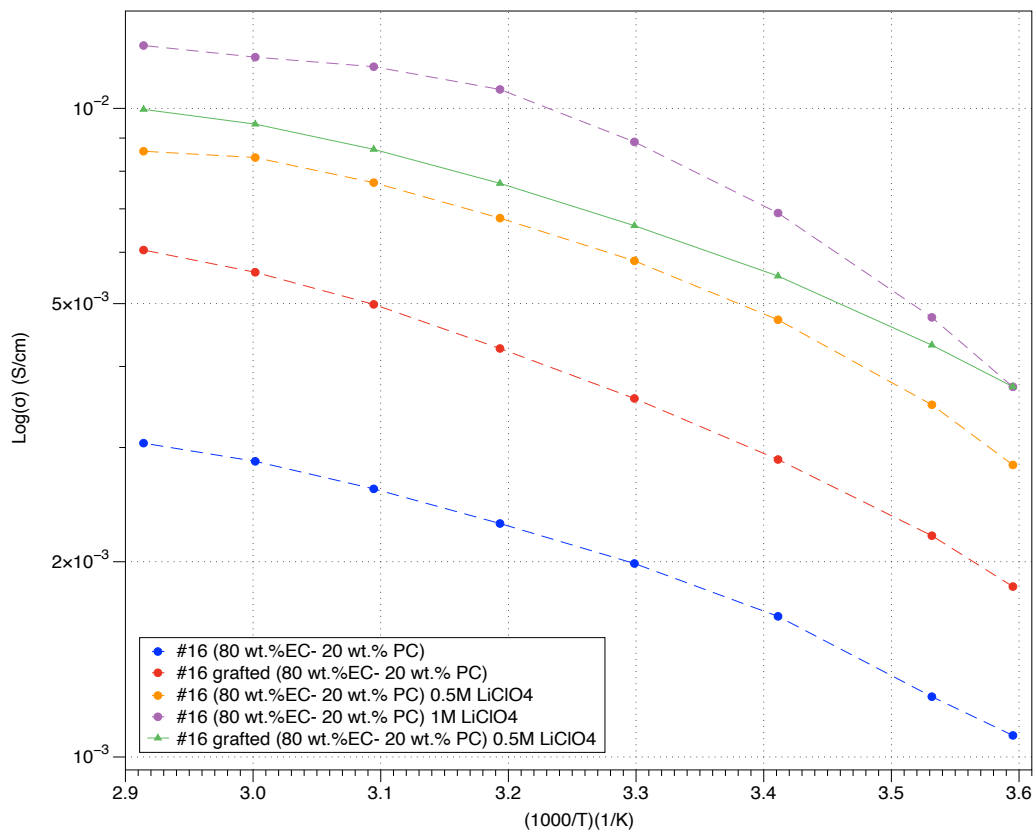
Figure 4.3 Conductivity of hybrid electrolytes mixed with various weight fraction of propylene carbonate (PC) and ethylene carbonate (EC) with or without added lithium perchlorate

4–6.2   FTIR

We used FTIR spectroscopy to verify that the synthesized inorganic backbone contains TFSI. The FTIR data for silica and functionalized TEOS, 2-[(trifluoromethanesulfonylimido)-N-4-sulfonylphenyl]ethyl-trimethoxysilane, which is polymerized by an acid catalyzed sol gel process, is shown in Figure 4. The presence of three sharp peaks in the 1300-1500 cm^{-1} region distinguishes the spectra of silica and the functionalized TEOS. The strong peaks corresponding to sulfonamide at 1335-1372 cm^{-1}, trifluoro group at 1132-1190 cm^{-1}, and symmetric sulfoxide group (SO$_2$) at 1030-1070 cm^{-1} confirm the presence of the cation donor in the form of a functionalized TEOS.
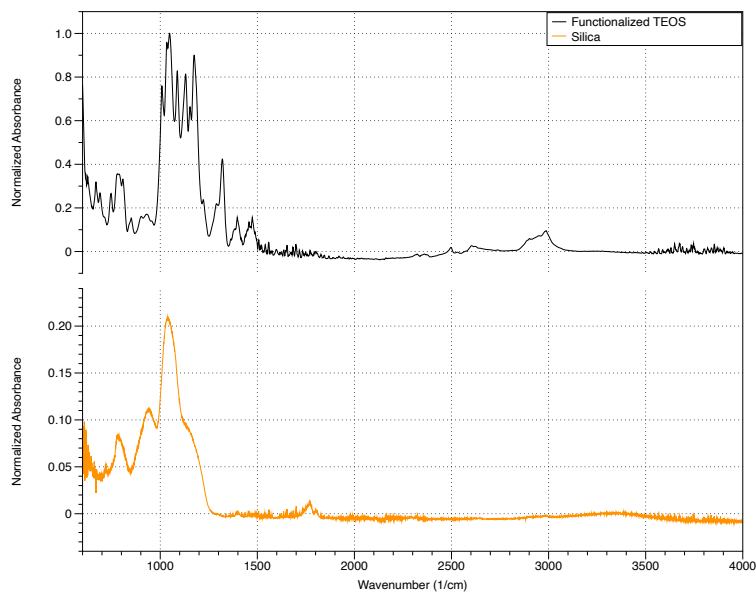
Figure 4.4   The FTIR of 2-[(trifluoromethanesulfonylimido)-N-4-sulfonylphenyl]ethyl-trimethoxysilane shown in black and pure TEOS in yellow

4–6.3   Thermogravimetric Analysis

The organic content of the composite solid electrolytes is an important parameter in determining their ionic conductivity. Hence, thermogravimetric analysis was performed to obtain the mass fraction of polymer in the composite. To obtain precise results, TEOS (100 wt.%) was polymerized using an acid catalyzed sol-gel process and was used as the control group during the TGA measurements. Functionalized TEOS, 2-[(trifluoromethanesulfonylimido)-N-4-sulfonylphenyl]ethyl-trimethoxysilane, was also synthesized using the methods described earlier to be used as the other control group during the TGA measurements. The TGA results, shown in figure 6, reveal that all weight loss for the hybrid composite electrolytes occur below 700 °C. The weight loss in the 130 °C to 250 °C range corresponds to desorption of water from the surface of the composite material and subsequent condensation of SiOH groups.[116] Physiochemical transformations such as changes in conformations of molecules, melting, initial defragmentation occur at lower temperatures as well. For the functionalized TEOS, the weight loss of the functional group (anionic TFSI group) occurs mostly in the 350 °C to 400 °C range. The inorganic backbone, which is synthesized using functionalized TEOS does not contain PEO. As a result, no steep weight loss is observed at temperatures below 350 °C.

78

The single-ion conducting composite electrolytes that contain PEO (600MW) show a higher weight loss compared to functionalized TEOS without PEO. As expected, samples with EO to donor ratios of 13 show the highest weight loss, which translates to the largest volume fraction of polymer in the composite. It can also be concluded that the composite materials design approach further improves the thermal stability of the electrolytes. The evidence for the thermal stability of the material is that weight loss is not observed at temperatures below 130 °C.
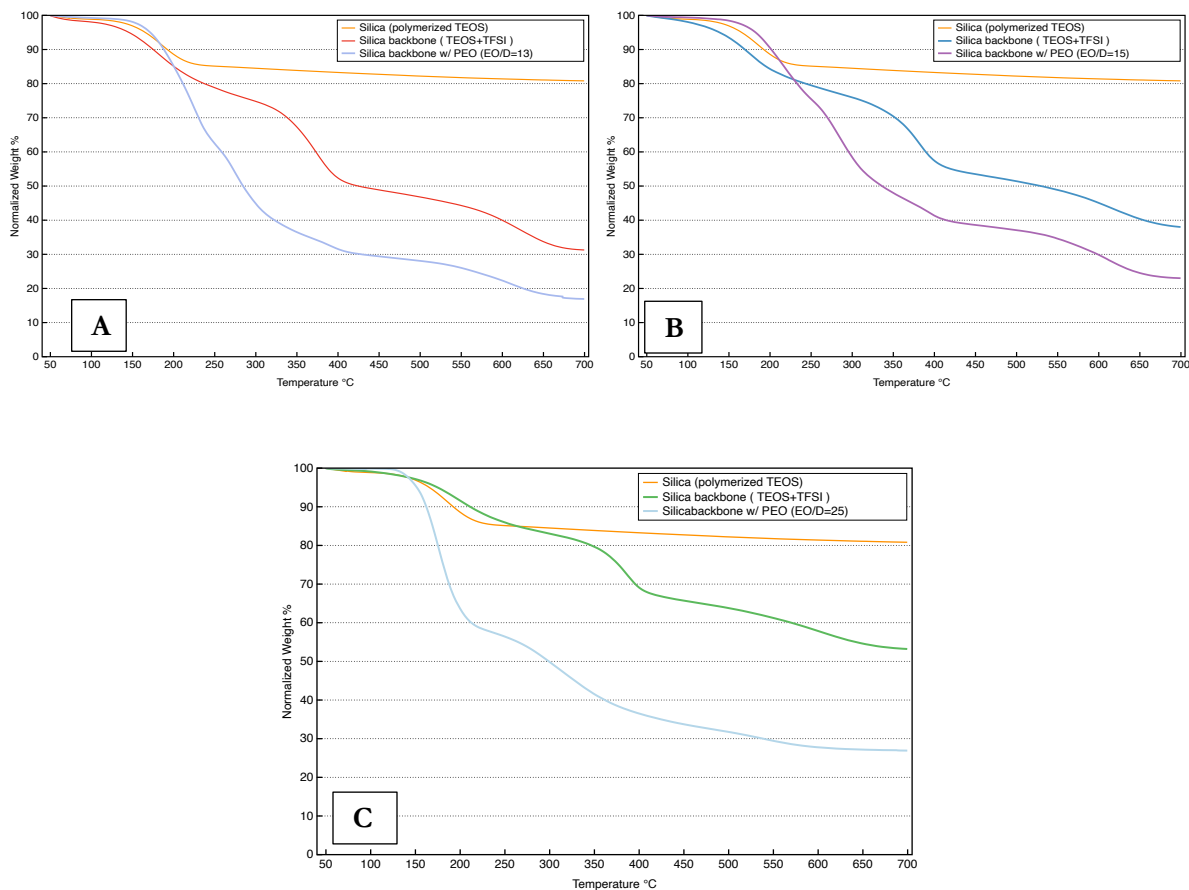
Figure 4.5   The thermograms of pure silica, silica backbone (polymerized TEOS with TFSI) and A) silica backbone with added PEO (600MW) (EO/D=13) B) silica backbone with added PEO (600MW) (EO/D=15) C) silica backbone with added PEO (600MW) (EO/D=25)

4–6.4   Transport number

The Bruce-Vincent method was used to obtain the transport number of our single ion electrolyte. The measurement is based on combining DC voltage and AC impedance in a symmetric cell with non-blocking lithium metal electrodes at 20°C. The DC voltage is set to 30 mV for 1000s, and the sample size is 0.712 cm².

The transport number is calculated using

$$t_{Li}^{+} = \frac{I^{\infty}R_E^{\infty}(\Delta V - I^0 R_I^0)}{I^0 R_E^0(\Delta V - I^{\infty}R_I^{\infty})},$$

(4.4)

in which ΔV is applied constant potential across the Li/#16 Li/Li symmetric cell, R_E and R_I are the resistances of the electrolyte and interphase, I is the current and 0 and ∞ correspond to initial and steady state. [117]

Results are shown in Fig 4.6 and Table 2. All Nyquist plots are clearly composed of two depressed semicircles. The semicircle in the high frequency region is the resistance through the solid electrolyte interface layers, while the one at middle frequency represents the charge transfer resistance at the electrode/electrolyte interface (R_I). The intercept of Nyquist curves at Z' axis (R_E) is the combination resistance which is attributed to the ionic resistance of the electrolyte and the contact resistance at the electrode/electrolyte interface.[118]
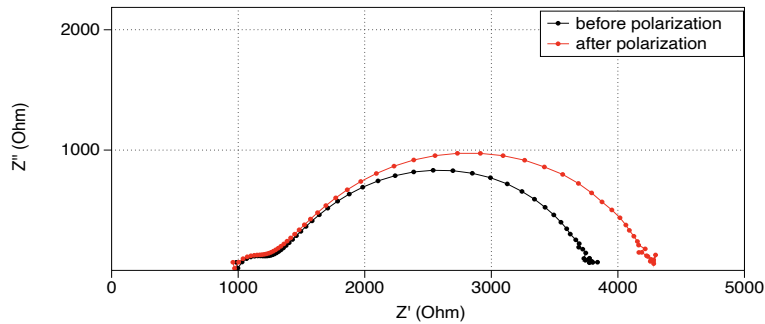
Figure 4.6   The AC impedance spectra of Li ‖ Li at 20 °C before and after DC polarization
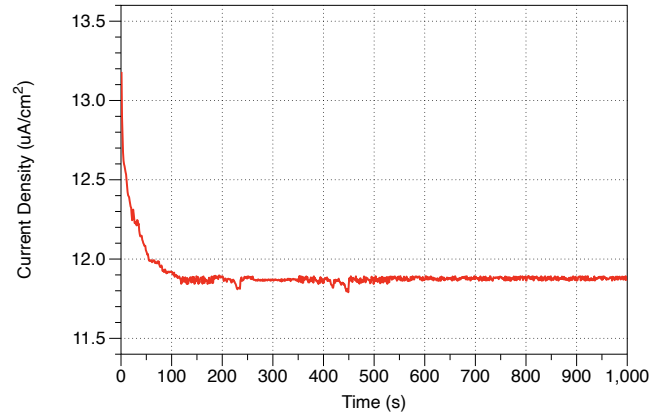
Figure 4.7   The current response of Li∥Li cell as a function of time during DC polarization under a constant potential of 30 mV.

	I (μA)	R_E (Ω)	R_I (Ω)
Before Polarization	9.88	997	2799
After Polarization	8.44	971	3309

Table 4.2   Result of the transference number measurement for #16 Li sample.

The obtained transference number for this system is 0.9 which confirms that our electrolyte is a single-ion conductor.

CHAPTER 5   Summary and Outlook

Solid electrolytes have the potential to significantly improve battery technology, in particular with respect to durability, energy density, and the ability to incorporate them into multi-functional structures. Since, the performance criteria that are expected of solid electrolytes are controlled by opposing factors, a composite design appears to be most logical approach. In this research we pursued the development of nano-scale hybrid materials that combine organic and inorganic constituents in a thermodynamically stable manner, i.e., by coalescing disparate material types using covalent chemical bonds, and that yield cation conductivities nearing commercially viable levels.

Initial materials designs based on GLYMO and mPEG-NH$_2$ chemistry turned into a challenge, numerous repetitions, and continued refinement of the parameters that control the process. Ultimately, this approach did not lead to the desired goal, but served as a valuable learning experience in that it led us to the discovery of strong inhomogeneities and anisotropies that develop in these sol-gel derived materials. Indeed, it is quite remarkable that by mechanically conditioning the material, in our case it has been radial and tangential stresses that develop in a cylindrical disk during drying, it is possible to obtain cation mobilities that vary between two and three orders of magnitude without any changes to the chemical constitution of the material. This is the most thought provoking outcome of this thesis research, in that it begs a number of questions. For one, considering that chemical composition appears to be the foremost design parameter being canvassed by researchers in pursuit of the top performing solid electrolyte, is that the right approach? What do we know about a "theoretical limit" in ionic conductivity for a given materials type, structure, or chemistry? How many different ways can we conceive to fabricate a material of a given composition, and how many different results for a chosen figure of merit will we measure? In our system, we found that in the very center, the ionic conductivity is a thousandfold higher than at its outer edge. How can we harness this

advantage? How can we adjust all of the structure across the entire material to exhibit a uniformly high ionic conductivity.

Ultimately, we succeeded at well-performing solid electrolytes by following the original idea of a covalently melded hybrid material using TFSI functional groups, oligo-polymer brushes, and ion exchange processing. We demonstrated that covalent bonding between physico-chemically contrasting materials constituents outperforms simply mechanically mixing them. This is the most satisfying outcome of this thesis research, in that it showed that a logical concept, provided it is well thought through and no ill-conceived implicit assumption have been overlooked can be brought to fruition. It provides a valuable guideline for how to conduct scientific research, as well as the trust we can place in it.

This is the second PhD thesis in our research group that is based on the hybrid material (or nanocomposite) design concept, and it has strengthened the outlook with respect to the success of these solid electrolyte materials beyond what was achieved during the first thesis. The performance characteristics of the materials we fabricated are very promising. Overcoming, the barrier of one $mS \cdot cm^{-1}$ and achieving cation transference numbers close to unity appear to be well within reach, making these materials commercially viable. In fact, an invention disclosure has been filed with the university's office of technology transfer.

Finally, we also developed new analytical concepts. Specifically, by using the correlation between adiabatic elastic moduli and the activation energy for cation hopping we were able to carry out more sophisticated and insightful data interpretation. Similarly, the notion that the activation free energy varies with the structural state of the material allowed us to analyze data in ways that are consistent with transition state theory and that yielded new revelations, such as the fact that the activation entropy can be more significant in defining atomic mobility than the activation enthalpy. So far, activation entropy has been difficult to access, and therefore has been ignored by most researchers. We have laid the groundwork for a new way of scrutinizing thermally activated processes, which hopefully will contribute to advancing the theoretical framework for describing this phenomenology, especially for the amorphous state of matter.

References

1   B.P. Koirala, R.A. Hakvoort, E.C. van Oost, and H.J. van der Windt, 'Community energy storage: Governance and business models,' *Consumer, prosumer, prosumager: How service innovations will disrupt the utility business model* 209 (2019).

2   R. Sims, '*Energy-smart farming : efficiency, renewable energy and sustainability*,' (Burleigh Dodds Science Publishing, Philadelphia, 2022)

3   J.A. Hernandez, D. Velasco, and C.L. Trujillo, 'Analysis of the effect of the implementation of photovoltaic systems like option of distributed generation in Colombia,' *Renewable and sustainable energy reviews* **15**, 2290 (2011).

4   S. Sagadevan, M.R. Johan, A.R. Marlinda, O. Akbarzadeh, K. Pandian, M.M. Shahid, F. Mohammad, and J. Podder, 'Background of energy storage,' in *Advances in Supercapacitor and Supercapattery*, (Elsevier, 2021), p. 1.

5   P.-J. Lian, B.-S. Zhao, L.-Q. Zhang, N. Xu, M.-T. Wu, and X.-P. Gao, 'Inorganic sulfide solid electrolytes for all-solid-state lithium secondary batteries,' *Journal of Materials Chemistry A* **7**, 20540 (2019).

6   K.B. Hatzell, X.C. Chen, C.L. Cobb, N.P. Dasgupta, M.B. Dixit, L.E. Marbella, M.T. McDowell, P.P. Mukherjee, A. Verma, and V. Viswanathan, 'Challenges in lithium metal anodes for solid-state batteries,' *ACS Energy Letters* **5**, 922 (2020).

7   W. Xu, J. Wang, F. Ding, X. Chen, E. Nasybulin, Y. Zhang, and J.-G. Zhang, 'Lithium metal anodes for rechargeable batteries,' *Energy & Environmental Science* **7**, 513 (2014).

8   C. Monroe and J. Newman, 'Dendrite growth in lithium/polymer systems: A propagation model for liquid electrolytes under galvanostatic conditions,' *Journal of The Electrochemical Society* **150**, A1377 (2003).

9   M.B. Dixit, W. Zaman, N. Hortance, S. Vujic, B. Harkey, F. Shen, W.-Y. Tsai, V. De Andrade, X.C. Chen, and N. Balke, 'Nanoscale mapping of extrinsic interfaces in hybrid solid electrolytes,' *Joule* **4**, 207 (2020).

10   J.C. Bachman, S. Muy, A. Grimaud, and H.H. Chang, 'Inorganic solid-state electrolytes for lithium batteries: mechanisms and properties governing ion conduction,' *Chemical Reviews* (2016).

11   Z. Gao, H. Sun, L. Fu, F. Ye, Y. Zhang, and W. Luo, 'Promises, challenges, and recent progress of inorganic solid-state electrolytes for all-solid-state lithium batteries,' *Advanced Materials* (2018).

12   X. Miao, H. Wang, R. Sun, C. Wang, and Z. Zhang, 'Interface engineering of inorganic solid-state electrolytes for high-performance lithium metal batteries,' *Energy & Environmental Science* (2020).

13   D. Liu, W. Zhu, Z. Feng, A. Guerfi, A. Vijh, and K. Zaghib, 'Recent progress in sulfide-based solid electrolytes for Li-ion batteries,' *Materials Science and Engineering: B* **213**, 169 (2016).

14   J. Lee, T. Lee, K. Char, K.J. Kim, and J.W. Choi, 'Issues and Advances in Scaling up Sulfide-Based All-Solid-State Batteries,' *Accounts of Chemical Research* **54**, 3390 (2021).

15   C. Wang, K. Fu, S.P. Kammampata, D.W. McOwen, A.J. Samson, L. Zhang, G.T. Hitz, A.M. Nolan, E.D. Wachsman, and Y. Mo, 'Garnet-type solid-state electrolytes: materials, interfaces, and batteries,' *Chemical Reviews* **120**, 4257 (2020).

16   Z. Hu, J. Sheng, J. Chen, G. Sheng, Y. Li, X.-Z. Fu, L. Wang, R. Sun, and C.-P. Wong, 'Enhanced Li ion conductivity in Ge-doped Li 0.33 La 0.56 TiO 3 perovskite solid electrolytes for all-solid-state Li-ion batteries,' *New Journal of Chemistry* **42**, 9074 (2018).

17   L. Han, M.L. Lehmann, J. Zhu, T. Liu, Z. Zhou, X. Tang, C.-T. Heish, A.P. Sokolov, P. Cao, and X.C. Chen, 'Recent Developments and Challenges in Hybrid Solid Electrolytes for Lithium-Ion Batteries,' *Frontiers in Energy Research* **8**, 202 (2020).

18   X. Yu and A. Manthiram, 'A review of composite polymer-ceramic electrolytes for lithium batteries,' *Energy Storage Materials* (2021).

19   R. Wei, S. Chen, T. Gao, and W. Liu, 'Challenges, fabrications and horizons of oxide solid electrolytes for solid-state lithium batteries,' *Nano Select* (2021).

20   Y.C. Jung, S.M. Lee, J.H. Choi, and S.S. Jang, 'All solid-state lithium batteries assembled with hybrid solid electrolytes,' *Journal of The Electrochemical Society* (2015).

21   X. Wang, H. Zhai, B. Qie, Q. Cheng, A. Li, and J. Borovilas, 'Rechargeable solid-state lithium metal batteries with vertically aligned ceramic nanoparticle/polymer composite electrolyte,' *Nano Energy* (2019).

22   K. Nairn, M. Forsyth, H. Every, and M. Greville, 'Polymer-ceramic ion-conducting composites,' *Solid State Ionics* (1996).

23   H. Zhai, P. Xu, M. Ning, Q. Cheng, J. Mandal, and Y. Yang, 'A flexible solid composite electrolyte with vertically aligned and connected ion-conducting nanoparticles for lithium batteries,' *Nano Letters* (2017).

24   J. Zheng, P. Wang, H. Liu, and Y.Y. Hu, 'Interface-Enabled Ion Conduction in Li10GeP2S12–Poly(ethylene Oxide) Hybrid Electrolytes,' *ACS Applied Energy Materials* (2019).

25   Y. Zheng, M. Ouyang, X. Han, L. Lu, and J. Li, 'Investigating the error sources of the online state of charge estimation methods for lithium-ion batteries in electric vehicles,' *Journal of Power Sources* (2018).

26   J. Zhang, C. Zheng, J. Lou, Y. Xia, and C. Liang, 'Poly(ethylene oxide) reinforced Li6PS5Cl composite solid electrolyte for all-solid-state lithium battery: Enhanced electrochemical performance, mechanical property and interfacial stability,' *Journal of Power Sources* (2019).

27   C. Yan, M. Dirican, J. Zhu, J. Zang, and R.K. Selvan, 'Li0.33La0.557TiO3 ceramic nanofiber-enhanced

polyethylene oxide-based composite polymer

electrolytes for all-solid-state lithium batteries,' *Journal of*

Materials Chemistry A (2018).

28   X. Wang, Y. Zhang, X. Zhang, T. Liu, and Y.H. Lin, 'Lithium-Salt-Rich PEO/Li0.3La0.557TiO3 Interpenetrating Composite Electrolyte with Three-Dimensional Ceramic Nano-Backbone for All-Solid-State Lithium-Ion Batteries,' *ACS Applied Materials & Interfaces* (2018).

29   P. Song, H. Xu, J. Wang, Y. Shiraishi, and Y. Du, 'Construct 3D networked Au-Cu nanowires for enhanced plasmon-driven catalytic ethylene glycol oxidation through visible light irradiation,' *Journal of Power Sources* (2018).

30   D. Li, L. Chen, T. Wang, and L.Z. Fan, '3D fiber-network-reinforced bicontinuous composite solid electrolyte for dendrite-free lithium metal batteries,' *ACS applied materials & interfaces* (2018).

31   W. Liu, N. Liu, J. Sun, P.C. Hsu, Y. Li, H.W. Lee, and Y. Cui, 'Ionic conductivity enhancement of polymer electrolytes with ceramic nanowire fillers,' *Nano letters* (2015).

32   J. Ju, Y. Wang, B. Chen, J. Ma, and S. Dong, 'Integrated interface strategy toward room temperature solid-state lithium batteries,' *Applied materials & Interfaces* (2018).

33   D. Zhou, D. Shanmukaraj, A. Tkacheva, and M. Armand, 'Polymer electrolytes for lithium-based batteries: advances and prospects,' *Chem* (2019).

34   K. Sashmitha and M.U. Rani, 'A comprehensive review of polymer electrolyte for lithium-ion battery,' *Polymer Bulletin* (2022).

35   J. Castillo, A. Santiago, X. Judez, and I. Garbayo, 'Safe, flexible, and high-performing gel-polymer electrolyte for rechargeable lithium metal batteries,' *Chemistry of Materials* (2021).

36   T. Sudiarti, D. Wahyuningrum, and B. Bundjali, 'Mechanical strength and ionic conductivity of polymer electrolyte membranes prepared from cellulose acetate-lithium perchlorate,' *IOP Conference Series* (2017).

37   J.Y. Lee, P.H. Chung, S.C. Yeh, and T.Y. Yu, 'Tough Polymer Electrolyte with an Intrinsically Stabilized Interface with Li Metal for All-Solid-State Lithium-Ion Batteries,' *The Journal of Physical Chemistry C* (2021).

38   X. Zhang, S. Liu, Y. Zheng, X. Koh, Q.F. Lim, and M. Sharma, 'Elucidating the relationship between mechanical properties and ionic conductivity in a highly conductive gel polymer electrolyte,' *Materials Letters* (2021).

39   F. Mohammad, '*Specialty polymers: materials and applications*,' books.google.com 2007) https://books.google.com/books?hl=en&lr=&id=twTrmFOPqpkC&oi=fnd&pg=PR5&dq=specialty+materials+materials+and+applications&ots=c6iuaGoJOJ&sig=8FQMwLSOOF8w2vJ2lvtlbFaILKw.

40   S. Hull, 'Superionics: crystal structures and conduction processes,' *Reports on Progress in Physics* (2004).

41   H.H. Möbius, 'On the history of solid electrolyte fuel cells,' *Journal of solid state electrochemistry* (1997).

42   J. Kondoh, T. Kawashima, and S. Kikuchi, 'Effect of Aging on Yttria-Stabilized Zirconia: I. A Study of Its Electrochemical Properties,' *Journal of The Electrochemical Society* (1998).

43   H. Zhang and M. Armand, 'History of Solid Polymer Electrolyte-Based Solid-State Lithium Metal Batteries: A Personal Account,' *Israel Journal of Chemistry* **61**, 94 (2021).

44   A. Chandra, A. Chandra, and K. Thakur, 'Synthesis and characterization of hot pressed ion conducting solid polymer electrolytes:(1–x) PEO: x NaClO4,' *The European Physical Journal Applied Physics* **69**, 20901 (2015).

45   K. Bicy, A.B. Gueye, D. Rouxel, N. Kalarikkal, and S. Thomas, 'Lithium-ion battery separators based on electrospun PVDF: A review,' *Surfaces and Interfaces* 101977 (2022).

46   N.A.W. Holzwarth, 'First principles modeling of electrolyte materials in all-solid-state batteries,' *Physics Procedia* **57**, 29 (2014).

47   Y. Zheng, Y. Yao, J. Ou, M. Li, D. Luo, H. Dou, Z. Li, K. Amine, A. Yu, and Z. Chen, 'A review of composite solid-state electrolytes for lithium batteries: fundamentals, key materials and advanced structures,' *Chemical Society Reviews* **49**, 8790 (2020).

48   H. Mehrer, 'Diffusion mechanisms,' *Diffusion in Solids: Fundamentals* (2007).

49   M. Hakala, M.J. Puska, and R.M. Nieminen, 'First-principles calculations of interstitial boron in silicon,' *Physical Review B* (2000).

50   J. Lynch, C. Giannini, and J.K. Cooper, 'Substitutional or Interstitial Site-Selective Nitrogen Doping in TiO2 Nanostructures,' *The Journal of Physical Chemistry* (2015).

51   M. Yang, Y. Liu, A.M. Nolan, and Y. Mo, 'Interfacial Atomistic Mechanisms of Lithium Metal Stripping and Plating in Solid-State Batteries,' *Advanced Materials* **33**, 2008081 (2021).

52   W. Wang, R. Christensen, B. Curtis, S.W. Martin, and J. Kieffer, 'A new model linking elastic properties and ionic conductivity of mixed network former glasses,' *Physical Chemistry Chemical Physics* **20**, 1629 (2018).

53   D. Golodnitsky, E. Strauss, E. Peled, and S. Greenbaum, 'On order and disorder in polymer electrolytes,' *Journal of The Electrochemical Society* **162**, A2551 (2015).

54   X. Liu, T. Wang, L.C. Chow, and M. Yang, 'Effects of inorganic fillers on the thermal and mechanical properties of poly (lactic acid),' *International journal of Polymer Science* (2014).

55   M. Bustamante-Torres and D. Romero-Fierro, 'Interaction between filler and polymeric matrix in nanocomposites: Magnetic approach and applications,' *Polymers* (2021).

56   S.Y. Kim and C.F. Zukoski, 'Role of polymer segment–particle surface interactions in controlling nanoparticle dispersions in concentrated polymer solutions,' *Langmuir* (2011).

57   J. Zhu, C. Abeykoon, and N. Karim, 'Investigation into the effects of fillers in polymer processing,' *International Journal of Lightweight Materials and Manufacture* (2021).

58   S.K. Young, 'Overview of sol-gel science and technology,' *apps.dtic.mil* (2002).

59   T. Sugiyama, H. Shiba, and M. Yoshikawa, 'Synthesis of Polycyclic and Cage Siloxanes by Hydrolysis and Intramolecular Condensation of Alkoxysilylated Cyclosiloxanes,' *Chemistry A European Journal* (2019).

60   A.E. Danks, S.R. Hall, and Z.J.M.H. Schnepp, 'The evolution of 'sol–gel'chemistry as a technique for materials synthesis,' *Materials Horizons* **3**, 91 (2016).

61   G. Tesoro and Y. Wu, 'Silane coupling agents: the role of the organofunctional group,' *Journal of adhesion science and technology* (1991).

62   W. Li, M. Body, C. Legein, and D. Dambournet, 'Sol–Gel Chemistry of Titanium Alkoxide toward HF: Impacts of Reaction Parameters,' *Crystal Growth & Design* (2016).

63   S. Li, Q. Wan, Z. Qin, Y. Fu, and Y. Gu, 'Understanding Stöber silica's pore characteristics measured by gas adsorption,' *Langmuir* **31**, 824 (2015).

64   B. Brattekås and R. Seright, 'The mechanism for improved polymer gel blocking during low-salinity waterfloods, investigated using positron emission tomography imaging,' *Transport in Porous Media* **133**, 119 (2020).

65   K. Ishizaki, S. Komarneni, and M. Nanko, 'Sol-gel processing, designing porosity, pore size and polarity, and shaping processes,' in *Porous Materials*, (Springer, 1998), p. 67.

66   A.F.V. Matias, R.C.V. Coelho, J.S. Andrade Jr, and N.A.M. Araújo, 'Flow through time–evolving porous media: Swelling and erosion,' *Journal of Computational Science* **53**, 101360 (2021).

67   S. Sinha, A.T. Bender, M. Danczyk, K. Keepseagle, C.A. Prather, J.M. Bray, L.W. Thrane, J.D. Seymour, S.L. Codd, and A. Hansen, 'Effective rheology of two-phase flow in three-dimensional porous media: experiment and simulation,' *Transport in porous media* **119**, 77 (2017).

68   L.C. Klein, 'Sol-gel processing of silicates,' *Annual Review of Materials Science* (1985).

69   R. Ravikrishna, R. Green, and K.T. Valsaraj, 'Polyaphrons as Templates for the Sol–Gel Synthesis of Macroporous Silica,' *Journal of sol-gel science and ...* (2005).

70   E. Burkel, 'Introduction to x-ray scattering,' *Journal of Physics: Condensed Matter* **13**, 7477 (2001).

71   X. Jiang, X. Liu, Z. Zeng, L. Xiao, X. Ai, H. Yang, and Y. Cao, 'A bifunctional fluorophosphate electrolyte for safer sodium-ion batteries,' *IScience* **10**, 114 (2018).

72   S. Esposito, '"Traditional" sol-gel chemistry as a powerful tool for the preparation of supported metal and metal oxide catalysts,' *Materials* (2019).

73   W. Liu, N. Liu, J. Sun, P.-C. Hsu, Y. Li, H.-W. Lee, and Y. Cui, 'Ionic Conductivity Enhancement of Polymer Electrolytes with Ceramic Nanowire Fillers,' *Nano Letters* **15**, 2740 (2015).

74   M. Nookala, B. Kumar, and S. Rodrigues, 'Ionic conductivity and ambient temperature Li electrode reaction in composite polymer electrolytes containing nanosize alumina,' *Journal of Power Sources* **111**, 165 (2002).

75   W. Wang, E. Yi, A.J. Fici, R.M. Laine, and J. Kieffer, 'Lithium Ion Conducting Poly(ethylene oxide)-Based Solid Electrolytes Containing Active or Passive Ceramic Nanoparticles,' *Journal of Physical Chemistry C* **121**, 2563 (2017).

76   H.T. Ahmed and O.G. Abdullah, 'Structural and ionic conductivity characterization of PEO:MC-NH4I proton-conducting polymer blend electrolytes based films,' *Results in Physics* **16**, 102861 (2020).

77   C.J. Leo, G.V. Subba Rao, and B.V.R. Chowdari, 'Studies on plasticized PEO–lithium triflate–ceramic filler composite electrolyte system,' *Solid State Ionics* **148**, 159 (2002).

78   K.M. Diederichsen, H.G. Buss, and B.D. McCloskey, 'The Compensation Effect in the Vogel–Tammann–Fulcher (VTF) Equation for Polymer-Based Electrolytes,' *Macromolecules* **50**, 3831 (2017).

79   F.J. Richards, 'A flexible growth function for empirical use,' *Journal of experimental Botany* **10**, 290 (1959).

80   S. Mehrolia, S. Alagarsamy, and V.M. Solaikutty, 'Customers response to online food delivery services during COVID-19 outbreak using binary logistic regression,' *International Journal of Consumer Studies* **45**, 396 (2021).

81   D. Xiong, L. Zhang, G.L. Watson, P. Sundin, T. Bufford, J.A. Zoller, J. Shamshoian, M.A. Suchard, and C.M. Ramirez, 'Pseudo-likelihood based logistic regression for estimating COVID-19 infection and case fatality rates by gender, race, and age in California,' *Epidemics* **33**, 100418 (2020).

82   M. Amatria, D. Lapresa, J. Arana, M.T. Anguera, and B. Garzon, 'Optimization of Game Formats in U-10 Soccer Using Logistic Regression Analysis,' *Journal of Human Kinetics* **54**, 163 (2016).

83   J. Pearce and S. Ferrier, 'Evaluating the predictive performance of habitat models developed using logistic regression,' *Ecological Modelling* **133**, 225 (2000).

84   S. Ben Jabeur, 'Bankruptcy prediction using Partial Least Squares Logistic Regression,' *Journal of Retailing and Consumer Services* **36**, 197 (2017).

85   A.J. Dood, J.C. Dood, D.C.R. de Arellano, K.B. Fields, and J.R. Raker, 'Analyzing explanations of substitution reactions using lexical analysis and logistic regression techniques,' *Chemistry Education Research and Practice* **21**, 267 (2020).

86   J. Zhu, Z. Zhang, S. Zhao, A.S. Westover, I. Belharouak, and P. Cao, 'Single-ion conducting polymer electrolytes for solid-state lithium–metal batteries: design, performance, and challenges,' *Advanced Energy Materials* **11**, 2003836 (2021).

87   L. Porcarelli, P. Sutton, V. Bocharova, R.H. Aguirresarobe, H. Zhu, N. Goujon, J.R. Leiza, A. Sokolov, M. Forsyth, and D. Mecerreyes, 'Single-Ion Conducting Polymer Nanoparticles as Functional Fillers for Solid Electrolytes in Lithium Metal Batteries,' *ACS applied materials & interfaces* **13**, 54354 (2021).

88   H. Zhang, Z. Song, W. Yuan, W. Feng, J. Nie, M. Armand, X. Huang, and Z. Zhou, 'Impact of negative charge delocalization on the properties of solid polymer electrolytes,' *ChemElectroChem* **8**, 1322 (2021).

89   H. Yuan, J. Luan, Z. Yang, J. Zhang, Y. Wu, Z. Lu, and H. Liu, 'Single lithium-ion conducting solid polymer electrolyte with superior electrochemical stability and interfacial compatibility for solid-state lithium metal batteries,' *ACS applied materials & interfaces* **12**, 7249 (2020).

90   C.D. Rodríguez-Fernández, L.M. Varela, C. Schröder, and E.L. Lago, 'Charge delocalization and hyperpolarizability in ionic liquids,' *Journal of Molecular Liquids* **349**, 118153 (2022).

91   V. St-Onge, M. Cui, S. Rochon, J.-C. Daigle, and J.P. Claverie, 'Reducing crystallinity in solid polymer electrolytes for lithium-metal batteries via statistical copolymerization,' *Communications Materials* **2**, 1 (2021).

92   S. Wang, W. Zhang, X. Chen, D. Das, R. Ruess, A. Gautam, F. Walther, S. Ohno, R. Koerver, and Q. Zhang, 'Influence of crystallinity of lithium thiophosphate solid electrolytes on the performance of solid-state batteries,' *Advanced Energy Materials* **11**, 2100654 (2021).

93   T. Itoh, Y. Mitsuda, T. Ebina, T. Uno, and M. Kubo, 'Solid polymer electrolytes composed of polyanionic lithium salts and polyethers,' *Journal of Power Sources* **189**, 531 (2009).

94   W. Wang, W. Liu, G.J. Tudryn, R.H. Colby, and K.I. Winey, 'Multi-length scale morphology of poly (ethylene oxide)-based sulfonate ionomers with alkali cations at room temperature,' *Macromolecules* **43**, 4223 (2010).

95   G. Guzmán-González and S. Vauthier…, 'Single-Ion Lithium Conducting Polymers with High Ionic Conductivity Based on Borate Pendant Groups,' *Angewandte* (2022).

96   W. Cai, Y. Zhang, J. Li, Y. Sun, and H. Cheng, 'Single-Ion Polymer Electrolyte Membranes Enable Lithium-Ion Batteries with a Broad Operating Temperature Range,' *Chemistry-Sustainability-Energy-Materials* **7**, 1063 (2014).

97   M. Piszcz, O. Garcia-Calvo, U. Oteo, J.M.L. del Amo, C. Li, L.M. Rodriguez-Martinez, H.B. Youcef, N. Lago, J. Thielen, and M. Armand, 'New single ion conducting blend based on PEO and PA-LiTFSI,' *Electrochimica Acta* **255**, 48 (2017).

98   L. Meabe, N. Goujon, C. Li, M. Armand, M. Forsyth, and D. Mecerreyes, 'Single-Ion Conducting Poly (Ethylene Oxide Carbonate) as Solid Polymer Electrolyte for Lithium Batteries,' *Batteries & Supercaps* **3**, 68 (2020).

99   A. Bergfelt, L. Rubatat, D. Brandell, and T. Bowden, 'Poly (benzyl methacrylate)-poly [(oligo ethylene glycol) methyl ether methacrylate] triblock-copolymers as solid electrolyte for lithium batteries,' *Solid State Ionics* **321**, 55 (2018).

100   Z. Shao and P. Jannasch, 'Single lithium-ion conducting poly (tetrafluorostyrene sulfonate)–polyether block copolymer electrolytes,' *Polymer Chemistry* **8**, 785 (2017).

101   X.-G. Sun, J. Hou, and J.B. Kerr, 'Comb-shaped single ion conductors based on polyacrylate ethers and lithium alkyl sulfonate,' *Electrochimica acta* **50**, 1139 (2005).

102   L. Porcarelli, M.A. Aboudzadeh, L. Rubatat, J.R. Nair, A.S. Shaplov, C. Gerbaldi, and D. Mecerreyes, 'Single-ion triblock copolymer electrolytes based on poly (ethylene oxide) and methacrylic sulfonamide blocks for lithium metal batteries,' *Journal of Power Sources* **364**, 191 (2017).

103 C.T. Elmore, M.E. Seidler, H.O. Ford, L.C. Merrill, S.P. Upadhyay, W.F. Schneider, and J.L. Schaefer, 'Ion transport in solvent-free, crosslinked, single-ion conducting polymer electrolytes for post-lithium ion batteries,' *Batteries* **4**, 28 (2018).

104 U. Subramanyam and J.P. Kennedy, 'PVA networks grafted with PDMS branches,' *Journal of Polymer Science Part A: Polymer Chemistry* **47**, 5272 (2009).

105 S. Feng, D. Shi, F. Liu, L. Zheng, J. Nie, W. Feng, X. Huang, M. Armand, and Z. Zhou, 'Single lithium-ion conducting polymer electrolytes based on poly [(4-styrenesulfonyl)(trifluoromethanesulfonyl) imide] anions,' *Electrochimica Acta* **93**, 254 (2013).

106 D. Devaux, L. Liénafa, E. Beaudoin, S. Maria, T.N.T. Phan, D. Gigmes, E. Giroud, P. Davidson, and R. Bouchet, 'Comparison of single-ion-conductor block-copolymer electrolytes with Polystyrene-TFSI and Polymethacrylate-TFSI structural blocks,' *Electrochimica Acta* **269**, 250 (2018).

107 Y. Lu, M. Tikekar, R. Mohanty, K. Hendrickson, L. Ma, and L.A. Archer, 'Stable cycling of lithium metal batteries using high transference number electrolytes,' *Advanced Energy Materials* **5**, 1402073 (2015).

108 F. Ahmed, I. Choi, M.M. Rahman, H. Jang, T. Ryu, S. Yoon, L. Jin, Y. Jin, and W. Kim, 'Remarkable conductivity of a self-healing single-ion conducting polymer electrolyte, poly (ethylene-Co-acrylic lithium (fluoro sulfonyl) imide), for all-solid-state Li-ion batteries,' *ACS applied materials & interfaces* **11**, 34930 (2019).

109   D.H.C. Wong, J.L. Thelen, Y. Fu, D. Devaux, A.A. Pandya, V.S. Battaglia, N.P. Balsara, and J.M. DeSimone, 'Nonflammable perfluoropolyether-based electrolytes for lithium batteries,' *Proceedings of the National Academy of Sciences* **111**, 3327 (2014).

110   K. Sinha and J.K. Maranas, 'Segmental dynamics and ion association in PEO-based single ion conductors,' *Macromolecules* **44**, 5381 (2011).

111   S. Li, A.I. Mohamed, V. Pande, H. Wang, J. Cuthbert, X. Pan, H. He, Z. Wang, V. Viswanathan, and J.F. Whitacre, 'Single-ion homopolymer electrolytes with high transference number prepared by click chemistry and photoinduced metal-free atom-transfer radical polymerization,' *ACS Energy Letters* **3**, 20 (2017).

112   L. Ye and Z. Feng, 'Polymer electrolytes as solid solvents and their applications,' in *Polymer Electrolytes*, (Elsevier, 2010), p. 550.

113   S. Zugmann, M. Fleischmann, M. Amereller, R.M. Gschwind, H.D. Wiemhöfer, and H.J. Gores, 'Measurement of transference numbers for lithium ion electrolytes via four different methods, a comparative study,' *Electrochimica Acta* **56**, 3926 (2011).

114   M. Rosso, J.-N. Chazalviel, and E. Chassaing, 'Calculation of the space charge in electrodeposition from a binary electrolyte,' *Journal of Electroanalytical Chemistry* **587**, 323 (2006).

115   Y. Yan, C. Shu, R. Zheng, M. Li, Z. Ran, M. He, A. Hu, T. Zeng, H. Xu, and Y. Zeng, 'Modulating Sand's time by ion-transport-enhancement toward dendrite-free lithium metal anode,' *Nano Research* 1 (2021).

116 H. Mohd Yusop, A.I.H. Mohd Ismail, and W.N. Wan Ismail, 'Preparation and characterization of new sol–gel hybrid inulin–TEOS adsorbent,' *Polymers* **13**, 1295 (2021).

117 M. Siekierski, M. Bukat, M. Ciosek, M. Piszcz, and M. Mroczkowska-Szerszeń, 'Transference Number Determination in Poor-Dissociated Low Dielectric Constant Lithium and Protonic Electrolytes,' *Polymers* **13**, 895 (2021).

118 Y. Shao, H. Gudla, D. Brandell, and C. Zhang, 'Transference number in polymer electrolytes: mind the reference-frame gap,' *Journal of the American Chemical Society* **144**, 7583 (2022).